CONTROLS AND RATES OF ACID PRODUCTION IN COMMERCIAL-SCALE SULPHUR BLOCKS

A Thesis submitted to the College of
Graduate Studies and Research
in partial fulfillment of the requirements
for the degree of Doctor of Philosophy
in the Department of Geological Sciences
University of Saskatchewan
Saskatoon, SK, Canada

By
TYLER K. BIRKHAM

PERMISSION TO USE

In presenting this thesis in partial fulfillment of the requirements for a Postgraduate degree from the University of Saskatchewan, I agree that the Libraries of this University may make it freely available for inspection. I further agree that permission for copying of this thesis in any manner, in whole or in part, for scholarly purposes may be granted by the professor or professors who supervised my thesis work or, in their absence, by the Head of the Department or the Dean of the College in which my thesis work was done. It is understood that any copying or publication or use of this thesis or parts thereof for financial gain shall not be allowed without my written permission. It is also understood that due recognition shall be given to me and to the University of Saskatchewan in any scholarly use which may be made of any material in my thesis.

Requests for permission to copy or to make other use of material in this thesis in whole or part should be addressed to:

Head of the Department of Geological Sciences
University of Saskatchewan
114 Science Place
Saskatoon, Saskatchewan, Canada
S7N 5E2

ABSTRACT

The controls of water and O_2 availability, microbial activity and temperature on acid (H_2SO_4) production rates in commercial-scale sulphur (S^0) blocks were quantified and recommendations were made for minimizing H_2SO_4 production in S^0 blocks. Acidic drainage from the S^0 blocks (pH 0.4-1.0) was attributed to mixing of fresh infiltrating water and low-pH resident water (mean pH=-2.1) with resident water comprising ~4-8% of the drainage. Although clean S^0 is strongly hydrophobic, preferential water infiltration occurred rapidly through fractured S^0 blocks in which the bulk hydraulic conductivity was estimated to be similar to gravel or clean sand (K_s=1×10^{-1} to 1×10^{-3} m/s). Microbial colonization of fracture faces generated localized hydrophilic conditions that helped create preferential pathways for water infiltration. Liquid water contact (compared to water vapour) was essential for S^0 oxidation (i.e., H_2SO_4 production), therefore H_2SO_4 production in the S^0 blocks was limited to fractures and friable S^0 through which water flowed. H_2SO_4 production was greatest in the upper 1 m of the S^0 block (70 to >97% of annual H_2SO_4 production) and the result of autotrophic microbial S^0 oxidation.

S^0 oxidation rates were very sensitive to temperature and increased by a factor of 4.3 for a temperature increase of 10°C (Q_{10}). Therefore minimizing temperature (<5°C) in S^0 blocks would be an effective strategy for controlling H_2SO_4 production. Heat released during S^0 oxidation did have a measurable effect on *in situ* temperatures and should be considered in the design of insulated cover systems. Although autotrophic microbial activity was insensitive to O_2 concentrations when they were >1 vol.%, the total mass production rate of H_2SO_4 is approximately proportional to the O_2 concentration at the surface of the S^0 block (assuming *in situ* O_2 concentrations decrease to <1 vol. %). Therefore, cover systems that minimize the surficial O_2 concentration are recommended.

Cover systems limiting H_2O infiltration would be effective for minimizing the volume of acidic drainage, but may have no impact on H_2SO_4 production rates within the block. In this study, H_2O infiltration through a typical soil cover (~95% efficiency) would easily satisfy the annual H_2O demand for H_2SO_4 production (2.6 mm/m^2 in the upper 1 m). Greater near-surface H_2SO_4 production rates may appear to make surficial biocide application an attractive option for minimizing S^0-oxidizing microbial activity,

however, this approach might simply drive the zone of H_2SO_4 production to greater depths and have no affect on the total mass production of H_2SO_4.

ACKNOWLEDGEMENTS

I would not have had the ability or desire to finish this degree without the help of many people.

Dr. M. Jim Hendry has been a wise mentor and great source of encouragement since our first meeting in 1997. I would have ventured elsewhere to study and conduct research long ago if I did not think I was learning from one of the best. His energy, enthusiasm, integrity, persistence, and loyalty are contagious and inspirational.

Dr. S. Lee Barbour is a tireless guide whose voice of insight and reason has helped me navigate numerous technical conundrums. Thankfully there are teachers like Lee who combine profound understanding with passion and ability for helping others see the pattern that does exist.

I thank Robert Mahood, Ron Lewko, and Gord McKenna who were the main industry contacts with Syncrude Canada Ltd. at various times during the project. They each provided meaningful and generous support for the project, and me, in a variety of ways.

I thank my committee members (Drs. Ansdell, Wassenaar, Eglington, and Renaut) for their contributions.

I thank the University of Saskatchewan, NSERC, and Syncrude Canada Ltd. for generous financial support.

I thank the host of summer students, fellow graduate students, and technical support who helped me along the way. In particular, Julie Robertson, Rob Holben, Ray Kirkland, Matt Harker, Sean Shaw, Jeremy Ledding, Brigitte Boldt-Leppin and Kristie Bonstrom.

Chris and Susan Wall provided me a ‘home-away-from-home’ in Saskatoon for many months as I pursued my degree from afar; their friendship is cherished.

I am so thankful for my great wife, Joanna. I could not have asked for a better partner for life.

Any redeeming qualities I might possess that helped me persevere and complete this degree can be traced to my mom, dad, and brother. My extended family has also been wonderfully supportive.

Despite the risk of sounding trite, I am humbled and grateful for the subtle, yet powerful, work of God in my life. The yoke has been easy and the burden light since following and learning from Jesus.

TABLE OF CONTENTS

LIST OF FIGURES

LIST OF TABLES

1.0 INTRODUCTION

1.1 Study Motivation

Global production of elemental sulphur (S^0) has exceeded market demand by as much as 1-3 Mt per year (Kitto, 2005) during the last 20 years resulting in stockpiling of 21 Mt of S^0 (Broere, 2008). These S^0 stockpiles are typically surface deposits and are exposed to atmospheric oxygen and precipitation which results in S^0 oxidation and associated sulphuric acid (H_2SO_4) production. The production and drainage of H_2SO_4 from the S^0 blocks is an environmental concern as surrounding surface water, groundwater, and soils are at risk of acidification and salinization. To our knowledge, no studies in the published literature have focused on this problem, therefore the purpose of this study was to define the controls on H_2SO_4 production and transport from S^0 blocks and relate these findings to the design of S^0 storage strategies that limit the environmental impact of S^0 stockpiles.

1.2 Overview

Greater than 90% of global S^0 production is a byproduct of bitumen upgrading, natural gas plants, coking plants, and non-ferrous metal smelters (Kitto, 2005). Increased S^0 production from these sources created a global S^0 surplus in the 1990's and 2000's and S^0 prices decreased from $140 USD (current $) per t in 1985 to $20-$60US per t from 2001 to 2005 (Kitto, 2005). Producers of S^0 in landlocked locations or with inadequate infrastructure have been at the greatest economic disadvantage and have stored large quantities of S^0 (i.e. northern Canada, Middle East, Caspian Sea regions). Although the price of S^0 rebounded to as much as $700 US per t from 2005-2008 (Kosich, 2008), forecasts predict widespread stockpiling of S^0 from 2011-2017 (ERCB, 2008). Canada, the world's largest S^0-producer, stockpiled 11.6 Mt of S^0 as of April 2008 (ERCB, 2008). Alberta is the leading S^0-producing province in Canada with 4.8 Mt and 1.5 Mt of S^0 produced from sour gas plants and bitumen upgrading in 2007,

respectively (ERCB, 2008). Annual S^0 production from bitumen upgrading at oilsand mines in northern Alberta is expected to increase to 5.7 Mt by 2017 (ERCB, 2008).

S^0 is typically stored above ground in large blocks containing hundreds of thousands of cubic meters of S^0, and with width/length dimensions of 100-200 m and depths of 10-25 m (P. Davis, personal communications). The blocks are gradually built up by pouring thin sequential lifts (<0.1 m) of molten S^0 (>115°C) into areas confined by metal forms. The molten S^0 solidifies within 1 d and shrinks by 7 % during this phase change. The solid S^0 shrinks an additional 5.5 % over several days when the temperature decreases to <95°C and the mineral structure changes from a monoclinic to rhombic crystal (Meyer, 1977). These volume changes result in extensive vertical and horizontal fracturing of S^0 blocks (Syncrude, 2004a; Bonstrom et al., 2009). Considering S^0 is extremely hydrophobic (Lyklema, 1995) and are typically well drained (Syncrude, 2004b), S^0 blocks can be generally be described as fractured, unsaturated, and hydrophobic.

Drainage water from S^0 blocks that are >20 yrs old is usually, if not always, acidic (pH <1.5; D. Wainwright, B. Goliss personal communications) as a result of S^0 oxidation (H_2SO_4 production). This reaction is described as follows:

$$2S^0 + 3O_2 + 2H_2O \rightarrow 2H_2SO_4 \qquad [1.1]$$

The acidic drainage at most S^0 blocks is collected in storage ponds and neutralized with lime or caustic (D. Wainwright, personal communications) or combined and neutralized with basic mine process waters (R. Carter, personal communications). This approach to managing the environmental impact of S^0 blocks requires continual monitoring and maintenance and is not a practical long-term management strategy as S^0 blocks may be in existence for several decades to hundreds of years. Alberta Sulphur Research Ltd., an organization representing the research interests of 63 S^0-related companies internationally, has identified long-term S^0 storage that minimizes H_2SO_4 production as an important challenge that requires further study.

1.3 Research Objectives

Fundamental to the development of long-term S^0 storage practices that limit H_2SO_4 production is an understanding of the controls on H_2SO_4 production in S^0

blocks. The goal of this study was to quantify the controls on H_2SO_4 production in commercial-scale S^0 blocks due to rate-determining factors such as oxygen and water availability, and temperature. The objectives were to:

1) quantify the distribution and controls on moisture water availability in S^0 blocks;
2) quantify the relative importance of diffusive and advective gas (i.e. O_2) transport in S^0 blocks;
3) quantify the present-day rates and controls on S^0 block oxidation;
4) define the distribution of H_2SO_4 production in S^0 blocks; and
5) identify mechanisms to control or reduce rates of S^0 block oxidation.

This dissertation is a compilation of three research papers which are presented in Chapters 2, 3, and 4 and address objectives 1, 2, and 3-5, respectively. All field data were collected at two commercial-scale above-ground S^0 blocks (referred to as Phase 1 and Phase 2 blocks) located at the Syncrude Canada Ltd. oilsands mine in northern Alberta, Canada (57°02'34.89"N, 111°38'36.14"W). The current study was part of a larger, cooperative research program involving 5 other graduate students focusing on various aspects of S^0 block oxidation and acidic drainage. The actual evaporation rates in Chapter 2, contact angles and surface conditioning films in Chapter 2, and *in situ* temperature profiles in Chapter 4 were measured by Dr. Sean K. Carey (Carleton University), Dr. John Lawrence (National Hydrology Research Centre) and Syncrude Canada Ltd., respectively. All other data presented were measured by the author of the current study. Manuscripts were edited by Dr. M. Jim Hendry, Dr. S. Lee Barbour, Dr. John Lawrence, and Dr. Sean Carey. As of June 2009, each manuscript had been submitted to scholarly journals for publication review. While the contents and conclusions of each manuscript in this thesis dissertation and as submitted for journal review are the same, the manuscripts have been edited and formatted to maintain consistency within this document.

In Manuscript 1 (Chapter 2), a water balance for the S^0 blocks was quantified by measuring precipitation and actual evaporation at the surface of the Phase 1 block and outflow rates from the Phase 2 block. The volume of water stored in the Phase 1 block was quantified by measuring depth profiles of moisture content, and the storage and release of water along the base of the block in response to rainfall events. A 1-D

analytical solution was used to quantify vertical water infiltration through the blocks, and a 2-D numerical model was used to simulate the unconfined flow system that develops at the base of the blocks in response to rainfall events. The analytical solution and numerical model were used in tandem to simulate hydraulic head and outflow responses to rainfall events and to estimate specific yield (S_y) and saturated hydraulic conductivity (K_s) values. Water repellency measurements of matrix and fractured S^0, dye tracer testing, and microbial analyses of matrix and fractured S^0 were used to confirm and interpret the modelling results.

In Manuscript 2 (Chapter 3), advective gas fluxes were quantified by measuring and modelling *in situ* N_2 concentrations along a cross-section through the Phase 1 block. *In situ* diffusion coefficients were estimated by modelling an *in situ* gas tracer experiment. Diffusion coefficients for unfractured S^0 were quantified by laboratory diffusion experiments on core samples collected from the Phase 1 block. The estimates of the advective gas flux and diffusion coefficients were then used to model *in situ* O_2 concentration distributions and to estimate total influx rates of O_2.

Manuscript 3 (Chapter 4) builds on the results of Manuscripts 1 and 2 and provides a more comprehensive analysis of the production and environmental loadings of H_2SO_4 from S^0 blocks. In addition, the control of temperature on S^0 oxidation rates in laboratory experiments, modelling of *in situ* temperature distributions in the Phase 1 block, and measured pH and SO_4 concentration in drainage waters from the Phase 2 block over one field season are presented. Comparisons are made between estimated H_2SO_4 production rates from O_2 modelling and measured H_2SO_4 loadings in drainage waters, and the mixing ratio of fresh infiltrating water and acidic resident water is estimated.

The findings from this study are widely applicable to other S^0 blocks because the construction of S^0 blocks is similar regardless of location (Syncrude, 2004a; personal comm. Paul Davis, Alberta Sulphur Research Ltd. general manager).

1.4 Literature Review

1.4.1 S^0 oxidation

S^0 oxidation (Eq.[1.1]) is the result of heterotrophic or autotrophic microbial activity. Autotrophic S^0-oxidizers (eg. *Acidithiobacilli*) utilize the electron transfer during S^0 oxidation as their main energy source, and fixate C-1 compounds (eg. CO_2) to generate biomass (Lizama et al., 2002). Heterotrophic S^0 oxidation produces CO_2 and is mostly incidental during oxidation of organic material for energy and growth. The activity of S^0-oxidizing microorganisms is strongly controlled by temperature (Wen et al., 2001) and the availability of oxygen, water, and substrates (Janzen and Bettany, 1987a, b). Most S^0 blocks are uncovered thereby exposing the S^0 to atmospheric oxygen, precipitation, and wind-blown sediments which contain S^0-oxidizing microorganisms (Lawrence and Germida, 1988) and substrates.

Because S^0 stockpiling is relatively recent, there are no published studies of S^0 block oxidation in the literature. However, S^0 oxidation has been widely studied as it relates to soil fertility and acidification. Results from these studies may not apply directly to S^0 blocks as S^0 particle size in these studies was generally <1 mm and S^0 was combined with soil (c.f., Chapman, 1989; Jaggi et al., 1999) or synthetic salts (Laishley et al., 1986). S^0 oxidation rates were quantified by measuring the increase in SO_4 concentrations (c.f., Janzen and Bettany, 1989a) and were found to be more sensitive to temperature than soil respiration processes (Li and Caldwell, 1966; Nor and Tabatabai, 1977; Jaggi et al., 1999), with very low or negligible oxidation rates at temperatures <5°C (Li and Caldwell, 1966; Nor and Tabatabai, 1977; Skiba and Wainwright, 1984; Janzen and Bettany, 1987b). Oxidation rates were limited at high and low moisture contents due to limited O_2 availability and water availability, respectively (Janzen and Bettany, 1989b). The control of O_2 concentrations on S^0 oxidation rates was not quantified in the literature, however O_2 availability was generally considered to be a primary control on S^0 oxidation. The effect of low pH on S^0 oxidation rates has not been studied in detail, however Baker et al. (2004) measured viable microbial communities in acidic mine drainage (from sulphide mineral oxidation) with pH 0.5-0.9.

1.4.2 Subsurface temperatures

Subsurface temperatures are controlled by the thermal properties of the geologic media and by heat sources or sinks. Important thermal properties include thermal conductivity and specific heat capacity, where thermal conductivity is the ability of a material to transmit heat and volumetric heat capacity is the heat required to increase the temperature of a unit volume of material by 1°C (Hillel, 1998). Heat sources or sinks may be anthropogenic (eg., pipelines, subsurface injection fluids) or naturally occurring (eg. geochemical reactions, seasonal temperature variation). Temperature variations from seasonal fluctuations in air temperature are usually limited to depths <5 m, with the magnitude of variation decreasing with increasing depth (Hillel, 1998). Exothermic or endothermic geochemical reactions produce or absorb heat at a rate proportional to the rate of reaction (Harries and Ritchie, 1985). S^0 oxidation is an exothermic reaction with a free energy of -415 $kJ \cdot mol^{-1}$ (Lizama et al., 2002). S^0 has a thermal conductivity and volumetric heat capacity of 0.269 $J \cdot s^{-1} \cdot m^{-1} \cdot °C^{-1}$ and 1420 $kJ \cdot m^{-3} \cdot °C^{-1}$, respectively (Lide, 2003) compared to 1.17 $J \cdot s^{-1} \cdot m^{-1} \cdot °C^{-1}$ and 2094 $kJ \cdot m^{-3} \cdot °C^{-1}$, respectively, for moist, compacted clay (porosity=40%, volumetric moisture content=20%; Hillel, 1998).

1.4.3 Subsurface gas transport and composition

Oxidation rates in the subsurface (Eq.[1.1]) are dependent on O_2 supply from the atmosphere (Binning et al., 2007). The consumption of O_2 during oxidation decreases subsurface O_2 concentrations resulting in diffusive O_2 influx across the ground/atmosphere interface. Steady-state diffusive flux in porous media is most simply and commonly quantified by Fick's first law:

$$J_i = -\theta_a \omega D_{air} \frac{dC_i}{dz} \qquad [1.2]$$

where J_i is the mass flux of species i (MT^{-1}), θ_a is the air-filled porosity, ω is the relative gas diffusivity (dimensionless; Moldrup et al., 2004) which is <1 and related to the inverse of the tortuosity (τ) of the porous medium (ratio of gas particle path length to straight-line travel distance), C_i is the concentration of species i (ML^{-3}), z is the distance in the direction of the mass flux (L), and D_{air} is the diffusion coefficient of the species in free air (L^2T^{-1}).

Transient diffusion of gases in porous media can be described by Fick's second law:

$$\theta_a \frac{\partial C_i}{\partial t} = \theta_a \omega D_{air} \frac{\partial^2 C_i}{\partial z^2} + \beta \qquad [1.3]$$

where β ($ML^{-3}T^{-1}$) is the rate of gas production or removal.

The effective coefficient of diffusion within the porous medium, D_e (L^2T^{-1}), can be defined by:

$$D_e = \omega D_{air} \qquad [1.4]$$

D_e values are a function of temperature (T) and can be scaled by (Fuller et al., 1966):

$$\left(\frac{T}{T_o}\right)^{1.75} \qquad [1.5]$$

where T_o is the temperature (K) at which D is known.

Diffusive fluxes of O_2, or any gas species, in the subsurface can be estimated relatively easily if the concentration gradients, θ_a and D_e are known (Eq.[1.2] and [1.3]). Although diffusion is typically considered the dominant mechanism of gas transport through a porous medium (Mendoza and Frind, 1990), advective gas transport can also be an important consideration when total pressure or density gradients exist (Thorstenson and Pollock, 1989). Advection is defined as the bulk movement of gas from areas of high pressure to areas of low pressure, with the advective flux of a gas species equal to its partial pressure multiplied by the bulk volumetric advective gas flux. Total pressure gradients can be caused by spatial variations in temperature (Harries and Ritchie, 1985), gas consumption or production rates (Amos et al., 2005), or changes in atmospheric and wind pressures (Massmann and Farrier, 1992).

Subsurface pore gas composition is typically a mixture of at least three gas species (O_2, N_2, and CO_2) with the magnitude and direction of the total flux of each gas species (combined effects of diffusion and advection) dependent on the fluxes of other gas species. For example, N_2 is typically non-reactive in the subsurface therefore there is no total net flux of N_2 at ground surface. However, N_2 concentration gradients can develop if O_2 is consumed in the subsurface without an equimolar production of a replacement gas. In this case, the total pressure will decrease in the subsurface and an

advective influx of atmospheric air will develop. To balance the advective influx of N_2, N_2 concentrations in the subsurface will increase and a diffusive efflux of N_2 will develop. Total O_2 influx is the sum of the diffusive and advective components, and may be significantly underestimated if only the diffusive flux is considered.

1.4.4 Water availability for S^0 oxidation

Water is a primary control on microbial oxidation rates of S^0 (Eq.[1.1]). The water balance equation for a S^0 block can be described by:

$$\Delta V_w = P - R + D - E \qquad [1.6]$$

where V_w is the volume of water stored (L^3), P is precipitation, R is the sum of runon-runoff, D is drainage from the porous medium, and E is water removed from the porous medium through evaporation (Warrick, 2002). Water runoff and runon can be ignored in the case of S^0 blocks, therefore changes in water storage are a function of precipitation, drainage, and evaporation.

1.4.4.1 Water storage

Water retention in a porous medium is similar to that of a capillary tube where:

$$H_C = \frac{2\gamma \cos\alpha}{r\rho g} \qquad [1.7]$$

where H_C is the height of capillary rise (L), γ is the water-air surface tension (MT^{-2}), α is the water-solid contact angle (defined as the angle between the solid surface and the outside face of the drop measured through the liquid), r is the capillary radius (L), ρ is the water density (ML^{-3}), and g is the gravitational constant (LT^{-2}).

Pore spaces and fractures are analogous to a capillary tube into which water spontaneously enters for hydrophilic conditions ($\alpha<90°$) but must be forced in for hydrophobic conditions ($\alpha>90°$, negative H_C). Negative matric potential (i.e. matric suction; the difference between pore air (u_a) and pore water pressure(u_w)) is required to remove water from pores of a hydrophilic porous medium while positive matric potential (positive pore water pressure) is required to force water into the pores of a hydrophobic medium. The suction required to desaturate (hydrophilic conditions), or

pressure required to saturate (hydrophobic conditions), pores or fractures increases with decreasing pore diameter or fracture aperture (equivalent to r in Eq.[1.7]).

The relationship between moisture content and matric potential is commonly referred to as the soil water characteristic curve (Figure 1.1). The residual moisture content is defined as the moisture content at which a decrease in matric potential does not significantly change the moisture content. The specific yield is defined as the volumetric fraction of a porous medium that will drain under gravity forces. For hydrophilic coarse-grained media (low air entry suctions) specific yield can be as great as the difference between the saturated and residual volumetric water contents. For hydrophobic media, the specific yield will theoretically be equal to the saturated volumetric water content as there will be no water retention in the absence of positive pore water pressures during drainage conditions (Figure 1.1). The persistence of hydrophobic conditions may vary depending on microbial colonization of the hydrophobic surface (Knickerbocker et al., 2000) and the phenomena causing the hydrophobic behaviour (Dekker and Ritsema, 2000).

The water storage capacity of a porous medium is equal to its interconnected (effective) porosity. Although the effective porosity of the matrix S^0 block component (5.5 %; Bonstrom et al., 2009) was 3.9 times greater than the fracture porosity (1.4%, Bonstrom, 2007; discussed below in section 1.4.5), most of the matrix porosity was likely inaccessible to water flow (storage) for typical above-ground S^0 block storage. The mean pore diameter (0.2 μm; K. Bonstrom, personal communication) was more than three orders of magnitude less than the mean fracture aperture (1.0 and 1.2 mm for horizontal and vertical fractures, respectively), resulting in a water entry pressure head of matrix S^0 (>1m; Figure 1.1) more than three orders of magnitude greater than the water entry pressure head for the average fracture. Therefore, infiltrating water would preferentially enter the fractures of S^0 blocks and occupy the matrix porosity only when pore water pressures exceeded 1-2 m (Bonstrom et al., 2009).

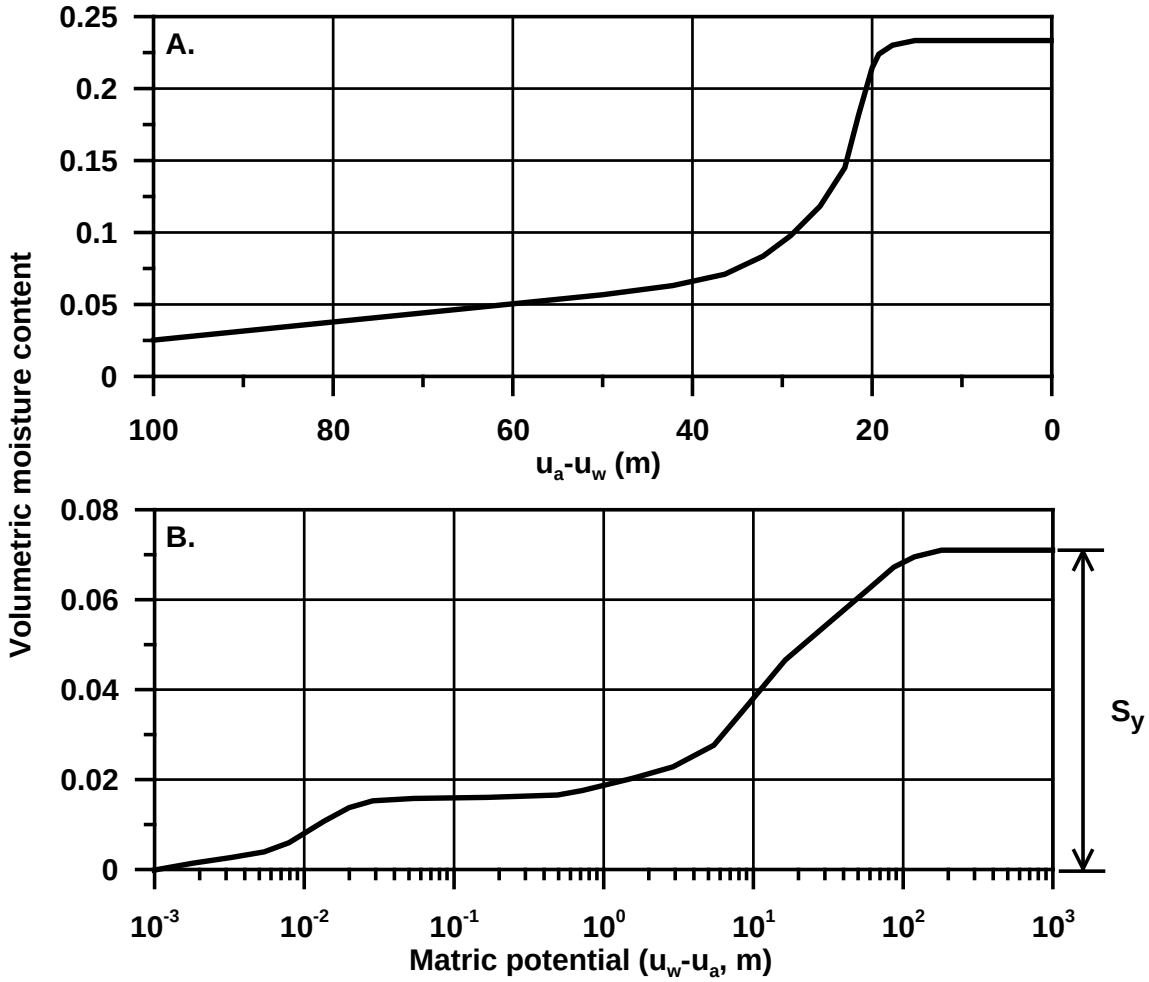

Figure 1.1. Conceptual soil water characteristic curve for an A.) hydrophilic silt (90%)-sand (10%) mixture (after Fredlund and Rahardjo, 1993), and B.) hydrophobic fractured S^0 block (after Bonstrom, 2007).

1.4.4.2 Water flow

Water flow or drainage through a porous medium can be described at steady state by Darcy's Law:

$$q = -Ki \qquad [1.8]$$

where K is the hydraulic conductivity ($L \cdot T^{-1}$), q is the unit flux of water ($L^3 \cdot T^{-1} \cdot L^{-2}$), and i is the hydraulic head gradient (dimensionless) equal to the change in total head (L) over a distance z (L).

Hydraulic conductivity is greatest for saturated conditions (K_s) and decreases with decreasing saturation as pore water and flow pathways become less interconnected

(Fredlund and Rahardjo, 1993). Unsaturated hydraulic conductivity of hydrophilic soils has been related to saturation by the Brooks and Corey (1964) relation:

$$K(S) = K_s S^{\frac{1}{\beta}} \qquad [1.9]$$

where $S = (\theta_w - \theta_r) / (n - \theta_r)$ with θ_r = residual moisture content, n = total porosity, and β is an empirical parameter.

Although Eq.[1.9] is usually applied to soils, the Brooks-Corey relationship can also be used for fractured networks with rough walls (Cey et al. 2006) and with a large range of fracture apertures at low pressure heads (Guarracino 2006).

Water flow through unsaturated fractured media is complex and dependent on the hydraulic properties (eg. storage capacity, water retention properties, hydraulic conductivity) of the matrix and fracture network, as well as antecedent moisture conditions, depth of the unsaturated zone, and precipitation intensity and duration. Fractures act as preferential flow pathways in saturated conditions with the saturated hydraulic conductivity of fractures (K_f) increasing with increasing fracture aperture according to (Cey et al., 2006):

$$K_f = \frac{\rho g b^2}{12\mu} \qquad [1.10]$$

where b is the fracture aperture (L), and μ is the dynamic viscosity ($MT^{-1}L^{-1}$).

Traditionally unsaturated fractures have been considered to act as capillary barriers and contribute very little to water flow if fracture saturation, and hydraulic conductivity, are low (Wang and Narasimhan, 1985). However, more recent studies have suggested that rapid water infiltration rates through deep, unsaturated fractured media cannot be explained without the inclusion of preferential flow through unsaturated fractures (Dragila and Wheatcraft, 2001). Tokunaga and Wan (1997) demonstrated that significant water flow can still occur along unsaturated fractures through water films that exist on the surface of rough-walled fractures, particularly in media with a low-hydraulic conductivity matrix.

Water infiltration through hydrophobic soils is usually preferential with more rapid infiltration occurring through pores that exhibit hydrophobicity to a lesser degree (Bauters et al., 2000) or that are relatively large (Dekker and Ritsema, 2000).

Preferential flowpaths through hydrophobic soils have commonly been visualized with dye tracer experiments (*c.f.*, Lipsius and Mooney, 2006).

Flow of dense non-aqueous phase liquids (DNAPLs) through water saturated porous media is analogous to water flow through hydrophobic media. DNAPL is immiscible in water (Fetter, 1993) and the pressure of DNAPL must exceed the entry pressure of an underlying pore or fracture before it will enter the pore or fracture (Kueper and McWhorter, 1991). The entry pressure increases with decreasing pore diameter or fracture aperture (similar to Eq.[1.7]), therefore DNAPL will preferentially flow through the largest pores or fractures (Kueper and McWhorter, 1991; Steele and Lerner, 2001).

1.4.4.3 Evaporation

Evaporation occurs when a water vapor pressure gradient exists between the surface of a porous medium and the atmosphere (Fredlund and Rahardjo, 1993). The water vapor pressure at the surface of the medium decreases with increasing matric and osmotic suction of the pore water, where osmotic suction is the pressure developed in response to increased pore water solute concentrations (decreased water potential) (Fredlund and Rahardjo, 1993). Evaporative water vapor flux from the ground surface occurs by turbulent air flow and can be quantified by simultaneous, high frequency measurements of vertical wind speed and humidity (eddy correlation method) (Warrick, 2002).

1.4.5 S^0 block literature review

Bonstrom (2007), Pisz (2008), Smith (2009), and Bonstrom et al. (2009) describe previous work on S^0 blocks by the University of Saskatchewan research group of which the author of this study was a member. Bonstrom (2007) measured key parameters of S^0 blocks regarding porosity and water flow. Bonstrom (2007) determined that pore water pressures of 1-2 m were required for water to begin to enter pores in matrix S^0 with water contact angle measured at >110° (J. Lawrence, personal communications). Bonstrom (2007) measured fracture apertures >0.3 mm, and reported a mean vertical fracture aperture of 1.2 mm and a mean horizontal fracture aperture (as

measured on an exposed weathered block face) of 1.0 mm at the Phase 1 block. The mean pore diameter of matrix S^0 was 0.2 μm (n=9) (K. Bonstrom, personal communication). The mean vertical and horizontal fracture frequencies were 33.5 and 5.4 m^{-1}, respectively. Fracture orientation was random and the maximum aperture was 13.8 mm (frequency 0.02 m^{-1}). The fracture porosity (n_f) was estimated at 1.4%.

The density, fracture porosity (n_f), matrix porosity (n_m), fracture aperture and distribution, and K_s of the Phase 1 block was described by Bonstrom et al. (2009). They determined the average dry density of intact core samples to be 1.88 g/cm^3 (n=280, s.d.=0.07 g/cm^3) with no change in density with depth; the mean n_m was estimated at 9.3% (range 4.5 to 23%, n=280, s.d.=3.4 %), assuming a specific gravity of 2.07 g/cm^3. Bonstrom et al. (2009) suggested low sample recovery during coring (62 to 78%) may be due to samples with higher n_m being pulverized during coring. As a result, the actual n_m in the field may be higher than the reported mean. S^0 samples with higher (vuggy) porosity were associated with larger crystals and longer cooling times. They also measured the effective (interconnected) porosity for dense, intact S^0 samples to be 5.5 %.

The average K_s of intact S^0 samples (unfractured to the unaided eye) as measured in the laboratory was 1.7×10^{-6} m/s (n = 17, s.d. = 1.1×10^{-6} m/s) and ranged from 5.0×10^{-6} to 5.0×10^{-7} m/s (Bonstrom et al. 2009). Hydraulic conductivity values measured *in situ* by packer tests were considered estimates of field-saturated conditions (only the area immediately adjacent to water injection was saturated, Bonstrom, 2007). These field hydraulic conductivity values averaged 1.0×10^{-5} to 1.0×10^{-6} m/s for depths greater than 9 m, and are similar to a saturated silt or very fine-grained sand (Bear, 1972). Due to concerns regarding the *in situ* K_s test procedures and drilling methods, these tests and data are being re-evaluated by J. Ledding (graduate student, University of Saskatchewan; personal communications, July 2009).

Smith (2009) studied the control of temperature and microbes on S^0 oxidation rates in laboratory experiments and characterized the controls on the isotope composition of SO_4 produced from S^0 oxidation. Smith (2009) measured S^0 oxidation rates in reaction cells ranging from 0.16-0.98 $\mu g \cdot cm^{-2} \cdot d^{-1}$ with temperatures of 6-32°C

and Q_{10} values of 1.9-1.6, respectively. Greater than 95% of S^0 oxidation was attributed to autotrophic microbial activity.

Pisz (2008) developed a methodology for measuring viable and non-viable populations of S^0-oxidizing microorganisms and applied this methodology to samples from reactions cells and the Phase 1 S^0 block. S^0 oxidation was limited to bioreactors inoculated with microorganisms from S^0-block drainage, suggesting microbial activity controlled S^0 oxidation rates. S^0-oxidizers were present in S^0 block samples to a depth of 6 m. However most probably number counts of autotrophic S^0-oxidizers were limited to depths of 0-0.1 m suggesting S^0 oxidation rates may be greatest near the S^0 block surface.

1.4.6 H_2SO_4 overview

H_2SO_4 is a polyprotic acid which forms hydronium ions (H+) during hydration according to:

$$H_2SO_4 \rightarrow H^+ + HSO_4^- \quad [1.11a]$$

$$HSO_4^- \rightarrow H^+ + SO_4^{-2} \quad [1.11b]$$

The first H^+ (Eq.[1.11a]) dissociates freely in water while HSO_4 is a weak acid with a dissociation constant (K_a) of 0.012 (Eq.[1.11b]) (Clark and Fritz, 1997). The pH of a solution is defined as:

$$pH = -\log\{H^+\} \quad [1.12]$$

where $\{H^+\}$ is the H^+ activity equal to the H^+ concentration multiplied by an activity coefficient. The activity coefficient for concentrated solutions (ionic strength greater than 0.5 M, or pH=0.3 for a H_2SO_4 solution) can be estimated by Pitzer equations, an empirical set of equations that account for ion-ion interactions in concentrated solutions (Plummer et al., 1988).

As the pH decreases (acidity increases) the water potential of a solution decreases (i.e., osmotic suction increases) thereby decreasing the equilibrium water vapor pressure and relative humidity (RH). RH is defined as:

$$RH = \frac{P_{act}}{P_{sat}} \quad [1.13]$$

where P_{act} is the actual vapour pressure ($M \cdot L^{-1} \cdot T^{-2}$), and P_{sat} is the saturated vapour pressure ($M \cdot L^{-1} \cdot T^{-2}$).

A relationship between H_2SO_4 molality and RH is presented by Staples (1981).

1.5 References

Amos RT, KU Mayer, BA Bekins, GN Delin, and RL Williams. 2005. Use of dissolved and vapor-phase gases to investigate methanogenic degradation of petroleum hydrocarbon contamination in the subsurface. Water Resources Research 41, Art. No. W02001.

Baker BJ, MA Lutz, SC Dawson, PL Bond, and JF Banfield. 2004. Metabolically active eukaryotic communities in extremely acidic mine drainage. Appl. Envir. Microbiol. 70: 6264–6271.

Bauters TWJ, TS Steenhuis, DA DiCarlo, JL Nieber, LW Dekker, CJ Ritsema, J-Y Parlange, and R Haverkamp. 2000. Physics of water repellent soils. Journal of Hydrology. 231-232: 233-243.

Binning PJ, D Postma, TF Russell, JA Wesselingh, and PF Boulin. 2007. Advective and diffusive contributions to reactive gas transport during pyrite oxidation in the unsaturated zone. Water Resources Research 43(2), Art. No. W02414.

Bonstrom, K. 2007. Physical controls on water migration in elemental sulphur blocks. M.Sc. thesis, Department of Geological Sciences, University of Saskatchewan, Saskatoon, SK.

Bonstrom K, SL Barbour, and MJ Hendry. 2009. Physical and hydraulic characterization of fractured, hydrophobic, sulphur within above ground sulphur blocks. Under revision, Canadian Geotechnical Journal.

Broere W. 2008. New uses of the world's growing sulphur stockpiles. Accessed June 10 2009 www.shell.com/home/content/innovation/about_us/news_publications/shell_world_stories/2008/sulphur/

Brooks RH, and AT Corey. 1964. Hydraulic properties of porous media. Hydrology Paper 3, Colorado State University, Fort Collins, CO.

Cey E., D Rudolph, and R Therrien. 2006. Simulation of groundwater recharge dynamics in partially saturated soils incorporating spatially variable fracture apertures. Water Resources Research, **42**: W09413. doi:10.1029/2005WR004589.

Chapman SJ. 1989. Oxidation of micronized elemental sulphur in soil. Plant Soil 116: 69–76.

Clark ID and P Fritz. 1997. Environmental Isotopes in Hydrogeology. CRC Press.

Dekker LW and CJ Ritsema. 2000. Wetting patterns and moisture variability in water repellent Dutch soils. Journal of Hydrology, 231-232: 148-164.

Dragila MI, and SW Wheatcraft. 2001. Ch. 7 Free surface films. In Conceptual models of flow and transport in the fractured vadose zone. National Academy Press, Washington.

Fetter CW. 1993. Contaminant Hydrogeology. Prentice Hall, New Jersey.

Energy Resources Conservation Board (ERCB). 2008. Alberta's energy reserves 2007 and supply/demand outlook 2008-2017. ST98-2008, Calgary, AB.

Fredlund DG, and H Rahardjo. 1993. Soil mechanics for unsaturated soils. John Wiley & Sons Inc., Toronto, ON.

Guarracino L. 2006. A fractal constitutive model for unsaturated flow in fractured hard rocks. Journal of Hydrology, **324**: 154-162.

Harries JR, and AIM Ritchie. 1985. Pore gas composition in waste rock dumps undergoing pyritic oxidation. Soil Science. 140(2): 143-152.

Hillel D. 1998. Environmental Soil Physics. Academic Press, St. Louis.

Janzen HH and JR Bettany. 1987a. Measurement of sulfur oxidation in soils. Soil Science 143(6): 444-452.

Jaggi RC, MS Aulakh, and R Sharma. 1999. Temperature effects on soil organic sulphur mineralization and elemental sulphur oxidation in subtropical soils of varying pH. Nutr. Cycl. Agroecosys. 54: 175–182.

Janzen HH and JR Bettany. 1987b. The effect of temperature and water potential on sulfur oxidation in soils. Soil Science 144(2): 81-89.

Kitto M. 2005. Sulphur supply/demand balance: the outlook to 2013. Proceedings of AFA 11th International annual fertilizer conference and exhibition. 1–3 Feb. 2005. Cairo, Egypt.

Knickerbocker C, DK Nordstrom, and G Southam. 2000. The role of "blebbing" in overcoming the hydrophobic barrier during biooxidation of elemental sulphur by Thiobacilllus thiooxidans. Chemical Geology, **169**: 425-433.

Kosich D. 2008. Sulphur, potash prices soar last month as base and precious metals decline. International Business Times, June 20.

Kueper BH, and DB McWhorter. 1991. The behavior of dense, nonaqueous phase liquids in fractured clay and rock. Ground Water. 29(5): 716-728.

Laishley EJ, RD Bryant, BW Kobryn, and JB Hyne.1986. Microcrystalline structure and surface area of elemental sulphur as factors influencing its oxidation by *Thiobacillus albertis*. Can. J. Microbiol. 32: 237–242.

Lawrence JR and JJ Germida. 1988b. Relationship between microbial biomass and elemental sulfur oxidation in agricultural soils. Soil Sci. Soc. Am. J. 52(3): 672–677.

Li P and AC Caldwell. 1966. The oxidation of elemental sulphur in soil. Soil Sci. Soc. Am. Proc. 30: 370–372.

Lide DR (ed.), 2003. CRC Handbook of Chemistry and Physics, 84th Edition. CRC Press, Boca Raton, Florica; Section 4, Properties of the elements and inorganic compounds, heat capacity of the elements at 25^{o}C.

Lipsius K, and SJ Mooney. 2006. Using image analysis of tracer staining to examine the infiltration patterns in a water repellent contaminated sandy soil. Geoderma, 136: 865-875.

Lizama HM, PA Zielinski, LD Kerby, and CC Abraham. 2002. Comparison of biooxidation with carbon dioxide assimilation during bacterial growth on ferrous ion or elemental sulfur. Biotech. Bioeng. 77(1): 111–117.

Lyklema J. 1995. Fundamentals of interface and colloid science. Academic Press, New York, N.Y.

Massmann J and DF Farrier. 1992. Effects of atmospheric pressures on gas transport in the vadose zone. Water Resources Research 28(3): 777-791.

Moldrup P, T Olesen, S Yoshikawa, T Komatsu, and DE Rolston. 2004. Three-porosity model for predicting the gas diffusion coefficient in undisturbed soil. Soil Science Society of America Journal 68: 750-759.

Mendoza CA and EO Frind. 1990. Advective-dispersive transport of dense organic vapors in the unsaturated zone 1. Model development. Water Resources Research 26(3): 379-387.

Meyer B. 1977. Sulphur, energy and environment. Elsevier Scientific, Amsterdam, Netherlands.

Nor YM and MA Tabatabai. 1977. Oxidation of elemental sulphur in soils. Soil Sci. Soc. Am. J. 41: 736–741.

Pisz, J. 2008. Characterization of extremophilic sulfur oxidizing microbial communities inhabiting the sulfur blocks of Alberta's oil sands. M.Sc. Thesis, Dept. Soil Science, College of Agriculture, University of Saskatchewan, Saskatoon, SK.

Plummer LN, DL Parkhurst, GW Fleming, and SA Dunkle. 1988. U.S. Geol. Survey Water-Resour. Invest. Report 88-4153.

Skiba U and M Wainwright. 1984. Oxidation of elemental S in coastal-dune sands and soils. Plant Soil 77: 87–95.

Smith LA. 2009. Defining controls of elemental sulphur oxidation using stable isotopes. M.Sc. thesis dissertation, Department of Geological Sciences, University of Saskatchewan, Saskatoon, SK.

Staples BR. 1981. Activity and osmotic coefficients of aqueous sulfuric acid at 298.15 K. J. Phys. Chem. Ref. Data, vol 10(3), 779-798.

Steele A and DN Lerner. 2001. Predictive modelling of NAPL injection tests in variable aperture spatially correlated fractures. Journal of Contaminant Hydrology. 49:287-310.

Syncrude Canada Ltd. 2004a. Geochemical characterization of a large sulphur block at Syncrude: Results from the 2003 field investigation. June 21, 2004, Fort McMurray. AB.

Syncrude Canada Ltd. 2004b. Geo-environmental observations of 17 sulphur blocks in Alberta. Research Dept. Progress Report 33(2), Fort McMurray, AB.

Thorstenson DC and DW Pollock. 1989. Gas transport in unsaturated zones: multicomponent systems and adequacy of Fick's laws. Water Resources Research 25(3): 477-507.

Tokunaga TK and J Wan. 1997. Water film flow along fracture surfaces of porous rock. Water Resources Research. 33(6): 1287-1295.

Wang JSY and TN Narasimhan. 1985. Hydrologic mechanisms governing fluid flow in a partially saturated, fractured, porous medium. Water Resources Research. 21(12): 1861-1874.

Warrick AW. 2002. Soil Physics Companion. CRC Press, New York.

Wen G, JJ Schoenau, T Yamamoto, and M Inoue. 2001. A model of oxidation of an elemental sulfur fertilizer in soils. Soil Sci. 166(9): 607–613.

2.0 WATER FLOW AND STORAGE IN FRACTURED, UNSATURATED SULPHUR BLOCKS

Preface

Water contact with S^0-oxidizing microbes is a requirement for the microbial oxidation of S^0, therefore, H_2SO_4 production (S^0 oxidation) in S^0 blocks will only occur where water is present. This manuscript focuses on quantifying the location and concentrations of water storage, and the rate and pathways of water infiltration through S^0 blocks. The volume of water stored for drained conditions was quantified by measuring depth profiles of water concentration in a commercial-scale S^0 block. The porosity in which this water was stored was determined by measuring the relative water repellency in the matrix and fracture porosity, and by dye tracer tests that visually demonstrated water infiltration pathways. The total porosity available for water storage and hydraulic conductivity in S^0 blocks was estimated by modelling transient pressure head and outflow responses to rainfall events. Although S^0 blocks are a very complex medium regarding water flow and storage (fractured, unsaturated, hydrophobic), a relatively simple working model is presented that will be useful for the design and evaluation of S^0 storage strategies.

Reference: Birkham TK, MJ Hendry, SL Barbour, SK Carey, JR Lawrence, and R Lewko. Water flow and storage in fractured, unsatured sulphur blocks. Submitted to Canadian Geotechnical Journal, June 2009.

2.1 Abstract

Water is a primary control on the generation of acidic (H_2SO_4) effluent from commercial-scale sulphur (S^0) blocks. Although clean S^0 is strongly hydrophobic, microbial colonization of fracture faces and friable S^0 generates localized hydrophilic conditions. Infiltration occurs preferentially along discrete fractures and in areas of friable S^0. Surface evaporation rates are low (mean 0.2 mm/d) and >90% of rainfall infiltrates and rapidly drains from the blocks. A conceptual model to describe the flow and storage of water in S^0 blocks was developed and tested. The S^0 blocks were represented as a hydrophilic equivalent porous medium for water migration. Vertical infiltration and lateral drainage at the base of the blocks were quantified using a 1-D analytical solution and 2-D numerical model, respectively. Specific yield (S_y) and saturated hydraulic conductivity (K_s) values were estimated (0.8 to 4.4%, and 1×10^{-1} to 1×10^{-3} m/s, respectively) by comparing measured hydraulic head and outflow responses to rainfall events. Given that commercial-scale S^0 blocks are constructed in a similar manner worldwide, the results of this study are considered widely applicable in the design of S^0 block storage facilities that minimize water availability and H_2SO_4 production in S^0 blocks.

2.2 Introduction

Elemental sulphur (S^0) has been stockpiled over the past 20 years due to a global S^0 surplus (Ober 2002). Increased S^0 production at petroleum refineries, natural gas plants, coking plants, and non-ferrous metal smelters (Ober 2008) combined with a decrease in S^0 prices from $300 to ~$25 USD per tonne from 1982 to 2002 has forced tens of Mt to be stockpiled at industrial sites. This is particularly common in regions where transportation costs are relatively high, such as at more remote sites including northern Canada, the Middle East, and the Caspian Sea region (Proce 2006). Increased demand from 2005-2008 (ERCB 2008) resulted in S^0 prices as great as $700 US per t (Kosich 2008) and mining of S^0 from the most accessible stockpiles. However, a S^0 surplus and continued stockpiling is expected to continue from 2011-2017 (ERCB 2008).

Canada was the world's largest S^0-producing country in 2007 (Ober 2008) with 11.6 Mt stockpiled as of April 2008 (ERCB 2008). Bitumen upgrading at oilsands mining operations in northern Alberta resulted in 1.5 Mt of stockpiled S^0 in 2007 with annual stockpiling expected to increase to 5.3 Mt by 2017 (ERCB 2008).

S^0 is commonly stored by pouring molten S^0 (135 to 145 °C) in a confined area on the ground surface where it solidifies (at 115 °C) in lifts approximately 0.1 m thick. Gradually, a large S^0 block is built up with typical footprint lateral dimensions of 100-200 m and heights of 10-20 m. Some of the stored S^0 within these above-ground blocks will oxidize to H_2SO_4 and this acid is carried to the natural environment as precipitation percolates through the blocks. Most, if not all sites more than 20 years old, experience problems with groundwater contamination as a result of S^0 oxidation to H_2SO_4 (Syncrude 2004a). Drainage waters seeping from the base of these S^0 blocks typically have low pH (0.4-1.0) and high SO_4 concentrations (12,000-34,000 mg/L) (D. Wainwright, B. Goliss, personal communications), and soil and groundwater acidification and soil salinization adjacent to the blocks can be a concern for refinery operators and government regulators.

Oxidation of S^0 to SO_4 (i.e., production of H_2SO_4) is dependent on microbial activity (Janzen and Bettany 1987a). Because microbial activity requires at least a microscopic film of water (Postgate 2000), minimizing water availability in blocks is potentially an effective approach to limiting H_2SO_4 production. Minimizing the percolation of water through the S^0 blocks will also reduce the volume of H_2SO_4 effluent from the blocks to the surrounding environment.

Characterization of the rates and pathways of water migration as well as moisture distribution in S^0 blocks is complex. The blocks are typically unsaturated and S^0 is hydrophobic (Lyklema 1995); as a result, typical relationships between hydraulic conductivity, moisture content, and pore-water pressure for unsaturated soils may not apply. In addition, S^0 blocks are heavily fractured as a result of volume change during freezing and subsequent mineralogical changes (Bonstrom et al. 2009). Given the importance of water availability for acid production and effluent generation, and the potential complexity of water flow through the blocks, the objectives of this study were to quantify the distribution and controls on moisture water availability in commercial-

scale S^0 blocks. The results of this study should be applicable to other S^0 blocks as the techniques used to construct S^0 blocks are similar worldwide (P. Davis, personal communication 2008).

This study was conducted at two commercial-scale blocks (Phase 1 and 2 blocks, Figure 2.1) located at the Syncrude Canada Ltd. oilsands mine in northern Alberta, Canada (57°02'34.89"N, 111°38'36.14"W). A water balance for the S^0 blocks was quantified by measuring precipitation and actual evaporation at the surface of the Phase 1 block and outflow rates from the Phase 2 block. Storage of water in the Phase 1 block was quantified by measuring depths profiles of moisture content, and the time dependent rise of water levels and the release of water from the base of the block in response to rainfall events. A 1-D analytical solution was used to quantify vertical water infiltration through the blocks, and a 2-D numerical model was used to simulate the rise and fall of the unconfined flow system that develops at the base of the blocks in response to rainfall events and subsequent drainage. The analytical solution and numerical model were used in tandem to simulate hydraulic head and outflow responses to rainfall events and to estimate specific yield (S_y) and saturated hydraulic conductivity (K_s) values. Water repellency measurements of matrix and fractured S^0, dye tracer testing, and microbial analyses of matrix and fractured S^0 were used to confirm and interpret the modelling results.

2.3 Field site and S^0 characterization

The Phase 1 S^0 block was constructed between 1994 and 2004. At completion, it contained 895,633 m^3 of S^0, was 359 m long x 168 m wide (area at base of 60,312 m^2), and at GTVP-03-07 (Figure 2.1) was 17.5 m high (Syncrude 2004b). The Phase 2 block was constructed between 1997 and 2005 and is located approximately 100 m west of the Phase 1 block. At completion, it was 261 m long x 334 m wide (area at base of 87,174 m^2) (Syncrude 2004b), with an average height of 25 m (R. Carter, personal communication).

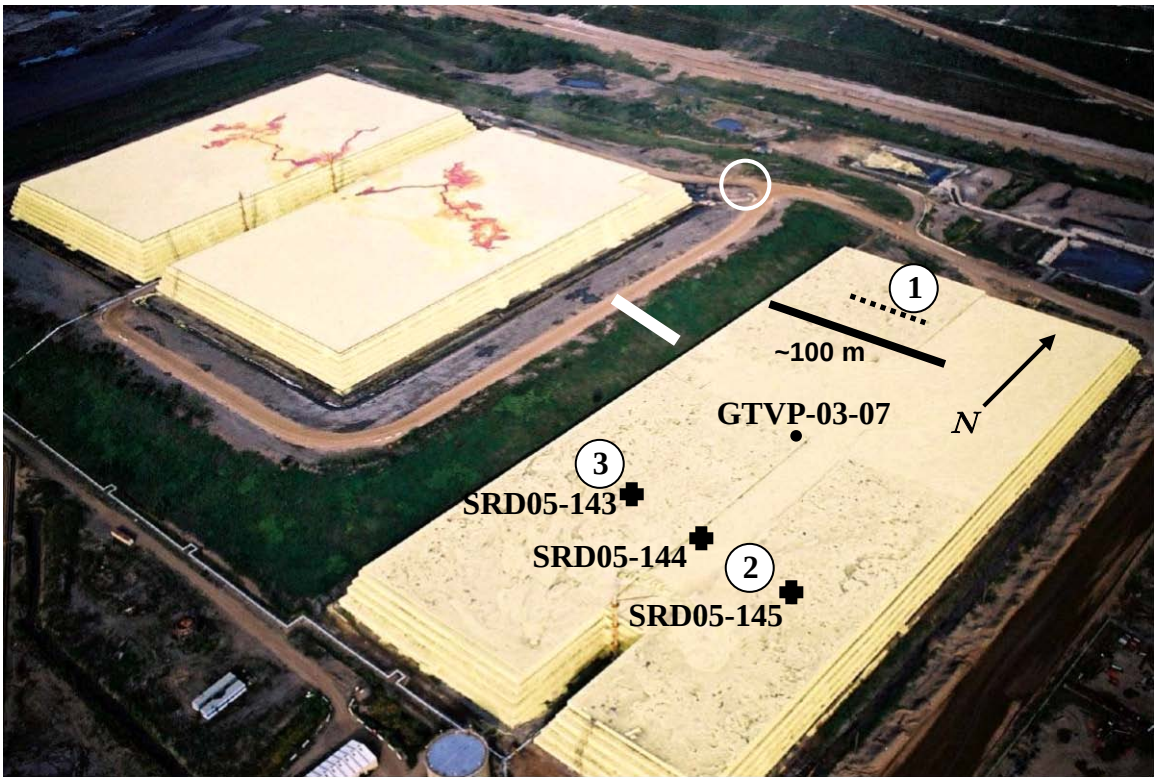

Figure 2.1. Instrumentation site map of Phase 1 (lower right) and Phase 2 (under construction, upper left) S^0 blocks at Syncrude Canada Ltd. oilsands mine in 2003. Black crosses on the Phase 1 block mark the drilling locations for moisture content sampling. The dot symbol marks the installation of the vibrating wire piezometer 1 m above the base of the Phase 1 block. The eddy covariance station was installed approximately 5 m from GTVP-03-07. The dotted line at the north end of the Phase 1 block represents the cross-sectional line along which dye tracer tests were conducted and samples for water repellency testing collected. Dark texturing on the surface of the Phase 1 block is wind-blown sediment. Locations 1, 2, and 3 on the Phase 1 block mark the locations of sediment sampling for water repellency testing. The Phase 2 weir is highlighted by a white circle at the north-east corner of the block. The flow of molten S^0 in channels (orange) is visible on the Phase 2 block. The passageways for pouring towers through the center of the Phase 2 block, and through the Phase 1 block, are also evident.

Both blocks were constructed by pouring molten S^0 from three towers into two areas east and west of the towers contained by shallow forms (lift thicknesses $\leq$0.12 m). The S^0 flowed by gravity to areas of lower elevation. After the S^0 on either side of the towers reached the desired height the towers were dismantled and S^0 was poured into the passageway between the east and west blocks (Figure 2.1).

S^0 undergoes shrinkage after pouring due to the effects of freezing and mineral change. S^0 shrinks by 7% during freezing and by 5.5% during the mineral change from monoclinic to rhombic crystal structure (Meyer 1977). The later transformation occurs over several days at temperatures less than 95°C. These combined volume changes result in vertical and horizontal fracturing of the S^0 blocks.

The Phase 1 and 2 blocks were constructed on compacted clay liners (approximately 1 m thick). More than 45 m of *in situ* McMurray Formation Oil Sand underlies the Phase 1 liner and approximately 20 m of coke underlies the Phase 2 liner. The Phase 1 block was constructed in a topographic low with its base elevation approximately 20 m below the base elevation of the Phase 2 block. The location of the Phase 1 block at the base of a hill allowed the construction of a vehicle ramp onto its top surface. As only the top of the Phase 1 block was accessible to heavy equipment, all activities requiring drilling and instrumentation were conducted on the Phase 1 block.

The density, fracture porosity (n_f), matrix porosity (n_m), fracture aperture and distribution, and K_s of the Phase 1 block was described by Bonstrom et al. (2009). They determined the average dry density of intact core samples to be 1.88 g/cm^3 (n = 280, s.d. = 0.07 g/cm^3) with no change in density with depth; the mean n_m was estimated at 9.3% (range 4.5 to 23%, n = 280, s.d. = 3.4 %), assuming a specific gravity of 2.07 g/cm^3. Bonstrom et al. (2009) suggested that low sample recovery during coring (62 to 78%) may be due to samples with higher n_m being pulverized during coring. As a result, the actual n_m in the field may be higher than the reported mean. S^0 samples with higher (vuggy) porosity were associated with larger crystals and longer cooling times. They also measured the effective (interconnected) porosity for dense, intact S^0 samples to be 5.5 %.

Bonstrom (2007) measured apertures >0.3 mm with digital calipers, and reported a mean vertical fracture aperture of 1.2 mm and a mean horizontal fracture aperture (as measured on an exposed weathered block face) of 1.0 mm at the Phase 1 block. The mean vertical and horizontal fracture frequencies were 33.5 and 5.4 m^{-1}, respectively. Fracture orientation was random and the maximum vertical fracture aperture was 13.8 mm (frequency 0.02 m^{-1}). The fracture porosity (n_f) was estimated at 1.4%.

The average K_s of intact S^0 samples (unfractured to the unaided eye) as measured in the laboratory was 1.7×10^{-6} m/s (n = 17, s.d. = 1.1×10^{-6} m/s) and K_s ranged from 5.0×10^{-6} to 5.0×10^{-7} m/s (Bonstrom et al. 2009). Hydraulic conductivity values measured *in situ* by packer tests (Bonstrom, 2007) were considered estimates of field-saturated conditions (only the area immediately adjacent to water injection was saturated). These field hydraulic conductivity values averaged 1.0×10^{-5} to 1.0×10^{-6} m/s for depths greater than 9 m, and are similar to a saturated silt or very fine-grained sand (Bear, 1972). *In situ* hydraulic conductivity test procedures and drilling methods are being refined and re-evaluated (personal communication, J. Ledding).

Bonstrom (2007) conducted water intrusion porosimetry tests on S^0 and measured a contact angle of >110° between the S^0 and water. The contact angle is defined as the angle from the surface of the solid material to the inside of the water droplet, with hydrophobic material having a contact angle with water of greater than 90°. Due to the hydrophobicity of S^0, water was found to begin to enter the matrix porosity of intact S^0 pieces at water-entry pressure heads of 1 to 2 m, with full saturation of the matrix requiring pressure heads of at least 100 m.

2.4 Materials and Methods

2.4.1Water repellency testing

The degree of hydrophobicity was measured on samples of Phase 1 S^0 (n = 21) and wind-blown soil sediment from the surface of the Phase 1 block (n = 3) using a water drop penetration test. This is an empirical test commonly used to measure the water repellency of soils (Dekker and Ritsema 2000). Water drops are placed on smoothly prepared soil samples and the median penetration time is used to quantify the degree of water repellency as described in Table 2.1.

For the sediment samples collected from the S^0 block, three drops (~0.5 mL each) of water were placed on air-dried samples and the penetration time of each drop was measured and recorded. The time for each of three water drops to disperse, or spread over the S^0 sample so the contact angle approached zero, was measured. The water drops were placed onto each S^0 fracture surface as well as the exposed matrix of

Table 2.1. Water repellency classification after Dekker and Ritsema (2000).

Water drop dispersion time (s)	Classification
<5	Wettable; not water repellent.
5 to 60	Slightly water repellent
60 to 600	Strongly water repellent
600 to 3600	Severely water repellent
>3600	Extremely water repellent

each sample. The water was dropped onto the sample from a height of not more than 0.5 cm at temperatures of 22°C.

S^0 samples were collected along three randomly-selected vertical cross-sections (Figure 2.1) on 16 May 2007. The vertical sections were approximately 0.3 m long and excavated to depths of 0.58, 0.51, and 0.26 m below the block surface. Samples lying along fractures were carefully excavated with a hammer and 2.54-cm wide chisel so the fracture surface was preserved. Ten samples were recovered from the 58-cm deep cross-section and seven samples from the 51-cm deep cross-section. Another four samples were recovered from a cross-section that followed the face of a large (2 mm aperture) fracture to a depth of 26 cm. The depth interval and orientation of each sample was recorded in the field at the time of collection. Each sample was placed in a sterile plastic bag, transported to the lab, and air-dried for 24 hr before water repellency tests were conducted.

The three samples of wind-blown sediments (~300 g each) from the surface of the Phase 1 S^0 block were collected on 18 September 2006 (locations 1, 2, and 3; Figure 2.1). The samples were collected by scraping sediment from the surface into sterile plastic bags, taking care to minimize the addition of S^0 to the sample. Sediment was also observed along fractures in the block, presumably transported and deposited on the fracture faces by infiltrating water. Sediment samples were air-dried within two days of collection.

2.4.2 Contact angle and surface conditioning film analyses

The relationship between hydrophobic conditions and the presence of microbial biofilm was investigated by measuring surificial water contact angles and visualizing the associated biofilms. Water contact angles of matrix and fractured S^0 surfaces were measured for samples (n = 5) collected aseptically from the Phase 1 block (depths of 0-0.2 m) using the static drop method and measuring the angle within the water phase as described by Skodowska et al. (1999). The contact angle is defined as the angle between the surface of the water drop and the surface of the S^0 on the water side of the angle. The chemistry of the conditioning film was investigated using lectin binding assays as described by Neu et al. (2001). In brief, a panel of fluorescently conjugated lectins with specificity for a range of carbohydrates and sugars (Table 2.2) were applied to the surface of the S^0, incubated for 20 min, and washed three times to remove unbounded lectin. The result of the binding was imaged using confocal laser microscopy (Bio-Rad MRC 1024, Zeiss, Jena, Germany) and water immersible objectives (40X, 63X, Nikon, Tokyo, Japan).

Table 2.2. Lectins binding to fracture S^0 surfaces and their target sugars and carbohydrates.

Lectin	Target
Tetragonolobus purpurea	terminal α-L-fucose
Arachis hypogaea	terminal β-galactose,
Canavalia ensiformis	dextrans, fructans, glycoproteins, polysaccharides
Glycine max	terminal a and β N-acetyl-D-galactosamine
Ulex europaeus	external α (1,2) linked fucose
Lens culinaris	Mannose, glucose, glycoconjugates
Galanthus nivalis	Mannose, α (1,3)Mannose, mannose type glycoproteins
Vicia villosa	terminal α -GalNAc, sialated O-linked polysaccharides
Triticum vulgaris	chitin (esp. fungal cell wall), N-acetyl neuraminic acid (Neu5Ac, sialic acid), glycoproteins, fetuin, chitobiose
Helix pomatia	α -N-acetyl-D-galactosamine
Artocarpus integrifolia	α -D-galactose and oligosaccharides
Solanum tuberosum	oligosaccharides containing β (1,4) linked GlcNAc, N-linked poly N-acetyllactosamine
Maclura pomifera	α -D-galactose, mellibiose, bacterial polysaccharide and antifreeze glycoprotein
Phaseolus coccineus	fetuin, not inhibited by monosaccharides

2.4.3 Dye tracer tests

To visualize the migration path of infiltrating precipitation, two dye tracer tests were conducted on the top of the Phase 1 block (Figure 2.1) on 21 April 2006. In both tests, brilliant Blue FCF at a concentration of 4 g/L was used because of its high visibility on yellow S^0, low health risks, and proven usefulness in mimicking water infiltration through porous media (Flury and Fluhler 1994; Lipsius and Mooney 2006).

The dyed water was ponded in square wooden forms glued to the block surface with insulating foam. The areas tested were 1,600 cm^2 (Test 1) and 2,500 cm^2 (Test 2). The edges of the forms were glued 10 cm from the edge of an approximately 70-cm high ledge. The forms for the dye tracer tests were located in areas where fracture apertures were <2 mm and similar to the mean vertical aperture of 1.2 mm. Based on preliminary infiltration tests with water (data not presented), areas where visible fractures were not present resulted in extremely slow infiltration (no measurable infiltration after 1 h) and areas where fracture apertures were >2 mm resulted in water escaping beneath the wooden form. The volume of dyed water poured into the forms for Test 1 and Test 2 was 10 and 11 L, respectively, which resulted in initial ponded depths of 62.5 and 44 mm. Approximately 15 hr after the dyed water infiltrated the block (infiltration times of 3 h 10 min and 30 min, respectively), vertical cross-sections beneath the wooden forms were cut into the S^0 block using a hammer and a 3.8 cm wide chisel. For Test 1, vertical cross-sections (0.7 m deep and 1.1 m wide) were chiseled at the edges (0.1 m from the vertical ledge) and centre of the form (0.3 m from the vertical ledge). For Test 2, vertical cross-sections (0.65 m deep and 1 m wide) were chiseled 0.05 m inside the form (0.15 m from the ledge), 0.25 m inside the form (0.35 m from the ledge), and 0.45 m inside the form (0.55 m from the ledge).

Each cross-section was excavated and photographed within ~1 h with a Canon Powershot A540® camera. The digital photographs were analyzed for dye coverage using ImageJ software (public domain, developed by the Research Services Branch of the NIMH, http://rsb.info.nih.gov/ij/) by converting the image from RGB format to its red, green, and blue components. The red slices of these stacked images provided the best contrast between the dyed and non-dyed areas of the cross-section and were used to digitally measure the area covered by the dye tracer.

The dye solution used in these tracer tests had a contact angle with fresh matrix S^0 of <90° (data not shown), with a single drop soaking into a piece of fresh matrix S^0 in ~30 min. As a result, the spreading of the dye tracer into the matrix S^0 and the area of dye coverage was likely greater than would be the case for infiltrating rain and melt water.

2.4.4 Moisture content distribution

Depth profiles of moisture content were measured on samples collected from the Phase 1 block on 25-27 April 2006. The samples were collected from augered holes at SRD06-143, -144, and -145 (located within 2 m of SRD05-143, -144 and -145, respectively; Figure 2.1) to total depths of 6 m. The auger drilling powdered the intact S^0 and yielded few solid sample diameters greater than 1 cm. Continuous samples of powdered S^0 were collected between 0 and 3 m at 10-cm intervals. From 3 to 6 m, 10 cm of S^0 was collected every 50 cm. The powdered S^0 was removed from the boreholes using a shop vacuum and placed in ice-packed coolers in sealed plastic bags Samples were analyzed for moisture content on the same day as collection. Moisture was evaporated by oven-drying approximately 200 to 250 g of sample at 90°C for approximately 30 hr. The balance used for weighing moisture content samples had a precision of ± 0.01 g.

2.4.5 Pore-water pressure head

A vented vibrating wire piezometer (Slope Indicator®) was installed on 10 September 2003, at GTVP-03-07 (Figure 2.1) on the Phase 1 block to measure the pore-water pressure within the block. The piezometer tip was lowered down a 0.203-m diameter cored hole to a depth of 16.5 m and cemented into place with cement-bentonite grout. The piezometer tip was 1 m above the base of S^0 block. Frequency signals from the vibrating wire piezometer were measured manually using a Slope Indicator® VW data recorder from 11 September to 9 October 2003, and converted to pore-water pressure head using a factory-supplied calibration equation with temperature and elevation correction. From 9 October 2003 to 3 June 2005, frequency signals from the

vibrating wire piezometer were measured 61 times at irregular intervals ranging from daily to monthly.

2.4.6 Evaporation and energy balance

The energy balance for the S^0 block surface can be described as follows:

$$R_n = L_v E + C + G + \varepsilon \quad [2.1]$$

where R_n is net radiation (W/m^2), L_vE is latent heat exchange (W/m^2, or evaporation, E, when divided by the latent heat of vaporization, L_v), C is convective sensible heat exchange (W/m^2), G is S^0 surface heat conduction flux into the block (W/m^2), and ε is a residual flux density associated with errors (W/m^2).

The eddy covariance method, a statistical method to measure vertical turbulent fluxes of water vapour, was used to measure L_vE and H in Eq.[2.1]. A weather station was used to measure air temperature and humidity, net radiation, incoming radiation, wind speed and direction, and rainfall on the Phase 1 block (Figure 2.1; Table 2.3).

Table 2.3. Summary of instrumentation for weather station and eddy flux system and equation parameters associated with the respective instrumentation.

Environmental variable	Instrument	Manufacturer	Instrument height (m)	Estimated error
Weather station				
Air temperature	HMP35CF	Vaisala	2	± 0.4°C
Relative humidity	HMP35CF	Vaisala	2	± 2%
Net radiation	Q7	REBS	2	± 5%
Short-wave radiation	SP-Lite	Kipp and Zonen	3	± 5%
Wind speed	Wind monitor	R.M. Young	3	± 0.3 m/s
Wind direction	Wind monitor	R.M. Young	3	± 3°
All-wave radiation	CNR1	Kipp and Zonen	2	± <5%
Eddy flux system				
Sensible heat flux	CSAT3	Campbell Scientific	1.7	± 30%
Latent heat flux	LI-7500 and CSAT3	LI-COR and Campbell Scientific	1.7	± 30%
Ground heat flux	CM3	Campbell Scientific	-0.05	± 10%

All instruments were connected to a CR23X datalogger (Campbell Scientific®), measured every 10 s, and an average or cumulative record logged every half-hour from 4 May to 16 September 2005. Evaporation and sensible heat flux were measured using a sonic anemometer (CSAT3; Campbell Scientific®) and fine-wire thermometer and an open-path gas analyzer (LI-7500; Li-Cor®) mounted on a 1.5 m boom and pointed into the prevailing wind direction. The mid-points of the sensors were 1.7 m above the ground and 0.2 m apart. Various wind components were measured at 10 Hz and their fluctuations were recorded every half hour using a CR-23X data-logger (Campbell Scientific®). Ground heat flux was measured using a heat flux plate placed at 0.05 m depth (Table 2.3), underneath fractured surficial S^0 pieces. Further details of the evaporation energy balance measurements are presented by Carey et al. (2005). Potential evaporation was measured daily from a water-filled pan (1.2-m diameter) at a meteorological station ~10 km from the S^0 blocks.

2.4.7 Drainage rates

A weir with a 45° V-notched opening was installed in the fall of 2005 at the northeast corner of the Phase 2 S^0 block (Figure 2.1), at a point past which all drainage water from the block flowed. Water levels approximately 2 m upstream of the weir were measured using a Campbell Scientific® SR50A-L sonic depth sensor and recorded on an hourly basis using a Campbell Scientific® CR-10X datalogger from 23 March to 2 November 2006. The flow rate over the weir was calculated using:

$$Q = 0.825h^{2.5} \qquad [2.2]$$

where Q is the flow rate (m^3/min) and h is the height of water above the channel bottom (m).

Maintenance checks were made on the weir and depth sensor every two weeks, at which time any sediment buildup was removed.

2.4.8 Water flow modelling

Water flow was assumed to be limited to the fractured network of the blocks given the hydrophilic conditions that develop on the fracture faces in the S^0 block and the extreme hydrophobicity of the matrix S^0. The fractured network was simplified for

modeling purposes and represented by a hydrophilic, equivalent porous medium. Guarracino (2006) concluded that models for quantifying the K and volumetric moisture content (θ_w) of fractured networks as functions of pore-water suction (ψ) were similar to those for porous media (i.e. Brooks-Corey model) when the range of fracture apertures comprising the network was greater than approximately five orders of magnitude. The full range of fracture apertures in the S^0 blocks could not be quantified as the digital caliper could not measure fracture apertures less than 0.1 mm (Bonstrom, 2007; maximum fracture aperture in blocks was 13.8 mm). However, it was assumed that fracture apertures substantially less than 0.1 mm did exist in the blocks and, therefore, the Brooks-Corey model could be applied to the fractured network in the S^0 blocks.

Water flow through the S^0 blocks was conceptually divided into two components: vertical infiltration of precipitation from the top to the bottom of the blocks, and horizontal drainage through the base of the blocks (Figure 2.2). Numerical modelling of vertical infiltration was non-convergent given the unsaturated conditions of the blocks and extremely steep air-entry pressures of the , therefore an analytical solution (Lessoff and Indelman 2004) was used to simulate one-dimensional vertical infiltration in response to rainfall events. Horizontal drainage through the base of the block was modelled using a two-dimensional finite element numerical model (SEEP/W by Geo-slope®). The calculated water fluxes with time from the bottom boundary of the analytical solution were used as the water flux input to the top boundary of the two-dimensional numerical model, which was used to simulate the rise and fall of the water table at the base of the blocks in response to horizontal water flow and water outflow at one end of the block. The K_s and S_y of the blocks were estimated by varying their values in the analytical and numerical models and comparing simulated and measured hydraulic heads at the base of the Phase 1 block, and drainage rates at the outflow weir for the Phase 2 block in response to rainfall events. The response of hydraulic head and outflow rates were simulated for relatively intense and isolated rainfall events. Hydraulic head and drainage responses to low intensity rainfall were not distinct enough to use for comparison, and extended rainy periods or frequent low-intensity rainfall events were beyond the scope and sophistication of the modelling methodology.

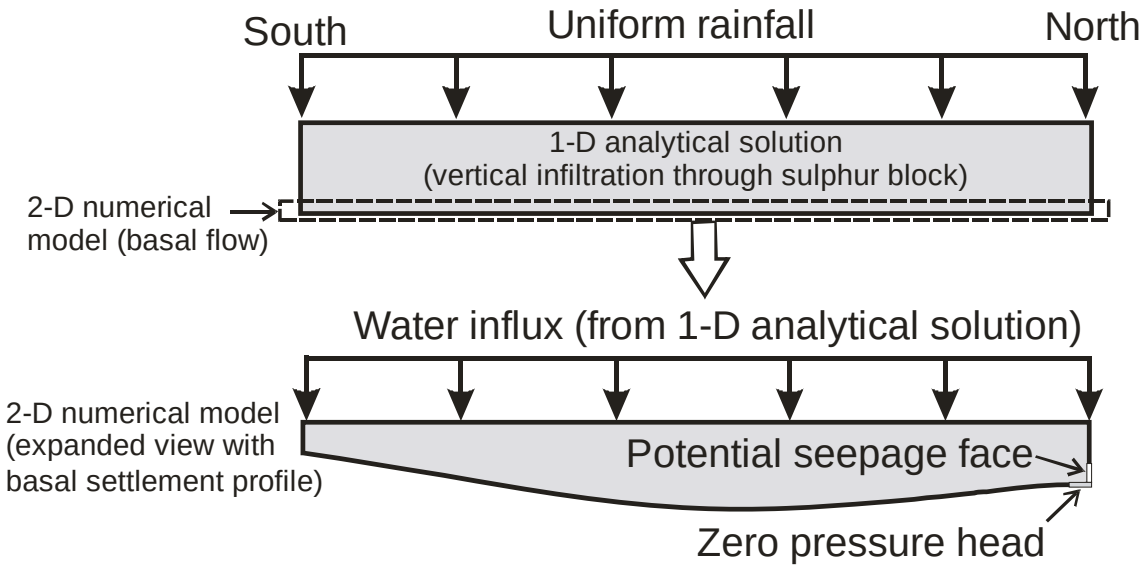

Figure 2.2. Conceptual schematic of sulphur block water flow modelling for vertical infiltration and two-dimensional basal flow, with basal discharge occurring from the north end of the block.

We acknowledge the hydraulic head and outflow modelling in this study are based on a few key assumptions. The two-dimensional model of water flow along the base of the S^0 blocks is an approximation of what is likely a more complex three-dimensional system that included water flow with an east-west component, in addition to outflow from the north end of the block. The S^0 blocks are also assumed to be homogenous with respect to S_y and K_s and, in the two-dimensional modelling, the S_y and K_s estimates for the base of the S^0 block are assumed to be representative of the entire depth of the block. Despite these limiting assumptions, the modelling presented in this study provides preliminary approximations of bulk field values of S_y and K_s which, to this point, have not been quantified.

Vertical infiltration: The one-dimensional analytical solution (Lessoff and Indelman 2004) was based on the assumption that a pulse of water was applied at a constant rate for a specified time period to an initially dry soil (residual moisture content, θ_r). Water flow was assumed to be gravity-driven with a unit hydraulic gradient, which is widely applicable to drainage of unsaturated porous medium (DiCarlo, 2003). The hydraulic conductivity (K)-saturation (S) relationship in the analytical solution was estimated by the Brooks and Corey (1964) relation:

$$K(S) = K_s S^{\frac{1}{\beta}} \quad [2.3]$$

where $S = (\theta_w - \theta_r) / (n - \theta_r)$ with θ_w = water-filled porosity and n = total porosity, and β is an empirical parameter.

The Brooks-Corey relationship (Eq [2.3]) is reported to be a reasonable estimation for fractured networks with rough walls (Cey et al. 2006) and with a large range of fracture apertures at low pressure heads (Guarracino 2006). A β parameter of 0.33 was assumed for Eq [2.3], comparable to a uniform sand (Fredlund and Rahardjo 1993). Daily rainfall data were obtained from the Environment Canada online climate database (www.ec.gc.ca) for the Mildred Lake station, which is approximately 15 km west of the S^0 blocks. The rainfall intensity was estimated by assuming a constant rainfall rate for the time period during which rainy weather was reported at the Fort McMurray Environment Canada weather station (www.ec.gc.ca), approximately 30 km south of the S^0 blocks (general weather description was not recorded for the Mildred Lake station).

Pore-water pressure response (Phase 1 block): The two-dimensional numerical model was used to model the rise and fall of the water table at the bottom of the Phase 1 block in response to a precipitation event on 14-15 April 2005 (36.3 mm over 25 hr). This event was modelled as it was a relatively intense and isolated rainfall event during which detailed pore-water pressure measurements were available.

A settlement profile (north/south orientation) of the bottom boundary of the Phase 1 block was estimated using the elevation of the S^0-liner interface at GTVP-03-07 (Figure 2.1) and the elevations of the S^0 block base at the north and south ends based on a topographic survey (data not presented). The domain for the unconfined flow model along the base of the Phase 1 block was 382 long and typically 2 m high. Vertical nodal spacing was 0.2 m in the top two-thirds of the mesh, and 0.05 m in the bottom third. Horizontal nodal spacing was 2 m throughout the mesh, except for the 2 m at the north end of the block (near drainage nodes) where the element size was reduced to 0.2 m. Outflow from the mesh occurred at nodes at the bottom of the north end of the block that were set at zero pressure head, and the bottom third of the vertical face of the north edge of the domain which was set as a potential seepage face. Fully drained conditions were

used for initial moisture contents. The total number of timesteps ranged from 200 to 300, with the total elapsed time ranging from 10 to 30 days depending on S_y and K values. Timesteps during the period of time in which water influx was applied to the top boundary were more detailed to ensure the input water volume was accurate.

Drainage rate response (Phase 2 block): Drainage rates from the base (north end) of the Phase 2 block in response to a precipitation event on 10-11 July 2006 (65.1 mm over 24 hr) were modelled using the same approach described above for the Phase 1 block. The precipitation event modelled for the Phase 2 block was chosen because it was also an intense and isolated rainfall event that caused a distinct increase in drainage rates. The model domain for the Phase 2 block was 273 m long, the length of the block in a north-south direction. Elevations of the base of the Phase 2 block at the north and south ends were obtained from a topographic map, and the settlement profile of the bottom of the Phase 2 block was assumed to have a similar shape as the Phase 1 profile.

2.5 Results and discussion

2.5.1 Water repellency

The wettability of the fracture faces varied from wettable (non-water repellent) to extremely water repellent (Table 2.4). This variation in water repellency was evident at small scales on fracture face areas of 10 cm^2, as well as across the entire depth profile. Both vertical and horizontal fracture faces were observed to be wettable. In contrast, clean, intact matrix material was observed to exhibit only extreme water repellency. In keeping with the wettability tests, static drop measurements indicated water contact angles on fracture faces where bacteria were determined to be present were 20 ± 5° whereas the sterile matrix S^0 had contact angles of 110 ± 10°. This indicates that the presence of microorganisms changes the S^0 surface from extremely hydrophobic to hydrophilic which is a critical step for microbial colonization and growth on S^0. Knickerbocker et al. (2000) observed that colloidal elemental S^0 floated on water for greater than three months yet sank after approximately two weeks if inoculated with *Thiobacillus thiooxidans*. They attributed the wettability of the inoculated S^0 to outer membrane vesicles, or blebs, of the *T. thiooxidans*. The hydrophilic blebs attach to the surface of the S^0 and overcome the hydrophobic barrier between the S^0 and the water.

Table 2.4. Water repellency classification for S^0 samples collected from Phase 1 depth profiles.

Cross-section	Fracture Orientation	Depth (cm)	Water repellency classification
A	Horizontal	0	Wettable
A	Vertical	5 to 8	Extremely repellent
A	Vertical	8 to 13	Extremely repellent
A	Vertical	13 to 22	Wettable
A	Horizontal	22	Wettable
A	Vertical	22 to 30	Slightly repellent.
A	Vertical	22 to 30	Strongly repellent
A	Vertical	30 to 35	Wettable
A	Horizontal	35	Wettable to extremely repellent
A	Vertical	43 to 46	Extremely repellent
A	Horizontal	46	Extremely repellent
A	Horizontal	51	Extremely repellent
B	Horizontal	0	Wettable
B	Vertical	0 to 5	Strongly repellent
B	Vertical	5 to 8	Slightly repellent
B	Horizontal	8	Extremely repellent
B	Horizontal	20	Extremely repellent
B	Horizontal	30	Extremely repellent
B	Horizontal*	33	Wettable
B	Horizontal	33	Wettable
B	Horizontal	49	Strongly to extremely repellent
C	Vertical	0 to 4	Wettable to extremely repellent
C	Vertical	4 to 11	Strongly to extremely repellent
C	Vertical	11 to 17	Wettable
C	Vertical	17 to 26	Wettable to extremely repellent

*Horizontal fracture face was on the bottom of excavated piece from 30 to 33 cm.

Bacteria including *Acidithiobacilli* employ some mechanism of attack or mobilization during their oxidation of S^0, including solubilization of the S^0 by fat globules of the cell envelope (Vogel and Umbriet 1941) or solubilization by phospholipids (Pivovarova et al. 1982). Bryant et al. (1984) indicated bacterial attachment to S^0 occurs via a secreted exopolymer or glycocalyx. The oxidation of S^0 in the soil environment involves the development of a conditioning film associated with the colonization by microorganisms (Lawrence and Germida 1991). Consistent with these observations, the microscopic examination of aseptically obtained fractures incubated in filter sterilized S^0 block drainage water showed the presence of a patchy "biofilm" that consisted of bacteria and fungal cells as well as microbial exopolymers that bound a variety of lectins (Table 2.2). The lectin binding patterns illustrated the presence of a range of bacterial types and a complex exopolysaccharide matrix (Figure 2.3). No lectin

binding was detected on the aseptically stained matrix S^0 surfaces even after incubation in sterile filtered S^0 block drainage water. The surface film contained bacterial glycoproteins with associated mannose, glucose, galactose, and oligosaccharides (Table 2.2, Figure 2.3). In addition, chitin was detected consistent with the presence of fungal hyphae. Additional molecular studies confirmed the presence of *Acidithiobacillus* sp., Archaeal probe positive cells, β-proteobacteria, α- proteobacteria, and other acidophilic S^0 oxidizers (*Acidiphillium sp.*, *Leptospirillum* sp. and *Acidimicrobium* sp.) (J.R. Lawrence, M.J. Hendry, unpublished data). The presence of this bio-coating on fracture surfaces would result in a hydrophilic surface that would retain water at the surface of the S^0 and facilitate growth and oxidation of S^0 by the associated microorganisms.

Of the three sediment samples taken from the S^0 block surface, two were classified as slightly water repellent and one as extremely water repellent. The water repellency measured for these samples represents a maximum potential value, as water repellency of air-dried samples is known to be greater than for moist samples (Dekker and Ritsema 2000). Therefore, a reasonable assumption is that the two slightly water repellant samples may exhibit no water repellency in moist *in situ* conditions. The water repellency of the sediment samples was also increased by the presence of powdered S^0. Although care was taken during sample collection, S^0 concentrations were 27-50% by weight (data not presented). The cause for the extreme water repellency of the third sample is not known but may have been due to the presence of finely powdered S^0 in the sample.

Water drop penetration tests did not provide conclusive evidence that wind-blown sediments on fracture faces in the S^0 block provide a pathway for water infiltration. However, given that two of the three samples exhibited only slight water repellency despite being air-dried and containing >27% S^0, wind-blown sediments along fracture faces in the S^0 block may contribute to hydrophilic pathways for infiltrating water provided by microbial biofilms.

2.5.2 Dye tracer tests

Results of the dye tracer test (Figures 2.4 and 2.5) clearly show infiltrating water follows preferential flow paths through the S^0 block. Discrete vertical fractures were the points of infiltration at the surface of the block, with lateral and

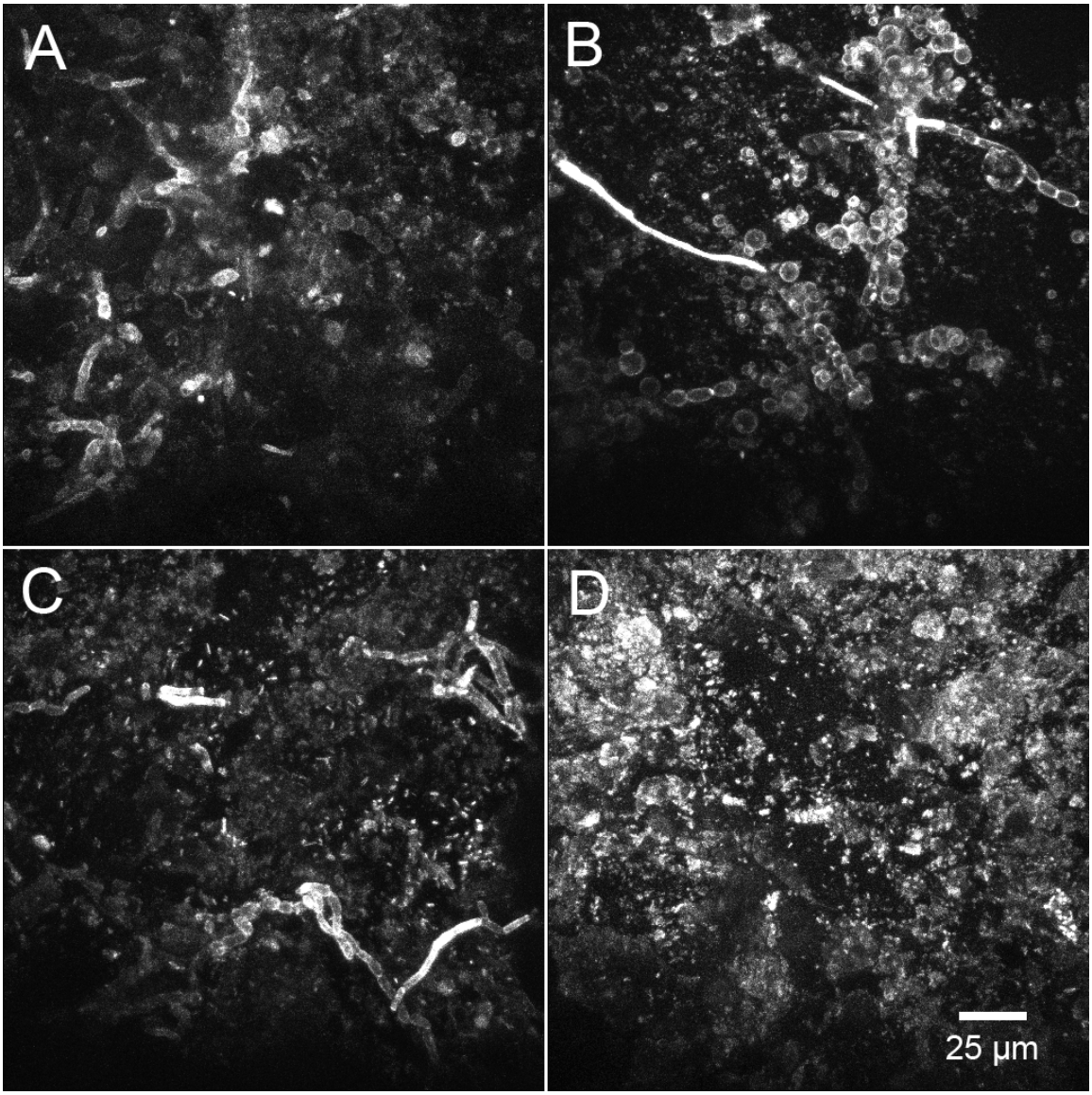

Figure 2.3. Confocal micrographs of fracture surfaces stained with lectins (A. *Triticum vulgaris*, B. *Galanthus nivalis*, C. *Solanum tuberosum*, and D. *Phaseolus coccineus*) with affinity for specific mono-oligosaccharides, fungal hyphae, bacterial cells, and generally distributed exopolymers.

downward migration of the tracer in the top 0.1-0.2 m occurring primarily through discrete horizontal and vertical fractures. Greater lateral dispersion of the dye tracer occurred at depths >0.2 m where the discrete fractures intersected areas with larger and friable crystal structures (Figure 2.5). The migration of the dye tracer along discrete fractures was relatively consistent between cross-sections for each test (Figure 2.5);

however, the migration of the tracer through areas with larger and more friable crystals was more variable.

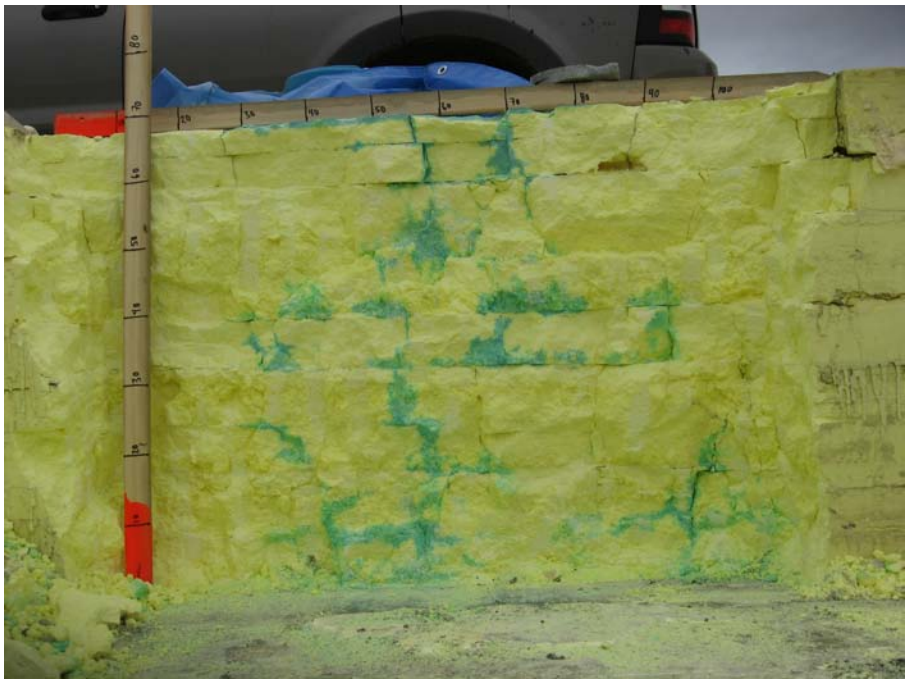

Figure 2.4. First vertical cross-section of S^0 block below area of dye tracer infiltration (Test 1).

Because the spreading of the dye tracer into the S^0 matrix was greater than for pure water (contact angle between dye tracer and S^0 was $<90^o$), actual water infiltration would follow more distinct preferential pathways than those exhibited in Figures 2.4 and 2.5. However, the greater spreading into the matrix material improved the visibility of the dye tracer while still demonstrating preferential flow through the block.

For some horizontal fractures, the dye was present and dispersed above the fracture but not below. This was attributed to the presence of larger S^0 crystals and greater porosity above the fracture. Each horizontal fracture corresponded to an interface between S^0 lifts, and solidification of molten S^0 would have been slowest at the bottom of each lift, resulting in larger crystals.

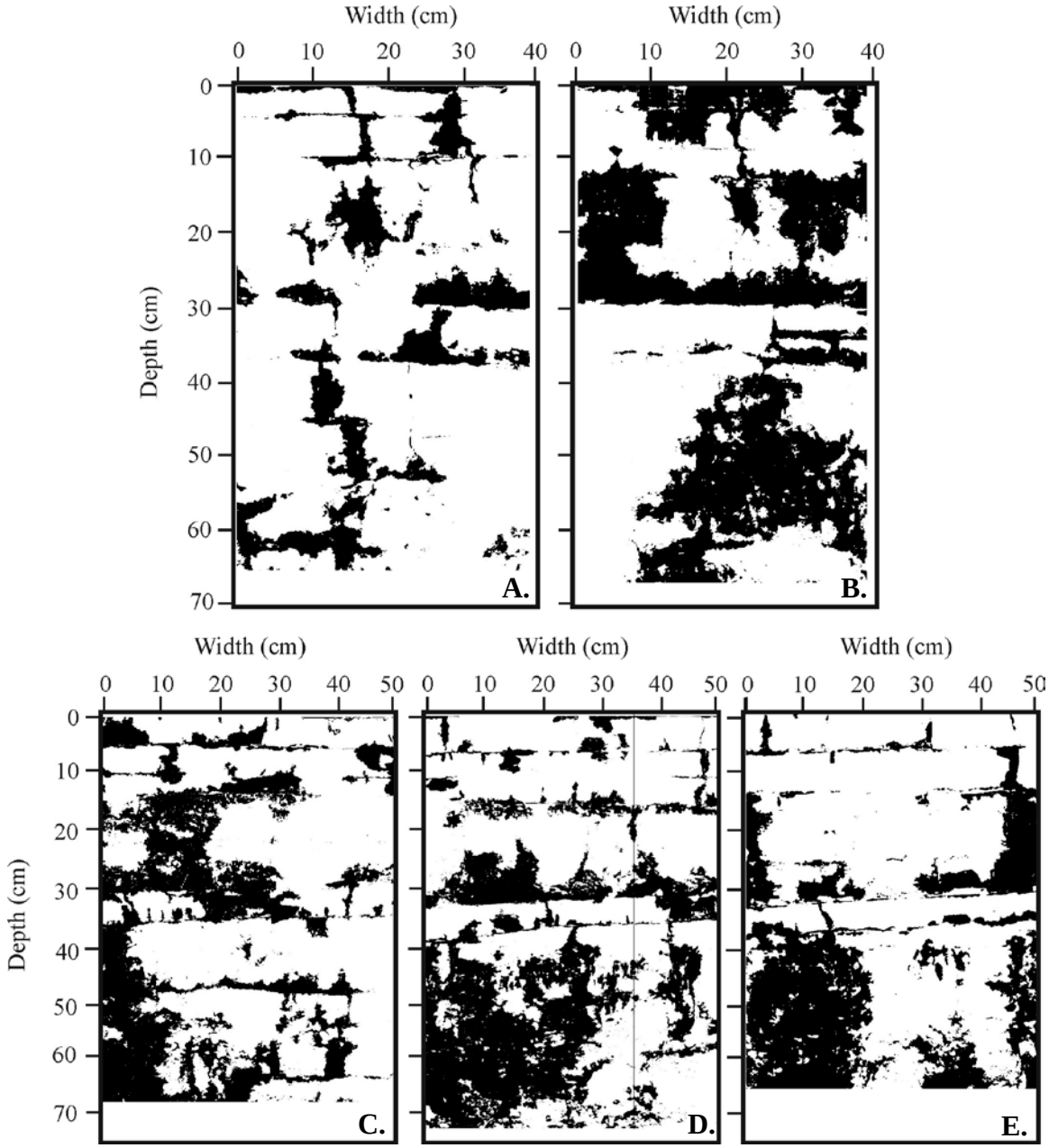

Figure 2.5. Distribution of dyed area across vertical tracer test cross-sections below Test 1 (A: north edge of form, and B: 0.2 m from north edge of form) and Test 2 (C: north edge of form, D: 0.2 m from north edge of form, and E: 0.4 m from north edge of form).

2.5.3 Water mass balance

Precipitation and evaporation comparison: Actual evaporation and rainfall precipitation were recorded for the entire 135-day test period (4 May to 16 September

2005; Figure 2.6). The actual evaporation (27.4 mm; average rate 0.20 mm/d) was 9.4% of the cumulative precipitation (292.1 mm) and 8.6% of potential evaporation (average rate 2.4 mm/d). The actual evaporation from the S^0 block was very low compared to literature values. For example, Carey et al. (2005) reported an evaporation-rainfall ratio of 61.4 % for an unvegetated waste-rock pile in northern Saskatchewan (57^o 12' N, 105^o 35' W). At an adjacent reclamation site with vegetation, May to August evaporation values exceeded rainfall values by 24 to 70% over a number of monitored years, drawing water stored in the vadose zone to sustain rates of approximately 2 mm/d (Carey 2008). The low actual evaporation from the S^0 block indicates that most of the precipitation (>90%) falling on the S^0 block infiltrates through the block and is not accessible for evaporation near the block surface.

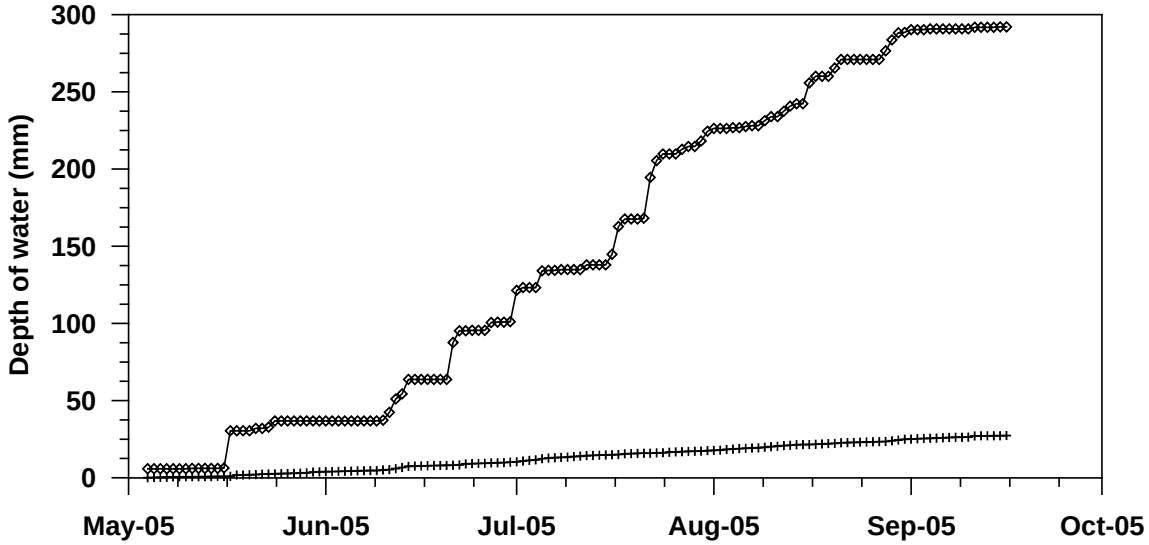

Figure 2.6. Cumulative precipitation (diamond symbols) and actual evaporation (cross symbols) for the Phase 1 S^0 block.

A key reason for the low evaporation rates is the high albedo (ratio between reflected and incoming solar radiation) of the S^0 blocks, which averaged 0.71. The S^0 albedo was at the high end of literature values and similar to snow-covered grasslands, lakes, and wetlands (Baldocchi et al. 2000). Evaporation occurred at a relatively steady rate (0.20 mm/d), suggesting infiltration after rainfall events is rapid (discussed below) and that the evaporative flux from the surface of the S^0 block results from a diffusive

flux of water vapour from the block to the atmosphere, rather than from evaporation from ponded or stored water.

Precipitation and drainage comparison: The cumulative evaporation volume from the Phase 2 block (Figure 2.7) was estimated assuming that evaporation rates were constant and similar to the measured values for the Phase 1 block (0.20 mm/day). The cumulative volume of drainage plus evaporation agreed with the cumulative precipitation volume throughout the field season. At the end of the field season, the drainage plus evaporation volume was only 5.1% less than the cumulative precipitation volume. Cumulative drainage volumes that exceeded precipitation volumes in late March and early May were attributed to rain from March 15-24 (cumulative depth 48 mm) contributing to the cumulative drainage volumes after 25 March 2005.

A similar comparison for the Phase 1 block is not presented because the contributing area to seepage from the north end of the Phase 1 block was greater than the footprint area of the block. As a result, the cumulative Phase 1 drainage volumes were at least double the rainfall volumes (based on footprint area of Phase 1 block; data not presented). This additional flow was attributed to groundwater discharge beneath the Phase 1 block from adjacent uplands. The drainage rates from the Phase 2 block were closely correlated with the rainfall rates. A more detailed discussion of the timing of drainage rates in response to rainfall events is presented in the modelling section below.

Water storage: The moisture contents measured in the Phase 1 block (Figure 2.8) ranged from 0.014 to 4.2 vol.% (θ_w) (0.001 to 2.3 gravimetric %) with a mean value of 0.6 vol. % (n = 108, s.d. = 0.7 vol. %). In general terms, the S^0 was very dry with a moisture content similar to that of a sand dune in an arid environment (Severinghaus et al., 1996). As discussed above, water flow and storage within the S^0 block are likely limited to the hydrophilic regions of fracture faces and more friable areas. This assumption is reasonable given the mean θ_w (0.6 %) was 41% (n = 108, s.d. = 50%) of the estimated n_f (1.4%). The most recent rainfall event prior to sample collection on 25-27 April 2006 was 2.5 mm from 05:00-08:00 on 22 April. The impact of this 2.5 mm rainfall event on the moisture contents measured on April 25-27 was analyzed using the one-dimensional analytical solution described above (Lessoff and Indelman 2004),

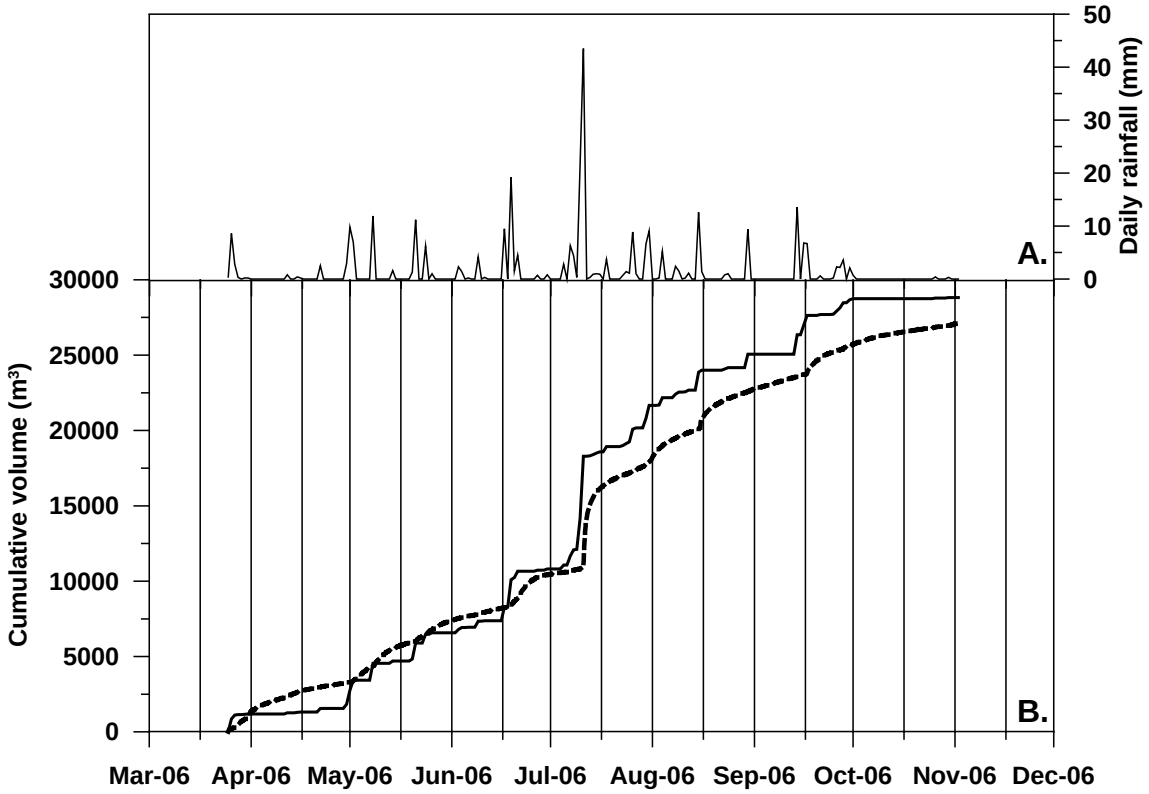

Figure 2.7. Daily precipitation (A.), and cumulative volumes of precipitation (solid line) and drainage plus evaporation (dashed line) (B.) for the Phase 2 S^0 block in 2006. Daily precipitation depths are presented above the cumulative volume graphs and correspond to the y-axis on the right.

assuming an n of 4%, θ_r of 0.6%, K_s of 1×10^{-2} m/s, and Brooks-Corey parameter of 0.33 for Eq[2.3]. Simulated θ_w depth profiles 3-5 days after the rainfall increased to a maximum of only 0.62% (initially 0.6%), suggesting the 22 April rainfall had very little effect on the θ_w of samples collected from 25-27 April. This indicates the mean measured θ_w is likely a reasonable estimate of θ_w for fully drained conditions, analogous to residual moisture content (θ_r, used to calculate S in Eq[2.3]) for a typical hydrophilic soil.

Measured θ_w showed no significant trend with depth. Although the greatest moisture contents were measured from 0-3 m depths, mean moisture contents at these shallow depths are not statistically different from the overall mean moisture content using a z-test with a 95% confidence level.

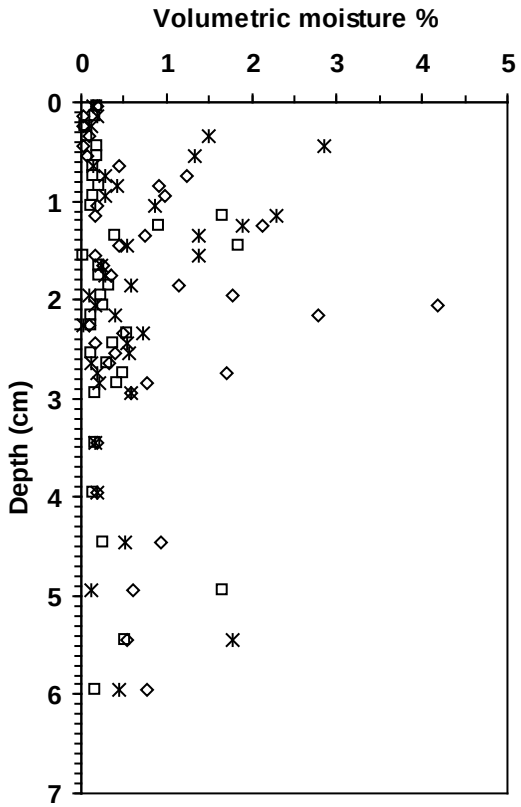

Figure 2.8. Moisture content depth profiles for SRD06-143 (diamond symbols), 144 (box symbols), and 145 (star symbols).

The elevation of the water table (Figure 2.9) ranged from 0.45 to 1.70 m above the base of the S^0 block (base elevation 303 m asl at the monitoring point), with fluctuations corresponding to rainfall events. During winter months and dry periods, the water table was approximately 0.6-0.8 m (303.6-303.8 m asl) above the block base, approximately level with the base of the north end of the Phase 1 block (303.7 m asl) where the majority of drainage occurred. This suggests most of the S^0 block depth is typically unsaturated, with the exception of an approximately 1 m zone near the base where saturation levels fluctuate from temporary water ponding after rainfall events. Due to differential settlement of the S^0 block (i.e., development of a settlement profile with the greatest settlement in the middle of the block), a small depth interval at the bottom of the interior of the S^0 block (maximum thickness of 0.8 m) is likely fully saturated year-round.

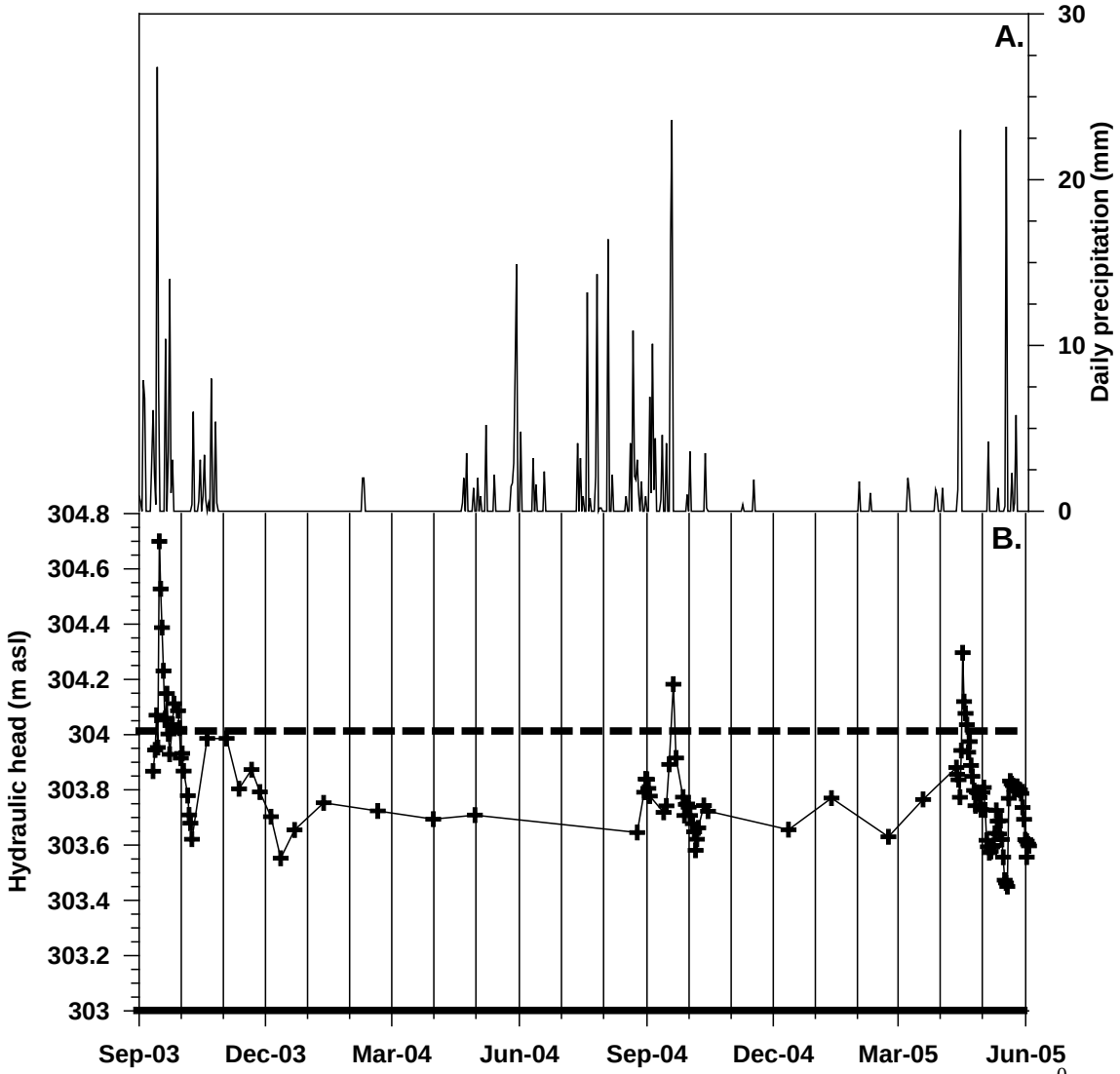

Figure 2.9. Daily precipitation (A.), and hydraulic head at the base of the Phase 1 S^0 block at GTVP03-07 (B.). The dotted line in B. represents the elevation of the vibrating wire piezometer tip and the solid line represents the base of the Phase 1 S^0 block at GTVP03-07 (piezometer tip installed at 304.1 m asl).

The water table at the base of the Phase 1 block was frequently below the piezometer tip (304.1 m asl). The vibrating wire piezometer is capable of measuring negative porewater pressures if the piezometer tip remains saturated (manufacturer specifications). Given the piezometer was backfilled with a cement-bentonite grout, the tip likely did remain saturated and the negative pore-water pressure measurements were accurate.

Modelling of pore-water head and outflow rate responses: The measured and modelled total head at the base of the Phase 1 block in response to rainfall on 14-15

April 2005 (36.3 mm over 25 hr) are presented in Figures 2.10B and C with rainfall amounts, rainfall intensity, and two different simulations of water flux (q) calculated from the one-dimensional analytical solution presented in Figure 2.10A. As described above, transient recharge (q) functions were applied to the top boundary of the two-dimensional numerical model for simulating the rise and fall of the water table at the base of the Phase 1 block.

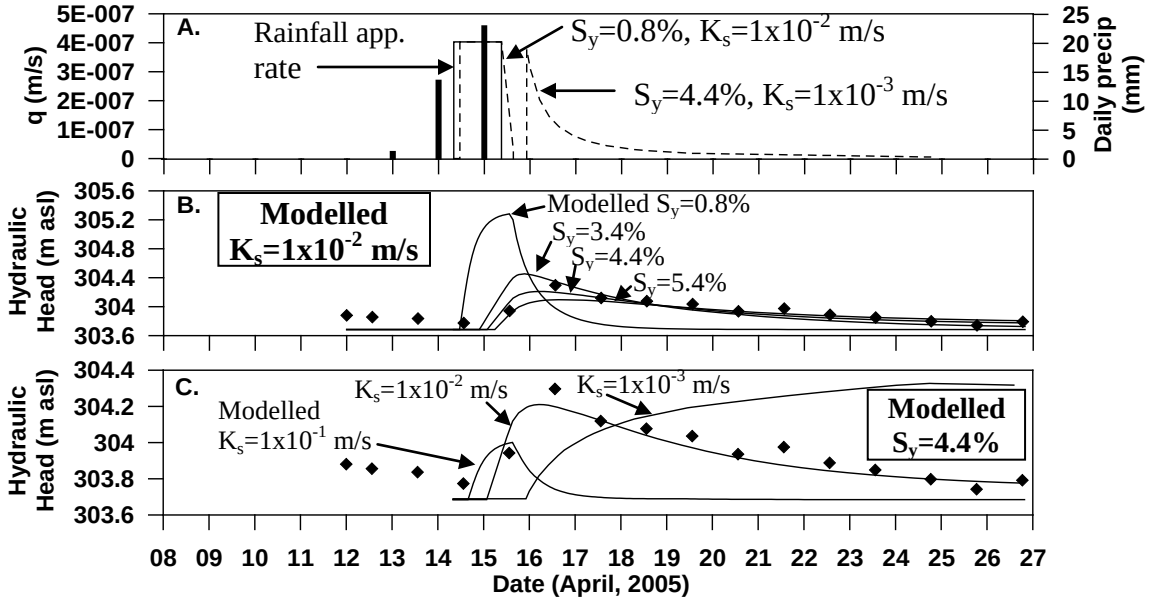

Figure 2.10. One-dimensional water flux (q) calculations and rainfall intensities (A) and two-dimensional hydraulic head response modelling (B, C) for a 14-15 April 2005, rainfall event. In A, vertical bars represent daily rainfall intensity, solid lines represent rainfall application rate to the top boundary of the 1-D analytic solution, and dashed lines represent examples of calculated water flux (q) from the bottom boundary of the 1-D solution (input influx to top boundary of 2-D numerical model). In B and C, measured hydraulic head values are represented by solid diamond symbols and solid lines represent modelled hydraulic head responses.

As expected, the water arrival to the bottom boundary of the analytical solution was delayed with decreasing K_s and increasing S_y values. For the S_y and K_s values used, the peak q values from the bottom boundary were equal to or slightly less than the rainfall application rate (4×10^{-7} m/s). S_y and K_s values of 4.4% and 1×10^{-2} m/s, respectively, resulted in the best match between measured and modelled hydraulic head responses. Decreasing the S_y for a given K_s resulted in a faster hydraulic response and increased peak hydraulic head values (Figure 2.10B). Decreasing the K_s for a given S_y resulted in a slower hydraulic response (Figure 2.10C) and, for the S_y and K_s values

used in this study, increased peak hydraulic head values. However, for any S_y value and rainfall event, the peak hydraulic head would not continually increase with decreasing K_s (a maximum possible hydraulic head would exist).

Measured and modelled outflow response from the Phase 2 block for rainfall on 10-11 July 2006 are presented in Figures 2.11B, C and D with rainfall amounts, rainfall intensity, and two simulated q functions from the one-dimensional analytical solution presented in Figure 2.11A. Similar to modelled hydraulic head responses (Figure 2.10B and C), the outflow response was delayed with increasing S_y (Figure 2.11B) and decreasing K_s (Figures 2.11C and D). Modelled cumulative outflow volumes for S_y = 0.8% and $K_s = 1 \times 10^{-2}$ m/s, and S_y = 3.4% and $K_s = 1 \times 10^{-1}$ m/s (Figures 2.11C and D, respectively) matched measured outflow volumes relatively well early in the outflow response, but were greater than measured values at later times. Matches between modelled and measured outflow volumes at later times were improved for simulations with S_y = 0.8% and $K_s = 1 \times 10^{-3}$ m/s, and S_y = 3.4% and $K_s = 1 \times 10^{-2}$ m/s (Figures 2.11C and D, respectively), however these modelled outflow volumes were less than measured volumes for early times.

A reasonable match between modelled and measured outflow volumes for both early and late times was achieved by applying a greater S_y (4.4%) in the middle 130 m of the block, and a lower S_y (0.8%) in the outer regions (~70 m) ($K_s = 1 \times 10^{-2}$ m/s) (Figure 2.11B). The rationale for applying a greater S_y in the middle of the block was that water ponding in response to rainfall was greatest in this region (due to the concave up settlement profile, data not presented). This water ponding would create positive porewater pressure heads and force water into the hydrophobic n_m, increasing the S_y. Bonstrom (2007) determined that porewater pressure heads of 1-2.5 m increased the water storage in matrix S^0 (S_y) by ~1-3 vol. %. Simulated porewater pressure heads of 1-2.5 m developed in the middle of the block in response to the 10-11 July 2006 rainfall, therefore a greater S_y would be expected in this region. A S_y of 4.4 % also corresponded with the best-fit S_y for the hydraulic head response modelling which was compared with field piezometer data measured in the middle region of the Phase 1 block. Modelled

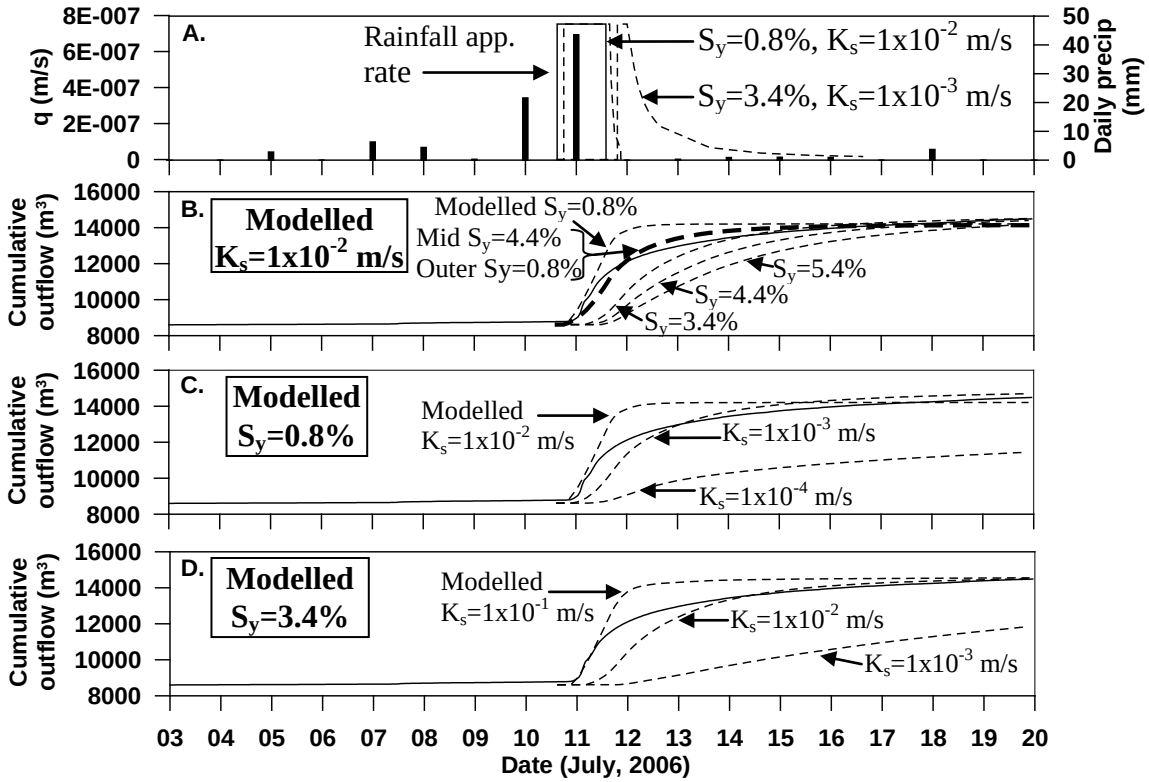

Figure 2.11. One-dimensional water flux (q) calculations and rainfall intensities (A) and two-dimensional outflow response modelling (B, C) for a 10-11 July 2006 rainfall event. In A, vertical bars represent daily rainfall intensity, the solid line represents rainfall application rate to the top boundary of the 1-D analytic solution, and dashed lines represent examples of calculated water flux (q) from the bottom boundary of the 1-D solution (input influx to top boundary of 2-D numerical model). The solid lines in B, C, and D represent measured cumulative outflow volumes and dashed lines represent modelled outflow response. The bold dashed line in B represents modelled outflow response for K_s=1 × 10^{-2} m/s and S_y=4.4% in the middle 130 m and S_y=0.8% in the outer regions.

hydraulic head response in the Phase 1 block assuming spatial variation of S_y similar to the conditions described matched measured values reasonably well (data not presented).

Considering both the hydraulic head and outflow modelling, the best estimate for S_y of the S^0 blocks was ~0.8% in regions where hydraulic pressure head was <1 m, and as great as 4.4% where hydraulic pressure head was as great as 2.5 m. The best estimate of K_s was 1 × 10^{-2} ± 5 × 10^{-3} m/s. The modelling suggested water flow and storage occurs through the fracture porosity (1.4%, equal to an S_y of 0.8% assuming a resident moisture content of 0.6%), and in the matrix porosity (as much as 3.6%, corresponding to an S_y of 4.4%) in regions where hydraulic pressure heads exceed 1 m. The portion of

the matrix porosity through which water flow occurred was likely associated with the friable S^0 zones observed to facilitate preferential water flow in the dye tracer test.

The K_s estimates from modelling in this study ($1 \times 10^{-2} \pm 5 \times 10^{-3}$ m/s) were similar to theoretical K_s for S^0 blocks calculated by Bonstrom et al. (2009) (6.1×10^{-3} m/s) based on fracture flow theory, but were more than two orders of magnitude greater than estimates from modelling of hydraulic packer tests performed in the Phase 1 block (1×10^{-5} to 1×10^{-6} m/s for depths greater than 9 m; Bonstrom 2007). The lower K_s estimates from the packer testing were attributed to clogging of fractures with S^0 powder during drilling of the boreholes for the packer tests. Modelling of the packer tests (not presented) showed a low-K_s layer (K_s equal to matrix K_s of 1.7×10^{-6} m/s; Bonstrom 2007) as thin as 0.1-0.2 m around the borehole would have affected the apparent K_s estimated by the packer test modelling.

2.6 Conclusions

Water storage and flow in S^0 blocks occurs preferentially in discrete fractures and friable zones of the matrix porosity (less than 3.6 vol.%). Because S^0 oxidation requires the presence of liquid water (Birkham et al. 2010), H_2SO_4 production would be limited to these regions. Greater than 90% of rainfall on the S^0 blocks infiltrates along preferential flowpaths through the blocks, due in part to the relatively high bulk K_s ($1 \times 10^{-2} \pm 5 \times 10^{-3}$ m/s) of the blocks. A key implication of this study is that although clean S^0 is extremely hydrophobic and above-ground blocks may intuitively appear to be very resistant to water infiltration, water rapidly infiltrates and is readily available for H_2SO_4 production within the blocks along hydrophilic pathways created by microbial colonization.

Representing S^0 blocks as a hydrophilic equivalent porous medium with a porosity equal to, or slightly greater than, the fracture porosity (1.4-5 vol.%) appears to be a reasonable assumption for basic modelling of water flow in unsaturated conditions. These results should be applicable to commercial-scale S^0 blocks worldwide given that construction methods are similar within the industry. The S_y estimates (0.8 to 4.4%) presented in this study are applicable to S^0 blocks in which hydraulic pressure heads are $\leq$2.5 m. S_y could increase to $\geq$6.9 % (sum of interconnected n_m and n_f) if hydraulic

pressure heads exceed 2.5 m, as water will begin to enter more of the matrix porosity at greater pore-water pressure heads.

Based on S^0 oxidation rate estimates by Birkham et al. (2010) (1.8 mol $O_2/m^3/d$ in the upper 1 m, and 2.7 x 10^{-4} mol $O_2/m^3/d$ below 1 m) and the stoichiometry in Eq.[2.1], annual water consumption in the Phase 1 block per m^2 was estimated at 2.6 L (depth of 2.6 mm), with 70 to >97 % of the annual water demand occurring in the upper 1 m during the summer. This was only 0.6% of the mean annual precipitation (water equivalent of 455.5 mm; Environment Canada online data from 1971-2000, www.ec.gc.ca), suggesting that cover systems designed to minimize water infiltration, and thereby minimize H_2SO_4 production in S^0 blocks, would need to be much more effective (efficiency >99.4%) than current conventional cover designs for mine closure (typical efficiency ~95%; M. O'Kane, personal communications) to decrease S^0 oxidation rates.

If a cover was installed on the block that eliminated infiltration, the stored water in the upper 1 m (estimated resident concentration of 0.6%) could maintain S^0 oxidation rates (as described above) for approximately 2 years. Assuming the zone of high S^0 oxidation rates moved deeper in the block as water was depleted in the upper 1 m, S^0 oxidation could continue for ≥40 years using resident water stored in the block. Therefore, installation of a cover system on a S^0 block that has been exposed to the environment might effectively eliminate the generation of acidic effluent but H_2SO_4 production within the block could be expected to continue for several years.

2.7 Acknowledgments

Robert Mahood and Gord McKenna provided field support, and Julie Robertson, Rob Holben, Matt Harker, and Greg Newman (Geo-Slope International Ltd.) technical assistance. We acknowledge the funding provided the Natural Science and Engineering Research Council of Canada and Syncrude Canada Ltd.

2.8 References

Baldocchi D, FM Kelliher, TA Black, and P Jarvis. 2000. Climate and vegetation controls on boreal zone energy exchange. Global Change Biology, 6(Suppl. 1): 69-83.

Bear J. 1972. Dynamics of fluids in porous media. Dover Publications, Mineola, N.Y.

Birkham TK, MJ Hendry, and SL Barbour. 2010. Controls and rates of acid production in commercial-scale sulphur blocks. In Press to Journal of Environmental Quality.

Bonstrom K, SL Barbour, and MJ Hendry. 2009. Physical and hydraulic characterization of fractured, hydrophobic, sulphur within above ground sulphur blocks. Under revision, Canadian Geotechnical Journal.

Bonstrom K. 2007. Physical controls on water migration in elemental sulphur blocks. M.Sc. thesis, Department of Geological Sciences, the University of Saskatchewan, Saskatoon, SK.

Brooks RH and AT Corey. 1964. Hydraulic properties of porous media. Hydrology Paper 3, Colorado State University, Fort Collins, CO.

Bryant RD, JW Costerton, and EJ Laishley. 1984. The role of *Thiobacillus albertis* glycocalyx in the adhesion of cells to elemental sulfur. Canadian Journal of Microbiology, 30: 81-90.

Carey SK, SL Barbour, and MJ Hendry. 2005. Evaporation from a waste-rock surface, Key Lake, Saskatchewan. Canadian Geotechnical Journal, 42(4): 1189-1199.

Carey SK 2008. Growing season energy and water exchange from an oil sands overburden reclamation soil cover, Fort McMurray, Alberta, Canada. Hydrological Processes, 22: 2847-2857.

Cey E, D Rudolph, and R Therrien. 2006. Simulation of groundwater recharge dynamics in partially saturated soils incorporating spatially variable fracture apertures. Water Resources Research, 42: W09413. doi:10.1029/2005WR004589.

Dekker LW, and CJ Ritsema. 2000. Wetting patterns and moisture variability in water repellent Dutch soils. Journal of Hydrology, 231-232: 148-164.

DiCarlo DA. 2003. Drainage in finite-sized unsaturated zones. Advances in Water Resources, 26: 1257-1266.

Energy Resources Conservation Board (ERCB). 2008. Alberta's energy reserves 2007 and supply/demand outlook 2008-2017. ST98-2008, Calgary, AB.

Flury M and H Fluhler. 1994. Brilliant Blue FCF as a dye tracer for solute transport studies-a toxicological overview. Journal of Environmental Quality 23: 1108-1112.

Fredlund DG and H Rahardjo. 1993. Soil mechanics for unsaturated soils. John Wiley & Sons Inc., Toronto, ON.

Guarracino L. 2006. A fractal constitutive model for unsaturated flow in fractured hard rocks. Journal of Hydrology, 324: 154-162.

Janzen HH and JR Bettany. 1987. Measurement of sulfur oxidation in soils. Soil Science, 143(6): 444-452.

Knickerbocker C, DK Nordstrom, and G Southam. 2000. The role of "blebbing" in overcoming the hydrophobic barrier during biooxidation of elemental sulphur by Thiobacilllus thiooxidans. Chemical Geology, 169: 425-433.

Kosich D. 2008. Sulphur, potash prices soar last month as base and precious metals decline. International Business Times, June 20.

Lawrence JR and JJ Germida. 1991. Microbial and chemical characteristics of elemental sulfur beads in agricultural soils. Soil Biology and Biochemistry 7: 617-622.

Lessoff SC and P Indelman. 2004. Analytical model of solute transport by unsteady unsaturated gravitational infiltration. Journal of Contaminant Hydrology, 72: 85-107.

Lipsius K and SJ Mooney. 2006. Using image analysis of tracer staining to examine the infiltration patterns in a water repellent contaminated sandy soil. Geoderma, 136: 865-875.

Lyklema J. 1995. Fundamentals of interface and colloid science. Academic Press, New York, N.Y.

McElroy DL and JM Hubbell. 2004. Evaluation of the conceptual flow model for a deep vadose zone system using advanced tensiometers. Vadose Zone Journal, 3: 170-182.

Meyer B. 1977. Sulphur, energy and environment. Elsevier Scientific, Amsterdam, Netherlands.

Neu TR, GDW Swerhone, and JR Lawrence. 2001. Assessment of lectin-binding-analysis for in situ detection of glycoconjugates in biofilm systems. Microbiology, 147: 299-313.

Ober JA. 2002. Materials flow of sulfur. U.S. Geological Survey. Open-file report 02-298.

Ober JA. 2008. U.S. Geological Survey, Mineral Commodity Survey, January, 164-165.

Pivovarova TA, YM Miller, SA Krasheninnkova, OA Kapustin, and SI Karavaiko. 1982. The role of phospholipids in the fractionation of stable isotopes of sulfur in its oxidation by *Thiobacillus ferrooxidans*. Mikrobiologiya, 51: 522-556.

Postgate J. 2000. Microbes and Man. Cambridge University Press, Cambridge, UK.

Proce B. 2006. Growing issue: Oilsands mining companies are looking for ways to manage growing levels of sulphur production from landlocked Athabasca oilsands region. Oilsands Review, October.

Pullan AJ. 1990. The quasilinear approximation for unsaturated porous media flow. Water Resources Research, 26(6): 1219-1234.

Severinghaus JP, ML Bender, RF Keeling, and WS Broecker. 1996. Fractionation of soil gases by diffusion of water vapor, gravitational settling, and thermal diffusion. Geochimica et Cosmochimica Acta, 60(6): 1005-1018.

Sklodowska A, M Wozniak, and R Matlakowska. 1999. The method of contact angle measurements and estimation of work of adhesion in bioleaching of metals. Biological Procedures Online, 1: 114-121.

Syncrude Canada Ltd. 2004a. Geo-environmental observations of 17 sulphur blocks in Alberta. Research Dept. Progress Report 33(2), Fort McMurray, AB.

Syncrude Canada Ltd. 2004b. Geochemical characterization of a large sulphur block at Syncrude: Results from the 2003 field investigation. June 21, 2004, Fort McMurray. AB.

Vogel KG and WW Umbriet. 1941. The necessity for direct contact in sulfur oxidation by *Thiobacillus thiooxidans*. Soil Science, 51: 331-337.

3.0 ADVECTIVE AND DIFFUSIVE GAS TRANSPORT THROUGH FRACTURED SULPHUR BLOCKS

Preface

Molecular O_2 is the key electron acceptor during microbial oxidation of S^0 to SO_4 (i.e. H_2SO_4) and, as such, is a fundamental control on acid production rates in S^0 blocks. As O_2 in oxidizing S^0 blocks is continually being consumed, an influx of atmospheric O_2 is required to replenish subsurface O_2 concentrations for acid production to persist. This manuscript investigates the key transport mechanisms by which atmospheric O_2 migrates into S^0 blocks. Diffusion of O_2 through unfractured matrix S^0 is measured in laboratory diffusion cells, while diffusion through a fractured S^0 block is measured by an *in situ* gas tracer experiment. *In situ* distributions of N_2, O_2, and CO_2 are measured and modelled to estimate the relative contributions of advective and diffusive O_2 transport.

Reference: Birkham TK, MJ Hendry, and SL Barbour. Advective and diffusive gas transport through fractured sulphur blocks. In press to Vadose Zone Journal, 2010.

3.1 Abstract

Long-term storage of sulphur (S^0) blocks poses a contamination risk to both groundwaters and surface waters as the oxidation of S^0 to H_2SO_4 creates drainage waters with low pH and elevated SO_4 concentrations. Because the presence of oxygen (O_2) in the S^0 blocks is a primary control on S^0 oxidation, rates of atmospheric gas migration into the blocks can be used to quantify S^0 oxidation rates. Using *in situ* measurements and a tracer experiment combined with laboratory diffusion experiments, a transport analysis of multiple gas species is used to quantify O_2 fluxes into a S^0 block. Advection, created by O_2 consumption within the block, accounted for 20% of the total O_2 influx and considerably increased H_2SO_4 production in the block above that attributed to O_2 diffusion. While barometric pumping was likely influencing O_2 concentrations in the upper 8 m, its overall effect on O_2 influx was determined to be negligible. Quantification of O_2 and CO_2 fluxes was necessary to explain the direction and magnitude of N_2 concentration gradients that develop in the block, despite the fact that N_2 was non-reactive. Our findings should be widely applicable because the construction method of S^0 blocks is standard throughout the world.

3.2 Introduction

S^0 production has increased over the past 20 years concurrent with the removal of SO_2 and H_2S at petroleum refineries, natural gas plants, coking plants, and non-ferrous metal smelters. Mining now accounts for <10% of global S^0 production (Ober, 2007). The resulting surplus of S^0 has been accompanied by a drastic decrease in its price. From 1982 to 2002, the price dropped from $300 to ~$25 USD per t (Ober, 2002). S^0-producers in western Canada, the Middle East, and the Caspian Sea region, where transportation costs are relatively high, have therefore stockpiled large volumes of S^0 (Proce, 2006). From 2005-2008, global S^0 supply and demand was relatively balanced (ERCB, 2008) and prices increased to $700 USD per t (Kosich, 2008). During this period S^0 was mined from the most accessible S^0 stockpiles; however, a S^0 surplus and continued stockpiling is expected from 2011-2017 (ERCB, 2008). In Canada, the world's largest S^0-producer, 11.6 Mt of S^0 was stockpiled as of April 2008 (ERCB, 2008). Annual S^0 production from bitumen upgrading at Canadian oilsands mining operations

in northeastern Alberta, Canada, was 1.5 Mt in 2007 and is expected to increase to 5.3 Mt by 2017 (ERCB, 2008).

The current practice of storing S^0 is to pour molten S^0 (135 to 145°C) in a confined area on the ground surface in lifts of about 0.1 m. The molten S^0 in these lifts solidifies (at 115°C), and as subsequent lifts of S^0 are poured, a large S^0 block is constructed (typically ~100 m × 200 m × 10-20 m high). Most sites with S^0 blocks older than 20 years experience problems with groundwater contamination as a result of the release of H_2SO_4 derived from S^0 oxidation (Syncrude Canada Ltd., 2004a). Drainage waters seeping from the base of these S^0 blocks typically have low pH (0.4-1.0) and high SO_4 concentrations (12-34 g/L) (unpublished data), and soil and groundwater acidification and soil salinization occurs adjacent to the blocks.

Although S^0 oxidation has been studied in soil fertilization (Janzen and Bettany, 1987a, b), bioleaching (Salo-Zieman et al., 2006), composting (Beffa et al., 1996), and natural environments (Knickerbocker et al., 2000), the S^0 under investigation has typically been in a fine, particulate form (<1 mm diameter). The limited number of published studies on the oxidation of S^0 in large blocks may be the result of the relatively recent concern over their environmental impact. Moreover, investigations of this phenomenon are complex as the S^0 blocks are unsaturated, fractured, and hydrophobic, although hydrophilic conditions may develop on fracture faces in the presence of hydrophilic bacterial growth or wind-blown sediments (Birkham et al., 2009).

Molten S^0 shrinks by 7% during the phase change from molten to solid S^0, and by an additional 5.5% during the mineral change from monoclinic to rhombic crystal structure (Meyer, 1977). The solidification of S^0 lifts occurs within 1 d of pouring, while the mineral change occurs over several days at temperatures <95°C. These volume changes result in extensive vertical and horizontal fracturing of the S^0 blocks (Syncrude Canada Ltd., 2004b; Bonstrom, 2007). The mean matrix porosity (n_m) of S^0 core samples is 9.4% (n=280, s.d.=3.5%) with values ranging from 4.5-23%. The wide range in values was attributed to variable rates of cooling (Bonstrom, 2007). Birkham et al. (2009) measured a mean volumetric moisture content of 0.6% (θ_w) in one block.

The rate of S^0 oxidation to SO_4 (i.e., production of H_2SO_4) is controlled by the activity of S^0-oxidizing microorganisms (Janzen and Bettany, 1987a) that may be either heterotrophic or autotrophic (Lawrence and Germida, 1991). Heterotrophic organisms require molecular O_2 as an electron acceptor and produce CO_2; autotrophic organisms require O_2 and CO_2. In both cases, the transport of gas through the S^0 blocks will control rates of oxidation and the resultant acid production.

Gas transport in unsaturated porous media can occur by diffusion or advection (Thorstenson and Pollock, 1989; Massman and Farrier, 1992; Shan and Stephens, 1995). Although diffusion of gas along concentration gradients is typically considered the dominant mechanism of gas transport through a porous medium (Mendoza and Frind, 1990a), advective gas transport can also be important if total pressure gradients caused by spatial variations in temperature, gas consumption or production rates, or changes in atmospheric and wind pressures exist (Thorstenson and Pollock, 1989).

The objective of this study was to quantify the relative importance of diffusive and advective gas transport in S^0 blocks. The study objective was attained by measuring *in situ* gas concentrations along a cross section through a commercial-scale block, conducting an *in situ* gas tracer experiment along two transects within the block, and conducting laboratory diffusion experiments. The findings from this study are applicable to other S^0 blocks as their construction is similar worldwide (Syncrude, 2004a; personal comm. Paul Davis, Alberta Sulphur Research Ltd. general manager).

3.3 Study site

The study was conducted on a commercial-scale S^0 block, referred to as the Phase 1 block, located at the Syncrude Canada Ltd. Mildred Lake mine site in northern Alberta, Canada (57°02'34.89"N, 111°38'36.14"W). The Phase 1 block was constructed between 1994 and 2004. At the time of this investigation, it was 359 m long × 168 m wide × 17.5 m high (at SRD04-129; Figure 3.1) and contained 900,000 m^3 of S^0 (Syncrude, 2004b). This block was constructed by pouring molten S^0 in lifts from three towers and allowing the S^0 to flow by gravity to areas of lower elevation within a confined area (see Phase 2 block, Figure 3.1). The maximum thickness of the lifts in any one area was less than 0.12 m. When the elevation of the S^0 blocks on either side of the

pouring towers reached the design height, the pouring towers were dismantled and S^0 was poured in lifts into the alley between the blocks (Figure 3.1).

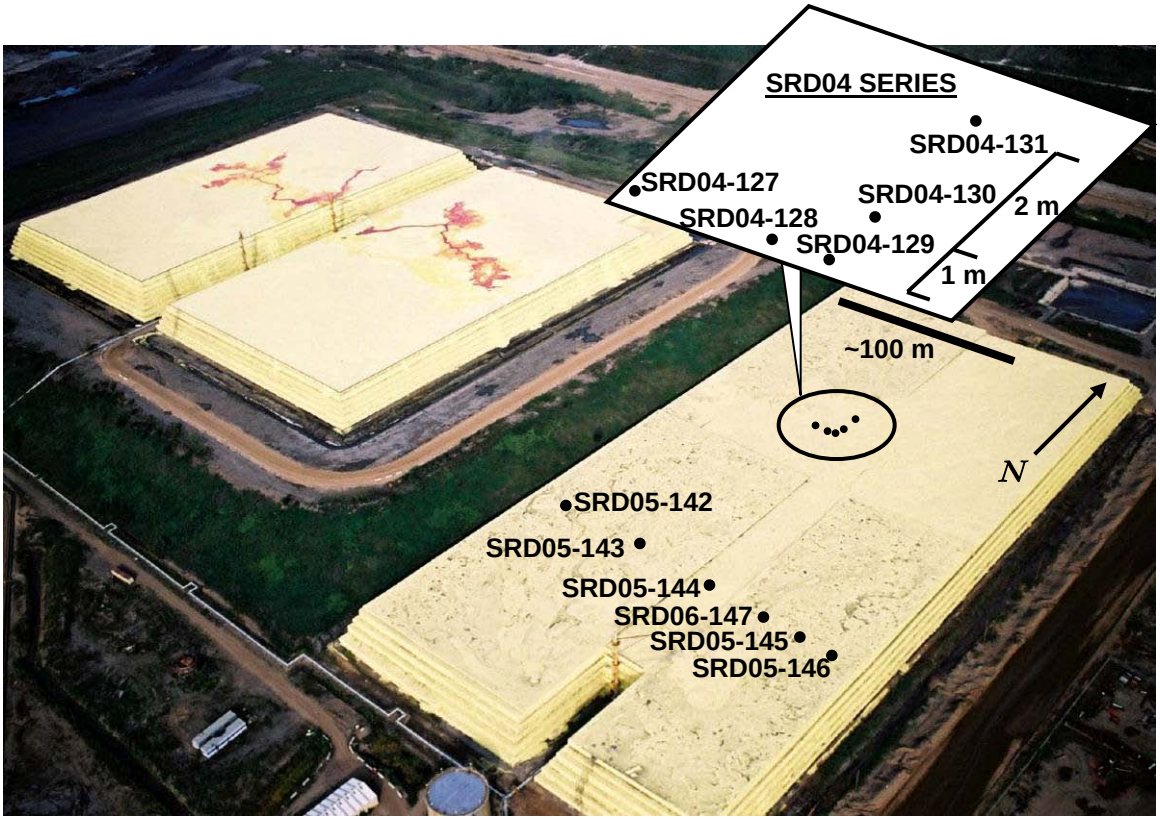

Figure 3.1. Aerial photo of the Phase 1 (lower right) and Phase 2 (under construction, upper left) S^0 blocks at the Syncrude Canada Ltd. oil sands mine in 2003. Black dots on the Phase 1 block represent locations of vertically-nested gas sampling ports (spacing of SRD04 series is presented in inset at an exaggerated scale for clarity). Dark texturing on the surface of the Phase 1 block is wind-blown sediment. The flow of molten S^0 in channels (orange) is visible on the Phase 2 block. The alley in the Phase 2 block and its remnants in the Phase 1 block are also evident.

3.4 Materials and methods

3.4.1 Laboratory Program

The diffusion of gases in porous media is most commonly described by Fick's first law:

$$J_i = -\theta_a \omega D_{air} \frac{dC_i}{dz} \qquad [3.1]$$

where J_i is the mass flux of species i (MT^{-1}); θ_a is the air-filled porosity; ω is the relative gas diffusivity (dimensionless; Moldrup et al., 2004), which is <1 and related to the

inverse of the tortuosity (τ) of the porous medium (ratio of gas particle path length to straight-line travel distance); C_i is the concentration of species i ($M \cdot L^{-3}$); z is the distance in the direction of the mass flux (L); and D_{air} is the diffusion coefficient of the species in free air ($L^2 \cdot T^{-1}$).

The effective coefficient of diffusion within the porous medium, D_e ($L^2 \cdot T^{-1}$), can be defined by:

$$D_e = \omega D_{air} \qquad [3.2]$$

Laboratory diffusion cells were used to estimate the ω of six unfractured S^0 cores collected in 2003 from depths of ~5-15 m (Table 3.1; Syncrude, 2004b).

Table 3.1. Thickness, porosity (n), and modelled ω values for S^0 core samples.

Core sample ID+	Sample height (cm)	Matrix porosity, n_m (%)*	Interconnected n_m (%)**	ω***
584A2	4.8	4.5	3.1	0.16
695E2	3.3	7.3	5.0	0.09
698E2	3.5	10.0	6.9	0.09
655C5	2.7	9.1	6.3	0.09
666C5	3.5	7.6	5.3	0.09
1485C5	2.9	14.3	9.9	0.12

+ Numeric prefix identifiers represent the depth below surface (in cm) from which the samples were collected.
* n_m values measured by Bonstrom (2007); n_m equal to $\theta_{a,m}$ for dry samples.
**Interconnected n_m ($\theta_{a,m}$) was 69% of n_m based on measurements by Bonstrom (2007).
***Average of N_2 and O_2 modelling

Core dimensions were measured using a digital caliper. The diffusion cells (Figure 3.5) were constructed from 7.62-cm diameter PVC pipe. A slip fit coupler was used to connect the upper section of the diffusion cell containing the S^0 core with a lower air-filled reservoir. The lower (air) reservoir ($\geq$560 cm^3) contained two three-way sampling valves and was isolated from the atmosphere, whereas the upper surface of the core was open to the atmosphere. The lower reservoir was flushed with ~2 L of pure N_2 gas for 2 min, with one sampling valve serving as an inlet for the pure N_2 gas and a second as an outlet to the atmosphere. A flushing rate of 1 $L \cdot min^{-1}$ resulted in a steady

but gentle flow of gas from the outlet valve so as to minimize pressure in the lower reservoir during N_2 flushing as well as advective transport of N_2 into the S^0 core. To ensure the flushing did not force N_2 into the core, preliminary tests were conducted where the top of the diffusion cell was sealed with cellophane and the flushing rate decreased until no outward displacement of the cellophane was observed (i.e., no upward advection of N_2).

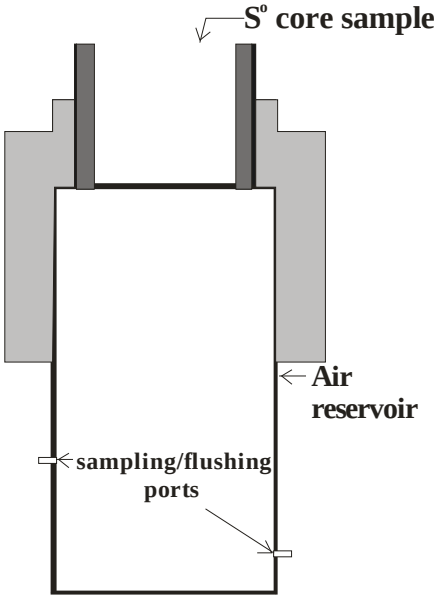

Figure 3.2. Schematic of gas diffusion cell (not to scale).

The experiments commenced when the N_2 gas was shut off and the two valves in the lower reservoir were closed. Samples were collected from the lower reservoir using one of the valves and a 10 cm^3 syringe with a three-way, luer lock valve attached to its sampling tip. As the samples were collected in the syringe, an equivalent volume of N_2 gas was injected into the lower reservoirs through the other three-way valve to ensure a constant total gas pressure in the lower reservoir. Prior to collecting the samples, 3 cm^3 of gas was withdrawn from the lower reservoirs and then expelled to the atmosphere. The three-way valves were then immediately switched to the reservoir and 7 cm^3 samples were withdrawn from the lower reservoir to ensure samples were not contaminated with atmospheric air. In total, approximately 60 cm^3 of gas was removed (and replaced) during each test, with <2% of the total reservoir volume ($\geq$560 cm^3) disturbed during each sampling event. The effect of disturbance of the diffusing gases

during sampling was evaluated by repeating two of the diffusion experiments with only one sampling event after a relatively long interval. Concentrations from these trials were very similar to those with five or more sampling events. As a result, sampling disturbances were considered to have a negligible effect on the diffusion experiments.

The concentrations of N_2 and O_2 ($[N_2]$ and $[O_2]$, volumetric %) of the samples were measured by gas chromatograph (GC). The analytical GC procedures for the diffusion cells were identical to those described below for *in situ* samples. Five to ten samples were withdrawn at approximately exponentially increasing time intervals over 2 d. Room temperature during the testing ranged from 20 to 22°C.

Gas diffusion in this study was simulated using the numerical model CTRAN/W® portion of the Geostudio 2007® modelling suite. This model quantifies diffusive fluxes based on Fick's laws, where Eq.[3.1] (Fick's first law) is used for steady-state conditions and Fick's second law:

$$\theta_a \frac{\partial C_i}{\partial t} = \theta_a D_e \frac{\partial^2 C_i}{\partial x^2} + \beta \qquad [3.3]$$

is applicable for transient conditions, where β ($M \cdot L^{-3} \cdot T^{-1}$) is the rate of gas production or removal (zero in the diffusion cells).

D_e values are a function of temperature (T) and were scaled by (Fuller et al., 1966):

$$\left(\frac{T}{T_o}\right)^{1.75} \qquad [3.4]$$

where T_o is the temperature (K) at which D is known.

Fick's second law was deemed appropriate for the laboratory diffusion cell experiments because this system can be assumed to be a binary gas mixture of O_2 and N_2, with equimolar fluxes of either gas occurring in opposite directions (Jaynes and Rogowski, 1983). Knudsen diffusion (collisions between gas molecules and S^0) was assumed to be minor as the air permeability (K_{air}) of the S^0 was $>6.9 \times 10^{-8}$ $m \cdot s^{-1}$ (Bonstrom, 2007), making the error from ignoring Knudsen diffusion <10% (Webb and Pruess, 2003). The diffusion cells were modelled assuming the S^0 core was dry and had an isotropic, homogeneous θ_a.

A 2-D grid was used to model [N_2] in the S^0 core and lower air-filled reservoir. A nodal spacing of 0.005 m was used for most of the model, but nodal spacing as small as 0.001 m was used adjacent to interfaces between the S^0 core and both the atmosphere and lower reservoir. The n_m (equivalent to matrix air-filled porosity, $\theta_{a,m}$ for dry samples) of each S^0 core was measured by Bonstrom (2007), who estimated the average interconnected n_m of unfractured S^0 to be 69% of the n_m. Thus, the $\theta_{a,m}$ used here in the diffusion cell modelling was 69% of the measured $\theta_{a,m}$. For modelling purposes, initial [N_2] and [O_2] both in the S^0 cores and the top boundary were assumed to be atmospheric (78.1 and 20.9%, respectively). The lower reservoir was simulated as a soil with a θ_a of unity. A backward difference time integration scheme was used, with timesteps (n=50) increasing exponentially over 3 d with an initial timestep of 10 s. Concentration data for the node at the same height as the sampling outlet were used to compare modelled and measured [N_2] and [O_2]. The binary D_{air} value for an N_2-O_2 mixture (i.e., D value in the lower reservoir) was 2.02×10^{-5} $m^2 \cdot s^{-1}$(at 20°C) (Weast, 1981). The D_e for N_2 and O_2 (Eq.[3.2]) was varied to obtain a best fit between simulated and measured [N_2] and [O_2], and thus provide estimates of the relative gas diffusivity (ω) for the S^0 samples.

3.4.2 Field program

Gas sampling ports and probes in the Phase 1 block: Nested gas sampling ports (n = 75) were installed at 10 locations on the Phase 1 block (Figure 3.1) in 0.15-m diameter boreholes drilled using solid-stem augers. The sampling ports were installed to facilitate an *in situ* SF_6 gas tracer experiment (SRD04 series) and to monitor [N_2], [O_2], [CO_2], and [CH_4] in the block (SRD05 and SRD06 series). SRD04-127 to SRD04-131 were installed in June 2004, SRD05-142 to SRD05-146 were installed September 2005, and SRD06-147 was installed March 2006.

SRD04 ports were installed along two perpendicular transects that intersected at SRD04-129 (Figures 3.1 and 3.3). SRD04 installations along the two transects were constructed of continuous multi-channel tubing (CMT; Solinst™) containing seven discrete sample channels within a 4.3-cm OD tube. One sampling port (area of approximately 1 cm^2) was cut and covered with screen in each channel at 2-m intervals along the CMT tubing. The CMT was then lowered down the borehole and the annular

space around each sampling port backfilled with 1 m of frac sand (particle diameter 0.5-1 mm) with the annular space between each sand interval backfilled with bentonite chips (1 m thickness) placed in 0.3-m lifts. The 1-m intake zone for each sampling port ensured the sand intake zone intersected at least one horizontal fracture, assuming an average horizontal fracture spacing of 0.6 m for fractures with apertures >1.4 mm (Bonstrom, 2007). Water (2 L) was poured on top of every 0.3-m bentonite lift to ensure at least some of the bentonite chips were hydrated, thus providing a barrier to gas migration along the annular space between sampling ports. Pea gravel (particle diameter 5-10 mm) was used as backfill in the 1-m interval around the 8.7-m deep sampling port at SRD04-129, which was used to inject the SF_6 tracer into the block (as described below). Pea gravel was used to ensure the injected SF_6 tracer would be readily introduced into the fractured S^0 block. The top of each CMT channel was fitted with a flow-through sampling valve and a three-way valve with luer lock connections for fastening to syringes during sampling. The gas port intakes at SRD04-127 to SRD04-131 were located in the block at elevations of 317.7, 315.7, 313.7, 311.7, 309.7, 307.7, and 305.7 m above sea level (asl) (depths of 2.7 to 14.7 m below surface). SRD04-127 and SRD04-131 were 3 m from SRD04-129; SRD04-128 and SRD04-130 were 1 m from SRD04-129.

The depths to the SRD05 and SRD06 sampling ports ranged from 320.2 to 305.6 m asl (depths of 0.5 to 15 m). CMTs were installed at the SRD05 instrumentation in the same manner as the ports for the SRD04 instrumentation. The gas probes at SRD06-147 were constructed using 6.35-mm OD polyethylene tubing with screened filters fitted across the down-hole end of the tubing. The gas probes were attached to a 1.27-cm diameter PVC pipe (with sealed ends) at the desired sampling points. The PVC pipe with attached gas ports were then lowered down the borehole. The probes at SRD04-133 were installed at 0.5, 1, 2, 3, 5, and 6 m below the surface. The backfilling method for these gas sampling probes was the same as for the CMT installations, however sand and bentonite thicknesses were reduced due to the smaller interval between probes.

SF_6 gas tracer experiment: An SF_6 gas tracer experiment was initiated on 7 May 2005. SF_6 is commonly used as a conservative gas tracer in unsaturated soils

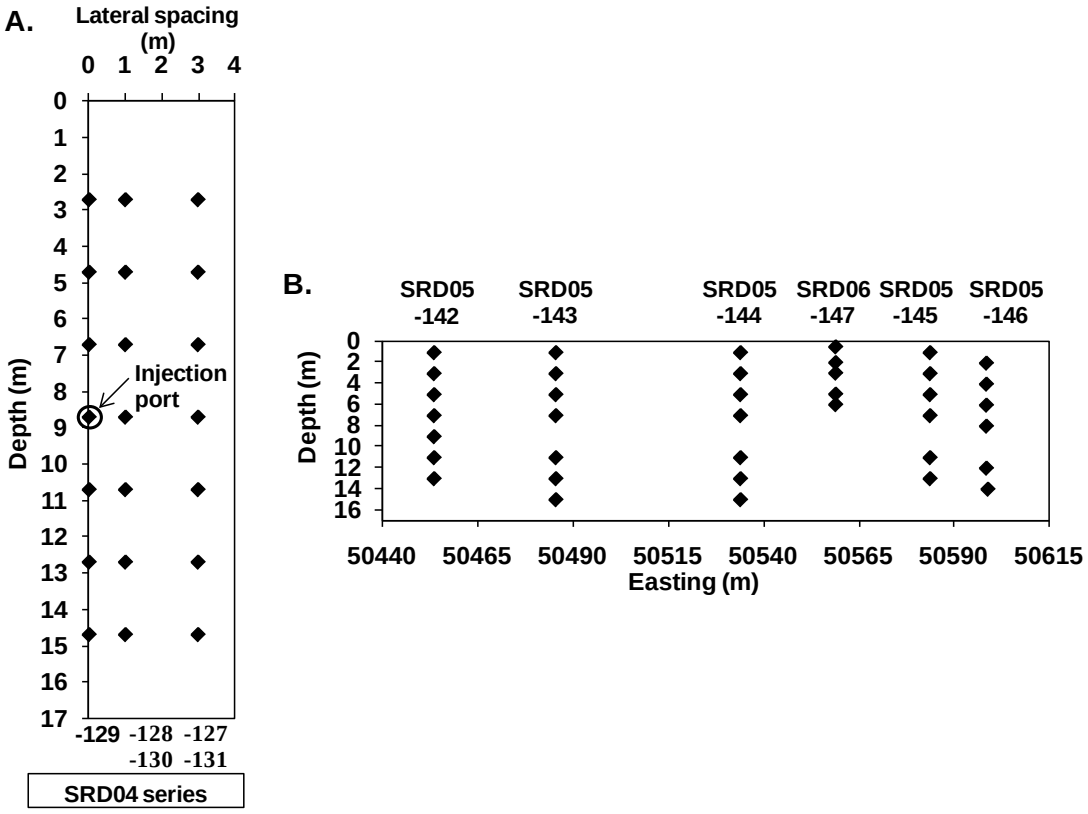

Figure 3.3. Spacing and depths of gas sampling ports in the Phase 1 block for: A. SF_6 tracer experiment (SRD04 series along two transects), and B. $[O_2]$, $[N_2]$, and $[CO_2]$ distributions.

(Tick et al., 2007; Johnson et al., 1998), including soils with high organic carbon and sulphur content (Wilson and MacKay, 1996). Sorption experiments (data not presented) confirmed the SF_6 behaved conservatively in the S^0. The SF_6 tracer was introduced into the block by flushing a mixture of 25 cm^3 of pure SF_6 in 1,960 cm^3 of air into the S^0 block at a depth of 8.7 m at SRD04-129 (Figure 3.1). The air used in the initial mixture was collected from the injection port 15 min prior to the SF_6 injection. Gas samples were collected from the SRD04 series ports on 16 occasions over 138 d, with ten suites of samples collected within the first 10 d after tracer injection. To minimize the disturbance from sampling on the migration of the tracer, gas purged from each port was collected in a gas-tight bag and re-injected into the S^0 block immediately after sample collection. After purging, 50 cm^3 of gas from each sampling port was collected in gas-tight 140-cm^3 syringes. Samples were analyzed for $[SF_6]$ within 4 h of collection by manual injection into an SRI 8610C GC, equipped with an electron capture detector

(^{63}Ni source) and a 2-m long, 1-mm diameter silcosteel® column maintained at a temperature of 60°C. The He carrier gas was delivered to the column at 50 psi; P-5 makeup gas was added inline to improve detection limits. A six-point calibration curve was created before and after each round of analyses by manual dilution of a 1 ppm (by volume) SF_6 standard (balance N_2). Samples with [SF_6] greater than the upper detection limit (500 ppbv) were diluted manually. The lower detection limit was 0.1 ppbv and the measurement accuracy was ± 5% of the concentration.

For presentation purposes, the sampling ports separated horizontally by 1 and 3 m from the injection port (at the same elevation as the injection port) are referred to as 1mh (read as 1 m horizontal from the injection port) and 3mh, respectively. The ports separated by 1 m horizontally and 2 m vertically (above and below) from the injection port are referred to as 1mh-2mv (read as 1 m horizontal, 2 m vertically below the injection port), and 1mh+2mv, respectively. The ports at elevations 2 and 4 m below and above the injection port are designated as -2mv and -4mv, and +2mv and +4mv, respectively.

Diffusion of the *in situ* SF_6 tracer was modelled using the CTRAN/W portion of the Geostudio 2007® modelling package (theory and equations presented above). The model mesh was axisymmetric with a radius of 15 m and a height of 17.4 m. Nodal spacing was 0.2 m. One day timesteps and a backward difference time integration scheme were used. Sensitivity analyses were performed to ensure the radius of the axisymmetric mesh was sufficiently large, and the nodal spacing and timesteps were sufficiently small, to not affect simulation results.

D_{air} for SF_6 was assigned a value of 8.9×10^{-6} $m^2\cdot s^{-1}$ (at 25°C; Werner and Hohener, 2003). In the model, S^0 was treated as an equivalent porous medium (EPM). The θ_a value of the EPM was considered to be the sum of interconnected $\theta_{a,m}$ and air-filled fracture porosity ($\theta_{a,f}$) values. The EPM ω value was estimated by assuming the contributions of the interconnected $\theta_{a,m}$ and $\theta_{a,f}$ to the EPM ω were proportional to their percentage of the EPM θ_a. In other words, the EPM ω was estimated assuming that gas diffusion occurred simultaneously through interconnected $\theta_{a,m}$ and $\theta_{a,f}$ in parallel. The ω for the $\theta_{a,m}$ component was measured in the diffusion cell testing (results presented below), and the ω for the $\theta_{a,f}$ was assumed to be unity. D_e values for the S^0 block were

corrected to a temperature of 11.1°C (mean temperature in the S^0 block, data not presented) using Eq. [3.4]. The use of a steady-state temperature was valid because temporal temperature variations below 5.5 m were <1°C.

For reasons discussed in the results section below, the mean [SF_6] for the two transects measured on day 12 was used as the initial concentration. This was applied to the model by assigning [SF_6] to concentrically layered spherical regions using linear interpolation to estimate [SF_6] between sampling ports. The gravel backfill surrounding the injection port was determined to have a negligible effect on simulations that started on day 12 and therefore was not included in the model grid.

The diffusive flux of SF_6 was quantified by Fick's second law because it was low in concentration and, therefore, diffusive fluxes of other gas components could be ignored (Jaynes and Rogowski, 1983). The scale of the SF_6 tracer modelling was assumed large enough in relation to the facture spacing that the S^0 block could be treated as a homogeneous porous medium.

In situ *gas concentrations:* [N_2], [O_2], [CO_2], and [CH_4] were measured at SRD05-142 to -146 and SRD06-147 on 9 December 2005, and 11 March, 17 May and 16 September 2006. Gas samples were collected in 140 cm^3 syringes after sufficient gas (100 mL per m of CMT channel) was purged from the sample tubing or channel to ensure gas from the appropriate depth was sampled. Samples were analyzed on site within 3 h of collection by manually injection into an Agilent Micro (M200) GC equipped with a thermal conductivity detector and 8-m columns packed with a 0.5-nm molecular sieve for separation of O_2 and N_2, and Poraplot for separation of CO_2 and CH_4. Carrier gases were argon for the O_2/N_2 column and helium for the CO_2/CH_4 column. Standards of atmospheric air (78.1% N_2 and 20.9% O_2), 100% N_2, and a calibration gas (10% O_2, 1.58% CO_2, and 0.52 % CH_4) were analyzed before and after each round of sampling. The lower detection limits for [O_2], [CO_2], and [CH_4] were 0.1, 0.05, and 0.005%, respectively.

In situ [N_2], [O_2], and [CO_2] cross sections were numerically modelled using Geostudio 2007® modelling suite. Inclusion of advective fluxes was achieved by generating a fluid (air) flow field in the SEEP/W® (fluid flow) portion of the Geostudio 2007® modelling suite, which simulated 2-D, steady-state head values according to:

$$\frac{\partial}{\partial x}\left(K_{a,x}\frac{\partial H}{\partial x}\right)+\frac{\partial}{\partial y}\left(K_{a,y}\frac{\partial H}{\partial y}\right)+F=0 \qquad [3.5]$$

where K_a is the air permeability ($L \cdot T^{-1}$) in the x and y directions, H is total head (L), and F is an applied flux (T^{-1}).

A 2-D mesh (97 m wide, 17.4 m high) was used (assuming approximately symmetrical conditions) to represent the western portion of the Phase 1 S^0 block (western edge to the middle of the pouring tower alley). Nodal spacing was 0.25 m in the upper 1 m and 0.5 m thereafter. Effects of compressibility, density gradients, and mechanical dispersion were not considered. A fluid (air) flow field was generated by removing O_2 from within the S^0 block at rates (F in Eq.[3.5]) equivalent to O_2 consumption rates (β_{O2}) and adding gas volume at rates equivalent to CO_2 production rates (β_{CO2}) at the base of the S^0 block (Figure 3.4, discussed in more detail below; see also Birkham et al., 2010). Volumetric gas removal rates applied in SEEP/W® were converted from β_{O2} and β_{CO2} values using the ideal gas law. Zero pressure head boundary conditions were applied to the upper and outer edge of the mesh.

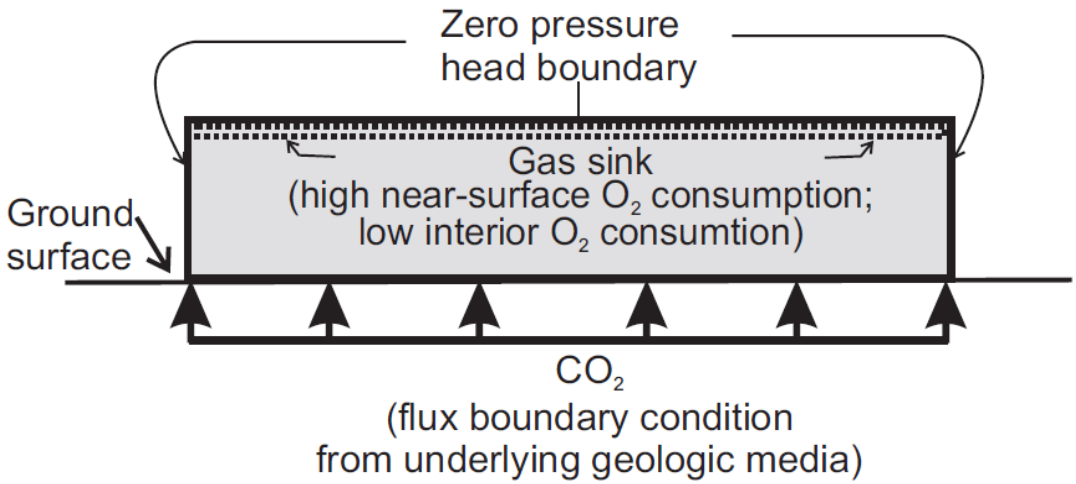

Figure 3.4. Conceptual schematic of gas head and flux boundary conditions, and internal gas sinks for S^0 block fluid (air) flow modelling.

For generating [N_2], [O_2], and [CO_2] cross sections, the fluid flow field was applied to CTRAN/W®, which incorporates mass transport due to diffusion and advection in addition to mass removal or addition rates (i.e., β_{O2} and β_{CO2}). To generate

simulated [N_2] distributions, the advective flow field was applied in CTRAN/W® with a constant atmospheric concentration of 78.1% applied to the top and outer edges. The advective mass influx of N_2 causes the [N_2] within the block to increase, creating a diffusive N_2 efflux from the S^0 block equal in magnitude but in the opposite direction to the advective flux. For the [O_2] distributions, the flow field was applied in CTRAN/W® with a constant atmospheric concentration of 20.9% applied to the top and outer edge boundaries, and mass removal rates (β_{O2}) applied within the block. For CO_2, a constant atmospheric concentration of 0.036% was applied to the top and outer edges in CTRAN/W, and a mass addition rate (β_{CO2}) was applied to the bottom boundary of the block. An iterative approach was used to choose β_{O2} and β_{CO2} rates that resulted in reasonable [N_2], [O_2], and [CO_2] distributions. D_{air} values for O_2 and CO_2 were 1.78×10^{-5} and 1.39×10^{-5} $m^2 \cdot s^{-1}$, respectively, at 0°C (Weast, 1981).

Only late summer conditions were considered and treated as quasi steady-state (assumption discussed below). In CTRAN/W®, steady-state conditions were attained by setting initial gas concentrations in the S^0 block to atmospheric values and running the simulation until gas concentrations reached steady-state. Assumptions for the spatial variation in θ, ω, and K_a are discussed below.

3.5 Results and discussion

3.5.1 Diffusion cell experiments

The thicknesses and $\theta_{a,m}$ of the samples along with best-fit ω values are included in Table 3.1. The modelled [N_2] and [O_2] corresponded very well to the measured values (data presented in Appendix), indicating gas migration in the experiments could be described accurately using Fick's law and gas transport in the cells was diffusion-dominated (i.e., no advective flux from flushing). Modelled ω for N_2 and O_2 differed by <0.02 and were within the analytical error of the [N_2] and [O_2]. The ω values in Table 3.1 (mean=0.11, s.d.=0.03, n=6) were within the wide range of values reported in the literature for different types of rock. For example, Boving and Grathwol (2001) report ω values for limestone and sandstone samples from 0.1-0.71 for n values of 10-40%, and ω values from 0.1-0.22 for n values of 3-10%. Further, Sato et al. (1997) report ω values of

0.16, 0.02, and 0.05 for n values of 1.2% (granodiorite), 2.8% (basalt), and 1.8% (mudstone), respectively.

For unsaturated soils, the value of ω (also commonly represented as the inverse of τ) can often be estimated as a function of n (or θ_a for a dry soil; Shen and Chen, 2007). In the literature, the most frequently used estimate of ω (Moldrup et al., 2004) as a function of θ_a is reported by Millington and Quirk (1961) where, for a dry soil:

$$\omega = \theta_a^{\frac{1}{3}} \qquad [3.6]$$

Using Eq. [3.6], estimates of ω for the S^0 samples tested in the diffusion cells range from 0.27-0.40, which are typically 2-3 times greater than ω values determined from the diffusion cell experiments. This suggests $\omega(\theta_a)$ equations for soils may not be appropriate for S^0. In addition, the simulated ω values of the S^0 samples did not exhibit a trend in relation to the interconnected $\theta_{a,m}$. For example, S^0 sample 584A2 (Table 3.1) had the lowest $\theta_{a,m}$ of the six samples tested but the greatest ω value. The inconsistent relationship between ω and n in this study was in keeping with the poor correlation reported by Bonstrom (2007) between K_a and n_m for 74 S^0 core samples with θ_m ranging from 7.1-24.2 %. We considered ω values measured in the diffusion cells as the lower limit for simulations of field conditions in the Phase 1 S^0 block, given only the most competent S^0 core samples, with likely the lowest ω values, were recovered for lab testing.

3.5.2 SF_6 gas tracer experiments

Measured and modelled [SF_6] for ten gas sampling ports are presented in Figure 3.5. The [SF_6] measured along the east-west and north-south transects yielded similar results, with the exception of the 1mh ports (Figure 3.5A). [SF_6] were as much as an order of magnitude greater in the first five days along the east-west transect (SRD04-128, 1mh) compared to the north-south transect (SRD04-130, 1mh). [SF_6] at both SRD04-128 and -130 did not equilibrate or follow a consistent decreasing trend until day 12 of the experiment. Therefore, for modelling purposes, the [SF_6] cross section for day 12 was used as the starting point for the transient model from day 12 to 137. Assuming the measured [SF_6] applied to a spherical volume, the estimated volume of SF_6 (including temperature correction) after day 12 was approximately one-third the original

injected volume. Inconsistencies in [SF_6] in the first 12 days at the 1mh ports, and differences between injected and estimated SF_6 volume after day 12, were assumed to be artifacts of the SF_6 injection into the S^0 block, with SF_6 being preferentially pushed towards SRD04-128.

Table 3.2 presents assumptions of EPM θ_a and ω values used in the modelling scenarios. EPM θ_a and ω values (7.3% and 0.21, respectively) estimated using average measured interconnected $\theta_{a,m}$ (6.5%), fracture porosity (n_f = 1.4%), matrix ω (0.11), and θ_w (0.6%) (Scenario A in Table 3.2) resulted in a reasonably good fit between modelled and measured [SF_6] for sampling ports at depths below or at the same elevation as the injection port (e.g., 1mh, 3mh, -2mv, 1mh-2mv in Figure 3.5). However, for sampling ports located at elevations above the injection port (results for +2mv, 1mh+2mv are presented as a representative example; Figure 3.5), modelled [SF_6] were as much as five times greater than measured [SF_6]. Modelled [SF_6] for Scenario B ($\theta_{a,f}$ decreased to 0.15%) also generally agreed with measured [SF_6] at elevations equal to or below the injection port reasonably well (Figure 3.5), but modelled [SF_6] for sampling ports located above the elevation of the injection port were as much as eight times greater than measured [SF_6]. The modelled [SF_6] for Scenario A and B cannot be considered unique because similar EPM θ_a and ω values could result from other assumptions for $\theta_{a,f}$, interconnected $\theta_{a,m}$, matrix ω, and fracture ω. For example, fracture ω might be less than one (e.g., due to fracture closure), or *in situ* matrix ω might have been different than those measured in the lab. $\theta_{a,f}$ was chosen as a variable in Scenarios A and B because it was the parameter most likely to vary in the S^0 blocks. Based on the best available estimates (Scenarios A and B), the modelling suggested an $\theta_{a,f}$ between 0.15% and 0.8% for depths greater than or equal to 8.7 m (injection port elevation).

Four possible mechanisms were considered to explain why modelled [SF_6] in Scenarios A and B were greater than measured [SF_6] for sampling ports above the injection port (upper 8 m): gravitational sinking, steady-state advective gas influx, spatial variation in θ_a and ω, and transient advective gas fluxes due to variations in barometric pressure. Sinking of the SF_6 plume due to gravitational settling should have a measurable effect only at very early times in the experiment (within the first hour) because the effect of gravitational settling is considered negligible when relative density

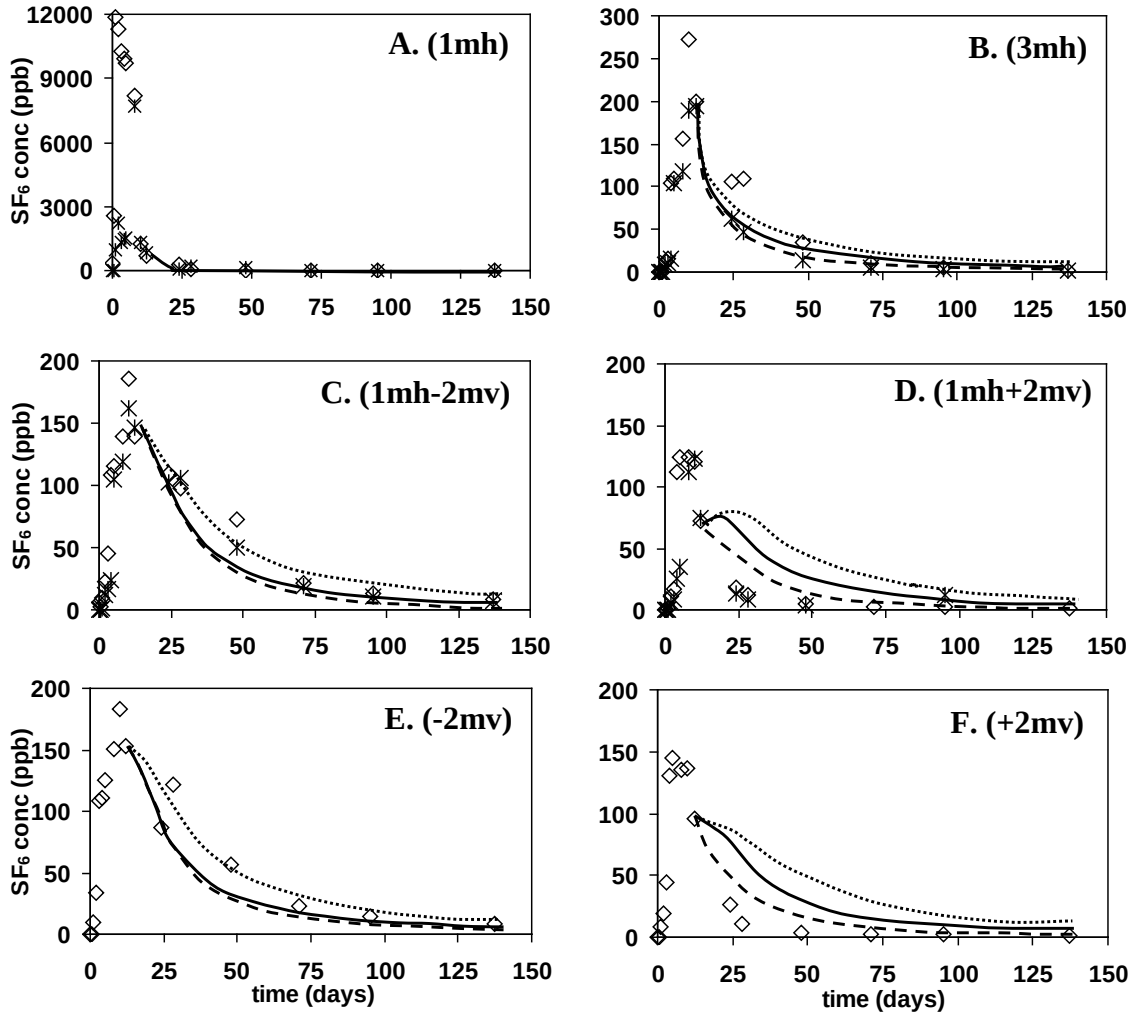

Figure 3.5. Measured and simulated [SF_6] for sampling ports located, in relation to the injection port: A) 1 m horizontally (1mh), B) 3m horizontally (3mh), C) 1 m horizontally and 2 m vertical below (1mh-2mv), D) 1 m horizontally and 2 m vertically above (1mh+2mv), E) 2 m vertically below (-2mv), and F) 2 m vertically above (+2mv). Simulated [SF_6] for Scenarios A (EPM θ_a=7.3%, ω=0.21), B (EPM θ_a=6.7%, ω=0.13), and C (EPM θ_a=9.0%, ω=0.44) are represented by solid, dotted, and dashed lines, respectively (lines are not distinguishable in A. 1mh graph). In graphs A to D, diamond symbols represent data from the east-west transect (SRD04-127, -128, -129) and star symbols represent data from the north-south transect (SRD04-129, -130, -131). In E and F, diamond symbols represent data from SRD04-129.

is <1.05 (Mendoza and Frind, 1990b; Shan and Stephens, 1995). We estimated the initial relative density of the initial SF_6 slug to have been about 1.05, with a maximum measured relative density of only 1.01 at the sampling ports. In the case of steady-state advective influx on the migration of the SF_6 tracer, we determined, by incorporating an advective flow field in the SF_6 tracer modelling (details discussed below), that the

Table 3.2. Parameters for SF_6 tracer simulations.

Scenario	EPM θ_a (%)	EPM ω	n (%)	n_m (%)	n_f (%)	interconnected $\theta_{a,m}$ (%)*	$\theta_{a,f}$ (%)**	matrix ω
A	7.3	0.21	10.8	9.4	1.4	6.5	0.8	0.11
B	6.7	0.13	10.2	9.4	0.8	6.5	0.2	0.11
C***	9.0	0.44	12.5	9.4	3.1	6.5	2.5	0.22

*Interconnected $\theta_{a,m}$ was 69% of n_m based on measurements by Bonstrom (2007).
**Average moisture content (0.6%; Birkham et al., 2009) assumed to occupy fracture porosity; $\theta_{a,f} = n_f - \theta_w$
***Scenario C parameters applied from 0-8.7 m depth and Scenario A parameters applied below 8.7 m.

velocity field had a negligible effect on the SF_6 migration and could not cause the rapid decrease in measured [SF_6] in the upper 8 m.

The effect of *in situ* θ_a and ω in the upper 8 m being greater than values below 8 m was evaluated in Scenario C (Table 3.2). Packer testing (*in situ* measurement of water permeability, K_w) in the Phase 1 S^0 block (Bonstrom, 2007) demonstrated K_w in the upper 8 m ranged from 8.5×10^{-5} to 2×10^{-4} m·s^{-1} while K_w below 8 m ranged from 3×10^{-6} to 1.5×10^{-5} m·s^{-1}. Bonstrom (2007) hypothesized the decreased K_w below 8 m was the result of the closure of fractures due to increased overburden pressure. Because Moldrup et al. (2001) report gas diffusivity and K_w in porous media are highly correlated, we assumed the relatively greater K_w in the upper 8 m of the S^0 block reflected an increased ω (and $\theta_{a,f}$). In Scenario C, the n (total porosity) and ω in the upper 8 m were increased to 12.5% and 0.44 respectively. These were considered to be maximum estimates as the n was equal to the combined volume shrinkage during solidification (7%) and mineral change (5.5%). The n_f in Scenario C (3.1%) was 2.2 times greater than the average measured n_f of 1.4%, and the matrix ω (0.22) was two times greater than the average matrix ω measured in the diffusion cell experiments. Despite the increased EPM θ_a and ω, modelled [SF_6] in the top 8 m (e.g., +2mv, 1mh+2mv; Figure 3.5) for Scenario C was still as much as three times greater than measured [SF_6], suggesting increased θ_a and ω in the upper 8 m were, at most, only partially responsible for the greater modelled [SF_6] values.

Advective fluxes due to barometric and wind-induced pressures were also considered as factors that could result in the measured [SF_6] in the upper 8 m being less than modelled [SF_6]. Nilson et al. (1991) conclude advective gas transport resulting from changes in barometric pressure is particularly important for fractured, unsaturated media. They approximated intrusion of atmospheric gas into the subsurface with:

$$\frac{\Delta L}{L_o} \approx \frac{\Delta p}{p_o}\left(\frac{\theta_{a,f} + \theta_{a,m}}{\theta_{a,f}}\right) \qquad [3.7]$$

where ΔL is the displacement of a gas particle at the top of an unsaturated medium, L_o is the depth of the unsaturated medium, Δp is the change in barometric pressure, and p_o is the initial barometric pressure. Eq. [3.7] assumes the volumetric expansion or compression of gas in an unsaturated medium is dependent on the total pore gas volume (matrix and fracture porosity), but the expansion/compression is limited to the fracture porosity because of the greater K_a of the fracture porosity relative to matrix porosity. Nilson et al. (1991) estimated that even for relatively high matrix K_a (6×10^{-7} m·s^{-1}) and low fracture porosity (0.01%, assuming fracture spacing and aperture of 1 m and 1×10^{-4} m, respectively), greater than 99% of gas displacement in response to a barometric pressure change would occur in the fractures. During barometric pressure cycles, SF_6 would be removed from the S^0 block. In response to an increase in barometric pressure, fresh atmospheric air would be pushed into the block along fractures to a depth of ΔL and SF_6 would diffuse from the matrix into the fresh air in the fractures. SF_6 would then be moved from the fractures to the atmosphere when gas is withdrawn during a decrease in barometric pressure. Temporal variation in SF_6 mass (estimated by multiplying measured [SF_6] by an associated pore gas volume) supports the hypothesis that SF_6 was flushed from the upper 8 m of the block during the tracer experiment. Estimated SF_6 mass in the upper 8 m decreased by 80-90% between days 12 and 47 of the tracer experiment, while estimated SF_6 mass below 8 m was constant with time.

Assuming an L_o of 17.4 m (height of Phase 1 S^0 block), $\theta_{a,f}$ of 0.15%, interconnected $\theta_{a,m}$ of 6.5% (Scenario B), and a barometric pressure cycle with a Δp to p_o ratio of 1%, atmospheric air would intrude into the block through fractures to a depth of 7.7 m (ΔL). During the tracer experiment, 53, 23, and 4 barometric pressure cycles occurred with Δp to p_o ratios ≥ 0.5, 1, and 2%, respectively (barometric pressure data

from Environment Canada online database for Fort McMurray, Alberta station; data not presented). Although detailed modelling of the effect of pressure cycles on the SF_6 tracer experiment was beyond the scope of this study, these approximations suggest at least partial flushing of the top 8 m due to pressure cycles is a reasonable assumption. Wind-induced pressure fluctuations would also cause flushing cycles; however, wind-induced uplift pressures would have rarely exceeded 1 kPa (estimate from Wind-RCI model; Baskaran, 2008; data not presented).

The SF_6 tracer modelling provided reasonable estimates of EPM θ_a and ω for depths below 8 m; however, because of advective gas flushing, accurate estimates of EPM θ_a and ω were not possible for depths of 0-8 m. The minimum (Scenario B) and maximum (Scenario C) EPM θ_a and ω estimates for depths from 0-8 m were expected to be 6.7% and 0.13, and 9% and 0.44, respectively.

3.5.3 *In situ* [N_2], [O_2], and [CO_2] distributions

Isopleths generated for [N_2], [O_2] and [CO_2] for 16 September 2006 (Figure 3.6) are representative of quasi-steady state conditions for the summer months when temperatures and H_2SO_4 production rates in the S^0 were greatest (data not presented). The 16 September 2006 [N_2] data were approximately 3-5% greater, and [O_2] 3-5% less, than for 9 December 2005 and 11 March 2006 (data not presented). [CO_2] varied by approximately 1% during the year. [N_2] within the block was as great as 98% with steep [N_2] gradients over the top 1-5 m, and more gradual gradients towards both the bottom of the block and the outer edges. These [N_2] gradients were indicative of advective influx of atmospheric gases into the block (Molins and Mayer, 2007; Amos et al., 2005; Thorstenson and Pollock, 1989). For example, in subsurface environments where denitrification or N_2 fixation are not occurring (i.e., N_2 is non-reactive), N_2 has a net flux of zero at the ground surface. Any advective N_2 influx at surface must be balanced by a diffusive flux of equal magnitude in the opposite direction. As a result, [N_2] gradients develop.

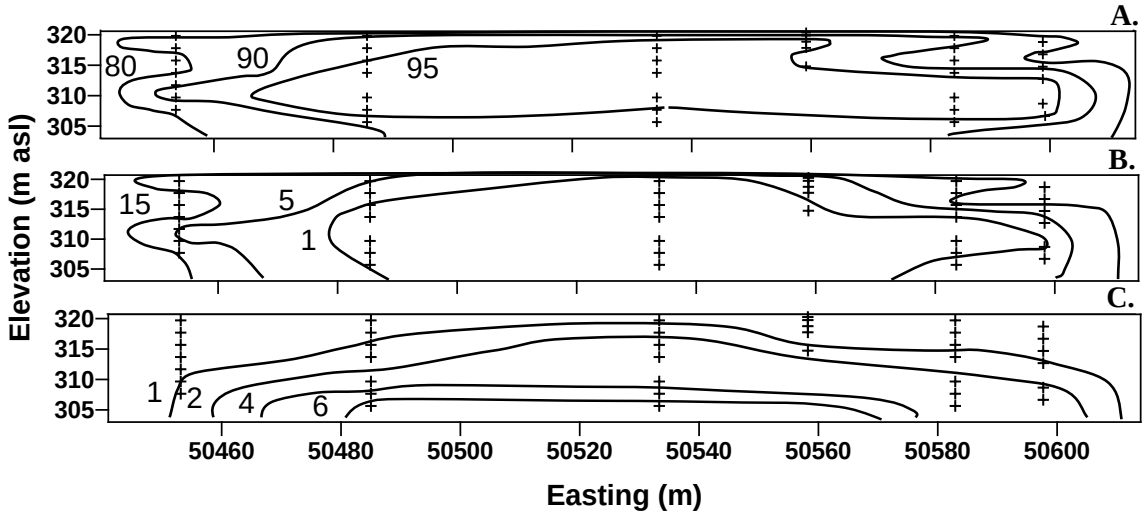

Figure 3.6. Isopleths of A) [N_2], B) [O_2], and C) [CO_2] in the Phase 1 block along an east-west transect from SRD05-142 to -146. Sampling date was 12 September 2006. Crosses represent sampling ports at, from left to right: SRD05-142, SRD05-143, SRD05-144, SRD06-147, SRD05-145, and SRD05-146. Atmospheric [N_2], [O_2], and [CO_2] were 78.1, 20.9, and 0.036%, respectively.

In situ [O_2] and [CO_2] (Figure 3.6B and C) indicated the advective influx of atmospheric gas was the result of O_2 consumption within the block with an absence of equimolar production of another gas to maintain total pressures at approximately atmospheric values. In other words, the [O_2]+[CO_2] in the block ([CH_4] was below the detection limit) was less than [O_2]+[CO_2] in the atmosphere (approximately 21%). Advective fluxes were also attributed to this mechanism by Molins and Mayer (2007), Binning et al. (2007), and Amos et al. (2005). Birkham et al. (2010) present a more detailed discussion of the [O_2] and [CO_2] profiles as they relate to the type, spatial variability, and rate of reactions occurring within the block.

Modelled [N_2], [O_2], and [CO_2] distributions presented in Figure 3.7 were simulated by applying O_2 consumption rates (β_{O2}) of 0.68 mol O_2 $m^{-3}\cdot d^{-1}$ in the top 1 m and $<2.7\times10^{-4}$ mol O_2 $m^{-3}\cdot d^{-1}$ in the rest of the S^0 block (where [O_2] was >0). Modelled [O_2] were insensitive to β_{O2} in the interior of the block when the interior β_{O2} was $<2.7\times10^{-4}$ mol O_2 $m^{-3}\cdot d^{-1}$. EPM θ_a and ω were assumed to be 7.3% and 0.21 (equivalent to Scenario A), except for depths of 0-1.5 m in the outer 35 m where θ_a and ω were increased to 9% and 0.44 (Scenario C). The increased θ_a and ω from 0-1.5 m in the outer 35 m decreased modelled gradients of [N_2], [O_2], and [CO_2] so that they corresponded better with measured values. Increased *in situ* θ_a and ω in the upper 1.5 m of the outer 35

m were not observed, but might have been caused by differential settling of the S^0 block, decreased confinement near the block edge, or increased distance from the pouring towers (finer and more tortuous flow channels of molten S^0 during construction).

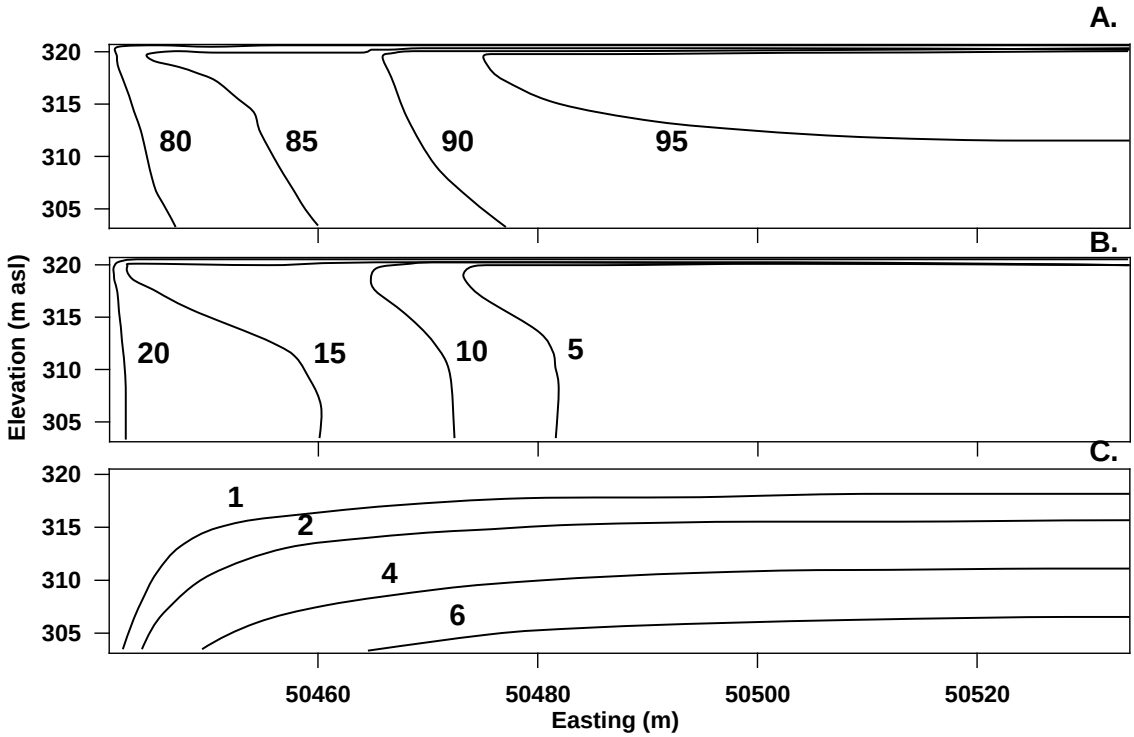

Figure 3.7. Modelled isopleths of A) [N_2], B) [O_2], and C) [CO_2]. Contour labels are volumetric concentrations. The right vertical boundary of the cross sections represents the middle of the S^0 block pouring alley.

The modelled [N_2], [O_2], and [CO_2] in Figure 3.7 were not unique solutions, as similar results could be simulated by increasing or decreasing the θ_a, ω, and β_{O2}. For example, when θ_a and ω were decreased to 6.7% and 0.13 respectively (Scenario B), the best-fit β_{O2} in the upper 1 m was 0.39 mol O_2 $m^{-3} \cdot d^{-1}$. If maximum estimates of θ_a and ω (9% and 0.44, respectively; Scenario C) were assumed, the best-fit β_{O2} in the upper 1 m was 1.8 mol O_2 $m^{-3} \cdot d^{-1}$.

The application of high β_{O2} in the top 1 m was required to simulate the steep vertical [O_2] and [N_2] gradients near the top of the S^0 block. A similar result could have been achieved by assuming relatively low EPM θ_a and ω (greater resistance to gas diffusion) at the surface of the S^0 block, but increased near-surface β_{O2} was considered more probable given increased nutrient availability from wind-blown sediments on the

block surface (see Figure 3.1) and microbiological analyses (Birkham et al., 2010).

An influx of CO_2 into the S^0 block was simulated by applying a CO_2 production rate (β_{CO2}) of 3.7×10^{-3} mol CO_2 $m^{-2}\cdot d^{-1}$ to the bottom boundary of the block. The inclusion of the β_{CO2} along the bottom of the block was required to generate a [CO_2] distribution with gradients throughout the block in the outward direction, but also to create [N_2] contours that extended laterally across the bottom of the block (i.e., 95% [N_2] contour in Figure 3.7). [N_2] gradients in the downwards direction (i.e., [N_2] contours extending laterally across the block) were required to balance the vertical advective fluxes created by the influx of CO_2 along the bottom boundary. Reactivity of CO_2 in the S^0 block was negligible (Birkham et al., 2010) and not included in this model. More detailed discussions of CO_2 fluxes within the S^0 block, O_2 consumption, and H_2SO_4 production are presented in Birkham et al. (2009b). The [CO_2] in the block was attributed to CO_2 production in the geologic media beneath the S^0 as CO_2 production rates associated with S^0 oxidation were very low (Birkham et al., 2010).

With initial [N_2] and [CO_2] set to atmospheric concentrations throughout the block, simulated steady-state conditions were reached in N_2 and CO_2 simulations after 3 yr with 60 min timesteps. Steady-state [O_2] were reached after 140 d with 15 min timesteps, and initial [O_2] of 20.9% in the outer 40 m and 0% elsewhere. Modelling was sensitive to K_a only if K_a at depths of 0-8m was less than K_a at depths of 8-17.4 m. As K_a is unlikely to increase with depth, a uniform K_a approximation (3×10^{-7} $m\cdot s^{-1}$) was considered adequate.

From the [O_2] model, advective influx was estimated at 21% of the total O_2 mass flux into the S^0 block (advective plus diffusive). Therefore, determining O_2 influx without the inclusion of advective influx would likely result in substantial underestimation. The occurrence of an advective atmospheric influx is important because it increases both H_2SO_4 production (i.e., total O_2 influx for S^0 oxidation) within the S^0 block and the potential for environmental loadings of H_2SO_4 in S^0 block drainage. The potential for advective O_2 influx is an important consideration in S^0 storage strategies because only cover designs that restrict air flow would effectively minimize O_2 flux (and H_2SO_4 production). Potential air flowpaths could include fractures or

cracks in soil covers, imperfections in synthetic covers, or pathways along monitoring instrumentation.

As demonstrated by the results of the SF_6 tracer experiment, barometric pumping of the fracture porosity in the upper 8 m was likely occurring. However, we determined its inclusion would have a negligible effect on modelled β_{O2} in the upper 1 m. Although ignoring advective O_2 influx during times of increasing barometric pressure resulted in an underestimation of modelled β_{O2}, this error would be balanced by an overestimation of β_{O2} during times of advective O_2 efflux resulting from decreasing barometric pressure. Diffusion of atmospheric O_2 from the fractures to the matrix porosity during times of increased barometric pressure may have resulted in a small net O_2 influx (underestimation of β_{O2}) from barometric pumping, however the complexity and short timescale (typical pressure cycles less than 2 d) of these effects was beyond the limitations of our sampling and modelling methods.

The modelled [N_2], [O_2], and [CO_2] distributions demonstrated the interdependency between the fluxes of gas species and the importance of considering multiple gas species in characterizing sub-surface geochemical reactions. Substantial errors in flux estimates of reactive gases could result if multiple gas species are not considered, and gradients of non-reactive species could be difficult, or impossible, to correctly interpret.

3.6 Acknowledgments

Ron Lewko, Robert Mahood and Gord McKenna provided field support, and Julie Robertson, Rob Holben, Matt Harker, and Greg Newman (Geo-Slope International Ltd.) provided technical assistance. We acknowledge the funding provided the Natural Sciences and Engineering Research Council of Canada and Syncrude Canada Ltd.

3.7 References

Amos RT, KU Mayer, BA Bekins, GN Delin, and RL Williams. 2005. Use of dissolved and vapor-phase gases to investigate methanogenic degradation of petroleum hydrocarbon contamination in the subsurface. Water Resources Research 41, Art. No. W02001.

Baskaran BA. 2008. Wind-roof calculator on the internet (Wind-RCI). National Research Council, Canada. www.irc.nrc-cnrc.gc.ca/bes/prsi/rci_e.html

Beffa T, M Blanc, and M Aragno. 1996. Obligately and facultatively autotrophic, sulfur- and hydrogen-oxidizing thermophilic bacteria isolated from hot composts. Archives of Microbiology 165: 34-40.

Binning PJ, D Postma, TF Russell, JA Wesselingh, and PF Boulin. 2007. Advective and diffusive contributions to reactive gas transport during pyrite oxidation in the unsaturated zone. Water Resources Research 43(2), Art. No. W02414.

Birkham TK, MJ Hendry, SL Barbour, SK Carey and JR Lawrence. 2009. Water balance and flux through sulphur blocks. *Submitted to Canadian Geotechnical Journal, June 2009.*

Birkham TK, MJ Hendry, and SL Barbour. 2010. Controls and rates of acid production in commercial-scale sulphur blocks. *In Press to Journal of Environmental Quality, June 2009.*

Bonstrom, K. 2007. Physical controls on water migration in elemental sulphur blocks. M.Sc. thesis, Dept. Geological Sciences, University of Saskatchewan. Saskatoon, Saskatchewan, Canada.

Boving TB and P Grathwohl. 2001. Tracer diffusion coefficients in sedimentary rocks: correlation to porosity and water permeability. Journal of Contaminant Hydrology 53: 85-100.

ERCB (Alberta, Canada), 2008. Alberta's energy reserves 2007 and supply/demand outlook 2008-2017. ST98-2008.

Fuller EN, PD Schettler, and CJ Giddings. 1966. A new method for prediction of binary gas-phase diffusion coefficients. Industrial and Engineering Chemistry Research 58(5): 19-27.

Janzen HH and JR Bettany. 1987a. Measurement of sulfur oxidation in soils. Soil Science 143(6): 444-452.

Janzen HH and JR Bettany. 1987b. The effect of temperature and water potential on sulfur oxidation in soils. Soil Science 144(2): 81-89.

Jaynes DB and AS Rogowski. 1983. Applicability of Fick's law to gas diffusion. Soil Science Society of America Journal 47: 425-430.

Johnson PC, C Bruce, RI Johnson, and MW Kemblowski. 1998. In situ measurement of effective vapor-phase porous media diffusion coefficients. Environmental Science and Technology 32: 3405-3409.

Knickerbocker C, DK Nordstrom, and G Southam. 2000. The role of "blebbing" in overcoming the hydrophobic barrier during biooxidation of elemental sulfur by *Thiobacillus thiooxidans*. Chemical Geology 169: 425-433.

Kosich, D. June 20, 2008. Sulphur, potash prices soar last month as base and precious metals decline. International Business Times.

Lawrence JR and JJ Germida. 1991. Microbial and chemical characteristics of elemental sulfur beads in agricultural soils. Soil Biology and Biochemistry 23(7): 617-622.

Massmann J and DF Farrier. 1992. Effects of atmospheric pressures on gas transport in the vadose zone. Water Resources Research 28(3): 777-791.

Mendoza CA and EO Frind. 1990a. Advective-dispersive transport of dense organic vapors in the unsaturated zone 1. Model development. Water Resources Research 26(3): 379-387.

Mendoza CA and EO Frind. 1990b. Advective-dispersive transport of dense organic vapors in the unsaturated zone 1. Sensitivity analysis. Water Resources Research 26(3): 388-398.

Meyer, B. 1977. Sulphur, energy and environment. Elsevier Scientific, Amsterdam.

Millington RJ, and JP Quirk. 1961. Permeability of porous solids. Transactions of the Faraday Society 57: 1200-1207.

Moldrup P, T Olesen, T Komatsu, P Schjonning, and DE Rolston. 2001. Tortuosity, diffusivity, and permeability in the soil liquid and gaseous phases. Soil Science Society of America Journal 65: 613-623.

Moldrup P, T Olesen, S Yoshikawa, T Komatsu, and DE Rolston. 2004. Three-porosity model for predicting the gas diffusion coefficient in undisturbed soil. Soil Science Society of America Journal 68: 750-759.

Molins S, and KU Mayer. 2007. Coupling between geochemical reactions and multicomponent gas and solute transport in unsaturated media: a reactive transport modelling study. Water Resources Research 43(5), Art. No. W05435.

Nilson RH, EW Peterson, KH Lie, NR Burkhard, and JR Hearst. 1991. Atmospheric pumping: a mechanism causing vertical transport of contaminated gases through fractured permeable media. Journal of Geophysical Research 96(B13): 21933-21948.

Ober JA. 2002. Materials flow of sulfur. U.S. Geological Survey. Open-file report 02-298.

Ober JA. 2007. U.S. Geological Survey, Mineral Commodity Survey, January, 160-161.

Proce, B. October, 2006. Growing issue: Oilsands mining companies are looking for ways to manage growing levels of sulphur production from landlocked Athabasca oilsands region. Oilsands Review.

Salo-Zieman VLA, PHM Kinnunen, and JA Puhakka. 2006. Bioleaching of acid-consuming low-grade nickel ore with elemental sulfur addition and subsequent acid generation. Journal of Chemical Technology and Biotechnology 81: 35-40.

Sato H, T Shibutani, and M Yui. 1997. Experimental and modelling studies on diffusion of Cs, Ni and Sm in granodiorite, basalt and mudstone. Journal of Contaminant Hydrology 26: 119-133.

Shan C and DB Stephens. 1995. An analytical solution for vertical transport of volatile chemicals in the vadose zone. Journal of Contaminant Hydrology 18: 259-277.

Shen L and Z Chen. 2007. Critical review of the impact of tortuosity on diffusion. Chemical Engineering Science 62: 3748-3755.

Syncrude Canada Ltd. 2004a. Geo-environmental observations of 17 sulphur blocks in Alberta. Research Dept. Progress Report 33(2).

Syncrude Canada Ltd. 2004b. Geochemical characterization of a large sulphur block at Syncrude: results from the 2003 field investigation. June 21, 2004.

Thorstenson DC and DW Pollock. 1989. Gas transport in unsaturated zones: multicomponent systems and adequacy of Fick's laws. Water Resources Research 25(3): 477-507.

Tick GR, CM McColl, I Yolcubal, and ML Brusseau. 2007. Gas-phase diffusive tracer test for the in-situ measurement of tortuosity in the vadose zone. Water, Air and Soil Pollution 184: 355-362.

Webb SW, and K Pruess. 2003. The use of Fick's law for modelling trace gas diffusion in porous media. Transport in Porous Media 51: 327-341.

Weast RC, Editor. 1981. CRC Handbook of Chemistry and Physics, 62nd Ed., CRC Press.

Werner D, and P Hohener. 2003. In situ method to measure effective and sorption-affected gas-phase diffusion coefficients in soils. Environmental Science and Technology 37: 2502-2510.

Wilson RD and DM Mackay. 1996. SF_6 as a conservative tracer in saturated media with high intragranular porosity and high organic carbon content. Ground Water 34(2): 241-249.

4.0 CONTROLS AND RATES OF ACID PRODUCTION IN COMMERCIAL-SCALE SULPHUR BLOCKS

Preface

Water draining from S^0 blocks is among the most acidic solutions described in the earth sciences literature. Addressing and mitigating this environmental concern requires a conceptual model describing the transformation of fresh water to highly acidic drainage as it water infiltrates through a S^0 block. This third manuscript builds on the findings of Manuscripts 1 and 2 (Chapters 2 and 3) to provide a more comprehensive conceptual model identifying where, and at what rates, H_2SO_4 is produced in S^0 blocks. In addition to the control of water and O_2 availability, the sensitivity of S^0 oxidation rates to temperature was measured in laboratory experiments and used to interpret seasonal variations of *in situ* H_2SO_4 production rates. *In situ* H_2SO_4 production rates were estimated by modelling O_2 consumption rates and compared with measured SO_4 efflux in drainage water from a S^0 block to provide validation of the O_2 (S^0 oxidation) modelling. A conceptual model is proposed that describes the mechanisms by which water is acidified as it flows through the block, and strategies for limiting H_2SO_4 production in S^0 blocks are suggested.

Reference: Birkham TK, MJ Hendry, and SL Barbour. Controls and rates of acid production in commercial-scale sulphur blocks. In Press to Journal of Environmental Quality, 2010.

4.1 Abstract

Acidic drainage (pH 0.4-1.0) from oxidizing sulphur (S^0) blocks is an environmental concern in regions where S^0 is stockpiled on ground surface. In this study, the locations, controls and rates of H_2SO_4 production in commercial-scale S^0 blocks (~1-2x10^6 m^3) in northern Alberta, Canada were estimated. *In situ* modelling of O_2 concentrations ($[O_2]$) suggest 70 to >97% of the annual H_2SO_4 production occurs in the upper 1 m of the blocks where temperatures increase to >15°C during the summer. Laboratory experiments show S^0 oxidation rates are sensitive to temperature (Q_{10}=4.3) and dependent on the activity of autotrophic S^0-oxidizing microbes. The annual efflux of SO_4 in drainage water from a S^0 block (5.5×10^5 kg) was within the estimated range of annual SO_4 production within the block (2.7×10^5-1.2×10^6 kg), suggesting H_2SO_4 production and removal rates were approximately equal during the study period. The low mean relative humidity within the block (68%, s.d.=17%, n=21) was attributed to osmotic suction from elevated H_2SO_4 concentrations and suggests a mean *in situ* pH of approximately -2.1. Low pH of drainage waters was attributed to mixing of fresh infiltrating water and low-pH *in situ* water. Heat generation during S^0 oxidation was an important factor in maintaining elevated temperatures (mean=11.1°C) within the block. Implications of this research are relevant globally as construction methods and physical properties of S^0 blocks are similar worldwide.

4.2 Introduction

The global market for elemental sulphur (S^0) from 1992-2005 was unique in that the annual supply from bitumen upgrading, natural gas plants, coking plants, and non-ferrous metal smelters exceeded demand by approximately 1-3 Mt (Kitto, 2005). As a result, S^0 prices decreased from $140 USD (current $) per t in 1985 to $20-$60 USD per t from 2001 to 2005 (Kitto, 2005). Producers of S^0 in locales with the highest transportation costs or inadequate infrastructure (e.g., northern Canada, Middle East, Caspian Sea regions) have been at the greatest economic disadvantage and, as a result, have stored large quantities of S^0 (in the order of tens of Mt) (Proce, 2006). The global S^0 supply and demand in the past three years (2005-2008) has been relatively balanced and prices increased to as much as $700 US per t (Kosich, 2008), with S^0 re-melted from

the most commercially-viable S^0 stockpiles. However, forecasts predict a return to a S^0 surplus from 2011-2017 and continued widespread stockpiling of S^0 (ERCB, 2008). In Canada, the world's largest S^0 producer, 11.6 Mt of S^0 was stockpiled as of April 2008 (ERCB, 2008) and the rate of S^0 stockpiling is expected to increase. Total annual S^0 production from bitumen upgrading at Canadian oilsands mining operations in northeastern Alberta was 1.5 Mt in 2007 and is expected to increase to 5.3 Mt by 2017 (ERCB, 2008).

Sulphur is typically stored by pouring molten S^0 (>115°C) in a confined area on the ground surface in lifts about 0.1 m thick. The S^0 solidifies and, as sequential lifts of S^0 build up, a large above-ground S^0 block is constructed (typically hundreds of thousands of cubic meters; width/length dimensions 100-200 m × 10-25 m high). A major environmental concern with this above-ground storage is the oxidation of S^0 to H_2SO_4 as evidenced by the low pH (0.4-1.0) and high SO_4 concentrations (>30 $g \cdot L^{-1}$) of water that seeps from the base of these blocks. Over long storage times, this acid could result in the acidification and salinization of waters and soils adjacent to the S^0 blocks.

Because S^0 surpluses are a relatively recent occurrence, little is known about the controls or rates of acid production (S^0 oxidation) in S^0 blocks. Research into reaction rates and controls on S^0 has, however, been conducted under laboratory conditions for purposes of crop fertilization (Attoe and Olson, 1966; Janzen and Bettany, 1987a; Janzen and Bettany, 1987b; Lawrence et al., 1988a; Lawrence et al., 1988b; Hyne et al., 1996; Wen et al., 2001). In addition, extensive research has been conducted into the rates and controls of the oxidation of sulphide mine tailings and waste rock from base metal and uranium mines (*c.f.,* Elberling et al., 1994; Lawrence et al., 1997; Elberling and Damgaard, 2001).

Arguably, the fundamental control of the oxidation of S^0 to SO_4 (i.e., production of H_2SO_4) is the presence and activity of heterotrophic and autotrophic microorganisms (Janzen and Bettany, 1987a). Autotrophs use the energy transferred during S^0 oxidation for growth and the fixation of C-1 compounds (e.g., CO_2; Lizama et al., 2002). S^0 oxidation during heterotrophic activity is mainly incidental (Baldensperger, 1976) as organic material is oxidized for energy and growth with CO_2 produced. S^0 oxidation by

both heterotrophic and autotrophic microorganisms requires molecular O_2 as an electron acceptor (Fenchel et al., 1998) according to (Lizama et al., 2002):

$$2S^0 + 3O_2 + 2H_2O \rightarrow 2H_2SO_4 \quad [4.1]$$

The rate of reaction [1] is also controlled by available surface area, temperature, and time (Janzen, 1984). In general, reaction rates increase with microbial activity, O_2 and nutrient availability, available surface area (Laishley et al., 1986), and temperature. Partially saturated conditions facilitate optimal reaction rates as water is available for reaction [1], yet the ingress of O_2 is not limited (Attoe and Olson, 1966; Janzen and Bettany, 1987b). Temperature increases S^0 oxidation rates according to the Arrhenius equation, with oxidation rates being limited below 5°C (Janzen and Bettany, 1987b; Lizama et al., 2002). Temperatures below 5°C also limit the activity of naturally-occurring autotrophic S^0 oxidizers (e.g., *Acidithiobacilli*) that function optimally at pH values less than 3 (Johnson, 1998).

While much can be learned from existing studies, understanding the oxidation of S^0 in commercial-scale blocks is a unique challenge because S^0 blocks are unsaturated, highly fractured, and mostly hydrophobic (Birkham et al., 2009). Sulphur blocks fracture as a result of the 12.5% total volume shrinkage (Meyer, 1977) that occurs after pouring due to both solidification/freezing (temperatures <115°C; 7% volume reduction) and a mineral change from monoclinic to rhombic crystal structure over several days at temperatures <95°C (5.5% volume reduction). The volume reduction results in extensive vertical and horizontal fractures (Bonstrom et al., 2009) that act as preferential pathways for water infiltration (Birkham et al., 2009) and gas transport (Birkham et al., 2010). Preferential water infiltration along fractures is enhanced by the hydrophobic nature of the matrix (unfractured) S^0 (Knickerbocker et al., 2000), which requires positive water pressure heads of 1-2 m for water to begin to enter matrix pore spaces (Bonstrom et al., 2009). Hydrophilic conditions may develop, however, in areas of microbial colonization on fracture faces (Birkham et al., 2009). In the case of S^0 blocks, reactions may be limited to the vertical and horizontal fracture surfaces that are evident on the surface of the blocks.

The objectives of the current study were to: (1) quantify the present-day rates and controls on S^0 oxidation in an above-ground block; (2) define the distribution of H_2SO_4

production in S^0 blocks; and (3) make recommendations to control or reduce rates of oxidation at two commercial-scale above-ground S^0 blocks. S^0 oxidation rates were estimated by modelling *in situ* O_2 concentration [O_2] and temperature distributions. These estimates were compared with oxidation rates measured in lab reaction cells, H_2SO_4 loading in drainage water from a S^0 block, and *in situ* relative humidity measurements. The findings of this study are applicable to S^0 blocks at other locations as most S^0 blocks are constructed with similar methods and therefore have similar geo-mechanical and geo-environmental properties (Syncrude Canada Ltd., 2004a; personal communication, Paul Davis, Alberta Sulphur Research Ltd).

4.3 Materials and methods

4.3.1 Field site

The two commercial-scale S^0 blocks studied were located at the Syncrude Canada Ltd. oilsands mine in northern Alberta, Canada (57°02'34.89"N, 111°38'36.14"W). The Phase 1 block was constructed between 1994 and 2004, is 359 m long and 168 m wide (area at base of 60,312 m^2) (Syncrude Canada Ltd. 2004b), and contains an estimated 946,000 m^3 of S^0. The maximum height of this block is 17.5 m at TM03-07 (Figure 4.1). The Phase 2 block was constructed approximately 100 m west of the Phase 1 block between 1997 and 2005. It is 261 m long and 334 m wide (area at base of 87,174 m^2) (Syncrude Canada Ltd., 2004b), has a height of 25 m, and an estimated volume of approximately 2,000,000 m^3. Both blocks were constructed using the same method whereby molten S^0 is poured from three towers into two areas on both sides of the towers (east and west directions). The extent of the molten S^0 flow is constrained by aluminum forms. After the S^0 reached the desired final height, the pouring towers were dismantled and S^0 was poured into the passageway between the east and west blocks.

Bonstrom (2007) described the density, fracture porosity (n_f), matrix porosity (n_m), fracture aperture and distribution, and saturated hydraulic conductivity (K_s) of the Phase 1 S^0 block. The density of intact core samples averaged 1880 $kg \cdot m^{-3}$ (n = 280, s.d. = 700 $kg \cdot m^{-3}$) and did not exhibit an increasing or decreasing trend with depth. The mean n_m of these samples was 9.3% (n = 280, s.d. = 3.4 %) assuming a specific gravity

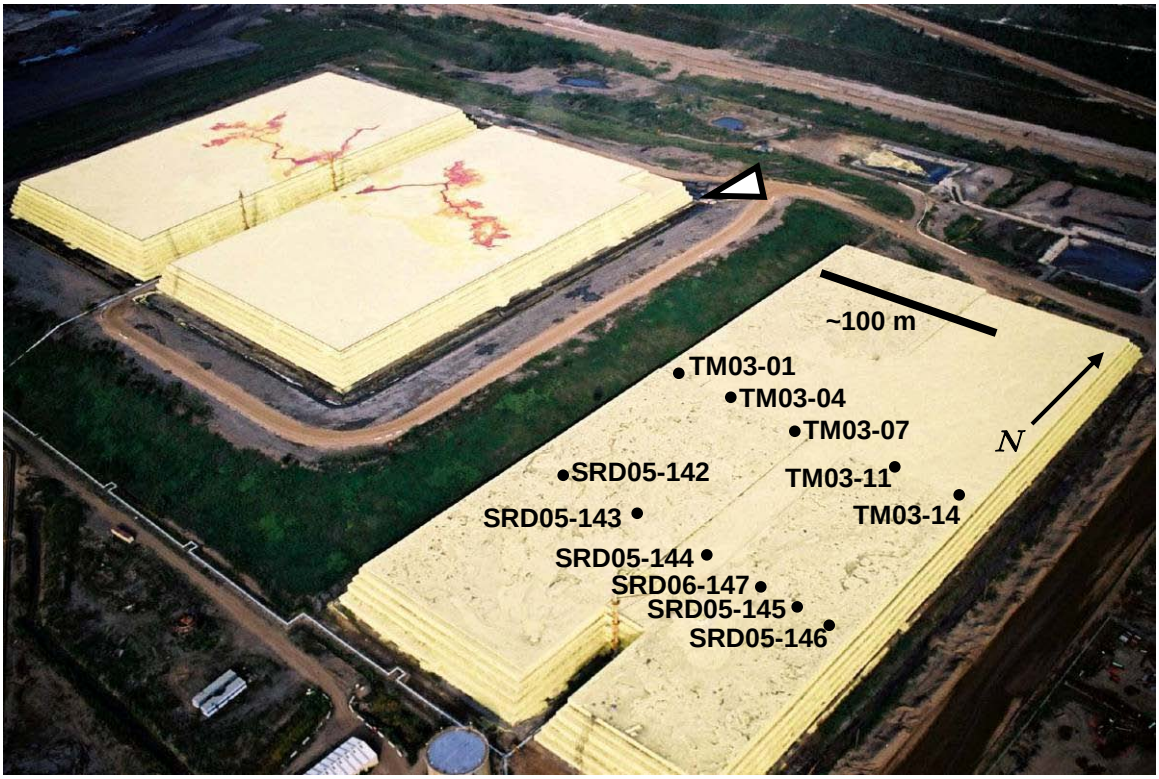

Figure 4.1. Aerial photo of Phase 1 (lower right) and 2 (upper left, under construction) S^0 blocks at Syncrude Canada Ltd. oil sands mine in 2003. Black dots on the Phase 1 block represent locations of vertically-nested gas sampling ports (SRD series) and thermistors (TM series). The white triangle at the north-east corner of the Phase 2 block represents the location of the weir and drainage sampling location. The dark texturing on the surface of the Phase 1 block is wind-blown sediment. Dark orange flow channels on the Phase 2 block are molten S^0. The passageway for the Phase 2 pouring towers divides the block in a north-south direction, while the passageway for the Phase 1 pouring towers has been filled except for a small section at the south end of the block.

of 2070 $kg \cdot m^{-3}$. The mean effective (interconnected) n_m was determined to be 6.5%. The mean aperture of vertical fractures was 1.2 mm and the mean aperture of horizontal fractures was 1.0 mm (only apertures >0.6 mm were measured). The fracture orientation was determined to be random and the mean vertical and horizontal fracture frequencies were 33.5 and 5.4 m^{-1}, respectively. The n_f was estimated at 1.4%.

Mean annual precipitation (water equivalent) at Fort McMurray (40 km south of S^0 blocks) is 455.5 mm, with 342.2 mm as rainfall and the remainder as snow (annual data from 1971-2000; Environment Canada, 2009a). Mean annual temperature is 0.7°C, with the lowest monthly mean in January (-18.8°C) and the highest in July (16.8°C).

4.3.2 Drainage outflow rates

Hourly outflow rates at the Phase 2 block were measured in 2006 using a V-notch weir (Figure 4.1) as described by Birkham et al. (2009). The water equivalent of the snowpack on the Phase 1 block was estimated from the results of a snow survey on 13 March 2006. Snow depths at 57 locations (along two north-south transects across the entire surface) were measured with a steel ruler. Snow pack density was measured at eight random locations by measuring the snow depth and collecting a core sample of the snow by pushing a plastic tube (inner diameter 18.5 mm) into the snowpack. The snow samples were transferred to sealed plastic bags and weighed later the same day. The snow water equivalent for the Phase 1 block was estimated by multiplying the average snow density and the estimated volume of snow on the Phase 1 block.

4.3.3 pH and SO_4 concentrations of drainage water

Drainage water samples (n=33) from the Phase 2 S^0 block were collected from 24 April to 9 October 2006 with an automated ISCO® water sampler in 1 L plastic bottles for pH and SO_4 concentration [SO_4] measurements. The mean sampling interval was 6 days and ranged from 1-50 days. Although the plastic bottles in the automated water sampler were left uncapped for up to two months (within an enclosed container), and the time between sample collection and pH and [SO_4] measurements was as great as three months (samples were stored in refrigerated, sealed 1 L plastic bottles), the delay in measurement had a minimal effect on pH. Analyses on selected samples at elapsed times of 1 h to 90 d between sample collection and pH measurement show the pH change was within the measurement error (±0.3 pH units, see below) (data not presented).

pH was measured using a Thermo Orion® 250A pH meter and a mV calibration (for dilute H_2SO_4 solutions with pH of -0.27, 1.0 and 2.0). The pH of each field sample (±0.3 pH units) was determined by measuring the mV of the sample and linearly interpolating a pH value from the calibration data. [SO_4] was measured on samples using a Dionex® ion chromatograph. Accuracy of [SO_4] analysis (including dilutions up to 500× and chromatograph error) was ±10%.

4.3.4 *In situ* relative humidity distribution

Relative humidity (RH) and temperature were measured in gas samples collected within the Phase 1 S^0 block on 16 May 2007 at SRD05-142, SRD05-143, and SRD05-144 (Figure 4.1). Samples were collected from vertically nested gas sampling ports (CMT channels, installation details described below) after purging 100 mL of gas for every meter of channel using a 140-mL syringe fitted with a three-way luer-lock valve. After the sample was collected, the 140-mL syringe was connected to a 60-mL syringe (plunger removed). After approximately 100 mL of gas was flushed through the 60-mL syringe, a Digi-Sense® RH meter probe (16.4-mm diameter) was slowly inserted. The syringe was sealed by fitting the rubber portion of the 60-mL syringe plunger around the RH probe. Care was taken to continually flush the sample through the 60-mL syringe as the RH probe was being fitted to avoid atmospheric contamination. Once the RH probe was sealed in the syringe, flushing of the sample from the 140-mL syringe was stopped to avoid pressurizing the sample and thereby increasing the RH. The syringes were kept in the shade during sampling and RH measurements to minimize temperature fluctuations. Temperature, RH, and calculated dew point were recorded once the temperature of the sample had stabilized.

The RH meter contained a capacitive sensor to measure RH over a range of 0 to 100% with an accuracy of ±2% between 10 and 90%, and ±4% between 0-10 and 90-100% RH. Temperature was measured with a thermistor element over a range of -40 to 60°C with an accuracy of ±0.2%. The RH factory calibration was verified using RH standards at 11.5 and 100% RH with a LiCl saturated salt solution and distilled water, respectively (Weast and Astle, 1981).

Water vapour concentrations were calculated using:

$$P_{act} = RH \times P_{sat} \qquad [4.2]$$

where P_{act} is actual water vapour pressure ($M \cdot L^{-1} \cdot T^{-2}$), and P_{sat} is saturated water vapour pressure. Saturated water vapour pressure in Eq.[4.2] were calculated using (Wagner and Pruss, 2002):

$$P_{sat} = P_{crit} \exp((\frac{T}{T_C}) fn(T)) \qquad [4.3a]$$

where P_{crit} is pressure at the critical point for water (22.064 MPa), T is the temperature at the sampling depth in Kelvin, and T_C is the temperature at the critical point for water (647.096 K). The term *fn(T)* is a temperature dependent function defined as (Wagner and Pruss, 2002):

$$fn(T) = a_1\upsilon + a_2\upsilon^{1.5} + a_3\upsilon^3 + a_4\upsilon^{3.5} + a_5\upsilon^4 + a_6\upsilon^{7.5} \quad [4.3b]$$

where a_1 = -7.8951783, a_2 = 1.84408259, a_3 = -11.7866497, a_4 = 22.6807411, a_5 = -15.9618719, a_6 = 1.80122502, and $\upsilon = 1-\frac{T}{T_C}$.

Temperature data at TM03-01, -04, and -07 (Figure 4.1) were used to estimate P_{sat} within the block with Eq.[4.3a] and [3b] at SRD05-142, -143, and -144, respectively. Temperature data for 16 May 2005 or 2006 were used when data were not available for 16 May 2007 (date of RH measurements). This was a reasonable approximation given the consistent seasonal patterns at depths above 5.5 m, and the relatively unchanging temperature at or below 5.5 m. *In situ* RH was then calculated by dividing the estimated P_{act} (from measured RH and temperature in 60-mL syringes as described above) by the estimated *in situ* P_{sat}. The error in calculated *in situ* RH was estimated to be ±3-5% (actual RH value, not a percentage of RH) for an error in *in situ* temperature of ±1°C, and approximately ±20% for a temperature error of ±4°C.

4.3.5 Reaction cells containing liquid water

Rates of O_2 consumption and CO_2 production (per unit surface area; α_{O2} and α_{CO2}) were measured for samples of S^0 in contact with liquid water by placing approximately 20 g of pure (>99.9%) S^0 (particles of 11-12 mm diameter; collected at the mine site) into autoclaved 100-mL glass serum bottles. Ten mL of drainage water collected from the Phase 2 S^0 block on 18 September 2006 was placed in each serum bottle (reaction cell) to act as an inoculant, with the exception of the control samples to which sterile (autoclaved) de-ionized water was added. The number of reaction cells per experiment, temperature, initial gas headspace concentrations, and water type are presented in Table 4.1. A water volume of 10 mL was used so that each S^0 particle was in contact with the water, but not saturated. The bottles were crimp sealed with 5 mm thick butyl blue septa.

Table 4.1. Details of S^0 reaction cell experiments containing liquid water.

Temp. (°C)	Initial gas composition	Water type	Number of experiments	mean α_{O2} (mol O_2 $m^{-2}\cdot d^{-1}$)	s.d. α_{O2} (mol O_2 $m^{-2}\cdot d^{-1}$)
23	Air[1]	Drainage	11	4.2×10^{-3}	1.2×10^{-3}
23	Cylinder[2]	Drainage	13	na[3]	----------
23	Air	Drainage (no S^0)	3	--[4]	--[4]
23	Air	Sterile de-ionized	3	3.7×10^{-5}	1.3×10^{-5}
10	Air	Drainage	4	1.3×10^{-3}	2.6×10^{-4}
10	Cylinder	Drainage	8	na[3]	----------
2.9	Air	Drainage	5	2.8×10^{-4}	1.5×10^{-5}
2.9	Cylinder	Drainage	8	na[3]	----------

[1] 20.9% O_2, ~0.04 % CO_2, 78.1 % N_2
[2] 3 % O_2, 10 % CO_2, 87 % N_2
[3] Not available; low initial [O_2] (3%) made α_{O2} measurements inconsistent
[4] αO_2 (per surface area) not measured because no S^0 particles were used; mean β_{O2} was 3.1×10^{-7} mol O_2 d^{-1} (s.d.=1.9×10^{-7} mol O_2 d^{-1})

Reaction cells with initial gas headspace concentrations of atmospheric air (20.9% O_2, ~0.04% CO_2, and 78.1% N_2) were used to measure α_{O2}. Reaction cells with initial gas headspace concentration of 3% O_2, 10% CO_2, and 87% N_2 were used to measure the α_{CO2}; these reaction cells were flushed with ~400 mL of the 3% O_2/10% CO_2 mixture by puncturing the reaction cell septa with one needle connected to the compressed gas cylinder and a second needle vented to the atmosphere. After flushing the reaction cells with the gas mixture (duration of approximately 60 s), the needles were removed from the septa. Reaction cells with both of the initial gas headspace compositions were maintained at 23, 10, and 3°C (±1°C).

The headspace gas sampling frequency and duration of these experiments varied depending on the temperature. Reaction cells at 23°C were sampled two to five times over a 14 d period while reaction cells at 3°C were sampled three to four times over a 114 d period. Samples were collected in 10-mL syringes with three-way luer lock valves. For gas headspace sampling, a needle connected to a 10-mL syringe via a three-way valve was inserted into the reaction cell through the septa. If a low [O_2] was expected, or if the initial headspace was 3% O_2/10% CO_2, the syringe and sampling

needle were pre-flushed immediately before sampling with 100% N_2 or 3% O_2/10% CO_2, respectively, to minimize atmospheric contamination. Immediately upon needle penetration through the septum, 3 mL of gas was withdrawn into the syringe and expelled to the atmosphere (using the three-way valve and keeping the cell headspace isolated from the atmosphere), after which 7 mL of gas was withdrawn from the cell and sealed in the syringe. The gas sample was immediately analyzed for [O_2], [N_2], and [CO_2] by manual injection into an Agilent Micro (M200) gas chromatograph (GC) equipped with a thermal conductivity detector and 8-m columns packed with a 0.5-nm molecular sieve for separation of O_2 and N_2, and Poraplot for separation of CO_2. Carrier gases were argon for the O_2/N_2 column and helium for the CO_2 column. Standards of atmospheric air (78.1% N_2 and 20.9% O_2), 100% N_2, and calibration mixtures (10% O_2/1.58% CO_2 and 3% O_2/10% CO_2) were analyzed before and after each round of sampling. The lower detection limits for [O_2] and [CO_2] were 0.1 and 0.05%, respectively.

The reactive S^0 surface area in the reaction cells was estimated assuming the particles were spherical (average diameter of 11.5 mm) and that no oxidation occurred in the internal porosity because of the absence of water due to hydrophobicity. α_{O2} calculations were corrected for gas volume removed during sampling by subtracting the sampling volume from gas volume present in the headspace before sampling. The reaction cells were confirmed to be gas tight by filling five empty crimp-sealed serum bottles with 100% N_2 and measuring negligible decrease in [N_2] after a 114 d test period (data not presented).

4.3.6 Microbiological analyses

To confirm the presence of heterotrophic and autotrophic S^0-oxidizing microorganisms in the reaction cells, most probable numbers (MPN) in water samples from the reaction cells were quantified following the protocol described in Lawrence et al. (1988a). In brief, heterotrophic S^0 oxidizers were detected with a five tube dilution series (n=18) in heterotrophic S^0 medium (HSM) (0.1% peptone, 0.05% yeast extract, 0.003% Bromophenol Blue, pH 6.8, 0.002% 2X water rinsed and pre-autoclaved flowable sulphur (Stoller Chemicals, Burlington, ON) added after autoclaving).

Autotrophic S^0 oxidizing microorganisms were enumerated (n=17) using the MPN technique and ATCC #125 medium (1.0 L of water: 0.2 g (NH)SO, 0.5 g $MgSO_4$. $7H_2O$, 0.25 g $CaCl_2$, 5.0 mg $FeSO_4$, 5 mL of 0.22 μm filter sterilized KH_2PO_4 solution at 0.3 g mL^{-1}, and 1 mL of filter sterilized Bromocresol green solution at 0.015 g·mL^{-1} for color indication of pH). The media for thiosulfate oxidizers had 5 mL of sterilized $(NH_4)_2S_2O_3$ solution (0.5 g mL^{-1}) added after autoclaving; the media for S^0 oxidizing autotrophs had 0.002% of 2× washed sterilized flowable S^0 added. Plates were incubated at 23°C for up to 12 weeks to detect growth as indicated by a decrease in pH of the media.

4.3.7 Water vapour reaction cells

α_{O2} and α_{CO2} for S^0 particles exposed to only water vapour were measured by placing air-dried S^0 in sealed 790-mL PVC cells (n=6) containing saturated KCl solutions to ensure water vapour was relatively abundant (RH=85%; Carotenuto and Dell'Isola, 1996) while preventing condensation on the S^0 pieces. The saturated KCl solution in the cells was open to the gas headspace but did not contact the S^0 particles directly. The reaction cells were gas tight, with threaded lids (with rubber O-ring) fitted with gas-tight, three-way sampling valves.

Two reaction cells contained one large piece of S^0 collected from the surface of the Phase 1 S^0 block (approximately 400 g each); two reaction cells contained the S^0 particles used in the free-water reaction cells; one reaction cell contained 'fresh' S^0 particles (never exposed to field conditions); and one cell contained only a saturated KCl solution. S^0 particles were submerged in Phase 2 block drainage water for 5 d to inoculate them with naturally occurring bacteria. The S^0 pieces were subsequently air-dried for 2 d prior to testing. The surface area of the large S^0 pieces was estimated by measuring the dimensions of each fracture face on the S^0 piece with a digital caliper, and assuming the fracture face to be either rectangular or triangular. The S^0 pieces were isolated from the KCl solution by placing a thin, finely perforated piece of plastic over the KCl container, on which the plastic S^0 container was placed. The equilibrium RH of the KCl solution was also measured at 85% to confirm the values reported in the

literature. This measurement was made by sealing an RH probe (described above) in a glass vial containing a saturated KCl solution.

The cells were maintained at room temperature (23°C) and sampled after 11, 23, and 67 d for [O_2], [CO_2], and [N_2]. Samples were collected in 10-mL syringes fitted with three-way sampling valves. Immediately after attaching the syringe to the reaction cell sampling valve and opening the sampling valve, 3 mL of gas was withdrawn from each cell and flushed to the atmosphere to minimize atmospheric contamination. Subsequently, a 10-mL sample was collected in the syringe and analyzed for [O_2], [CO_2], and [N_2] as described for the reaction cells containing liquid water.

4.3.8 *In situ* temperature distribution

Temperature profiles were measured in the Phase 1 block using vertically nested thermistors installed September 2003 at TM03-01 (depths of 0.4, 1.4, 3.4, 5.4, 7.4, 9.4, 11.4, and 13.1(×2) m), TM03-04 (depths of 0.5, 1.5, 3.5, 5.5, 7.5, 9.5, 11.5, 13.5, and 13.8 m), TM03-07 (0.5, 1.5, 3.5, 5.5, 7.5, 9.5, 11.5, 13.5, 16.5, and 18.5 m), TM03-11 (depths of 0.3, 1.3, 3.3, 5.3, 7.3, 9.3, 11.3, 13.3, and 13.6 m), and TM03-14 (depths of 0.4, 1.4, 3.4, 5.4, 7.4, 9.4, 11.4, and 12.75(×2) m) (Figure 4.1). Temperatures were measured and logged once daily on Data Dolphin® dataloggers. As several of the thermistors malfunctioned in late 2005, spurious temperature values (i.e., values that changed by >10^{o}C over a short time period) were deleted from the data set and are not presented.

4.3.9 *In situ* [O_2], [N_2], and [CO_2]

Vertically nested gas sampling ports along the SRD05/SRD06 transect on the Phase 1 block (Figure 4.1) were installed to measure [N_2], [O_2], and [CO_2] profiles at depths of 1-15 m for the SRD05 series and 0.5-6 m for the SRD06 profile. Continuous multi-channel tubing (CMT; Solinst®) was used in all SRD05 instrumentation while conventional gas ports were installed at SRD06-147. The SRD05 CMTs (Figure 4.1) were installed in 15.3-cm diameter boreholes drilled using solid-stem augers. The CMTs contained seven discrete sample channels within a 4.3-cm OD tube, with one sampling port (area ~100 mm^2) constructed in each channel. Sampling ports were spaced along the

CMT at approximately 2-m intervals, with one sampling port for each CMT channel. The CMT was lowered down the borehole and the annular space around each sampling port backfilled with filter sand (particle diameter of 0.5 to 1 mm) with the annular space between each sand interval backfilled with bentonite chips in approximately 0.3-m lifts (1 m total thickness). The 1-m intake zone for each sampling port was chosen to ensure the sand backfill (and the gas intake zone) intersected the horizontal fractures. Two L of water was poured on top of every 0.3-m bentonite lift to hydrate the bentonite chips and thus create a barrier to gas migration along the annular space between sampling ports. The top of each CMT channel was fitted with a flow-through sampling valve and a three-way valve with luer lock connections for fastening to syringes during sampling.

The gas sampling installation at SRD06-147 was constructed using 6.35-mm OD polyethylene tubing with screened filters fitted across the down-hole end of the tubing. The gas probes were attached to a 12.7-mm diameter (OD) PVC pipe (with sealed ends) at the desired sampling points. The PVC pipe with attached gas ports was then lowered down the borehole. The gas ports at SRD06-147 were located at 0.5, 1, 2, 3, 5, and 6 m below the surface. The backfilling method used for these probes was the same as for the CMT installations, except thinner bentonite seals (0.25-0.5 m) were used between the sampling ports.

In situ $[O_2]$, $[N_2]$, and $[CO_2]$ were measured on 9 December 2005, and 11 March, 17 May, and 12 September 2006. In each sampling campaign, gas samples were collected in 140-mL syringes after sufficient gas (e.g., 100-mL per meter of CMT channel) was purged from the sample tubing or channel to ensure gas from the appropriate depth was being sampled. Samples were analyzed on site within 3 h of collection using the analytical procedure and calibration standards described for the reaction cell experiments above.

4.3.10 $[O_2]$ distribution modelling

$[O_2]$ distributions in the Phase 1 block were modelled to estimate the location and rates (per unit volume, β_{O2}) of O_2 consumption. The aim of the modelling was to simulate general trends in the $[O_2]$ distribution, rather than exactly match the modelled and measured $[O_2]$ contours. The modelled β_{O2} were used as an estimate of H_2SO_4

production rates according to the stoichiometry in Eq. [4.1]. The 2-D modelling was performed using the Geostudio® 2007 numerical modelling suite, which included coupled models for advective gas flow (SEEP/W®) as well as gas consumption rates and diffusive fluxes (CTRAN/W®). Birkham et al. (2010) used this same approach to model steady-state late-summer [N_2], [O_2], and [CO_2] distributions in the Phase 1 block. To meet the objective of this paper, we focus on seasonal trends in [O_2] and controls on *in situ* [O_2].

Gas diffusion within the block was described by Fick's first law:

$$J_i = -\theta_a \omega D_{air} \frac{dC_i}{dz} \quad [4.4]$$

and transient gas diffusion was described by Fick's second law:

$$\theta_a \frac{\partial C_i}{\partial t} = \theta_a D_e \frac{\partial^2 C_i}{\partial x^2} + \beta \quad [4.5]$$

where J_i is the mass flux of species i ($M \cdot T^{-1}$); θ_a is the air-filled porosity; ω is the relative gas diffusivity (dimensionless; Moldrup et al., 200), which is greater than one and related to the tortuosity (τ) of the porous medium (ratio of gas particle path length to straight-line travel distance); C_i is the concentration of species i ($M \cdot L^{-3}$); z is the distance in the direction of the mass flux (L); and β is the gas consumption/production rate per unit volume ($M \cdot T^{-1} \cdot L^{-3}$). The D_{air} for O_2 was assumed to be 1.78×10^{-5} $m^2 \cdot s^{-1}$ (Weast and Astle, 1981). D_e is the effective diffusion coefficient ($L^2 \cdot T^{-1}$) as defined by:

$$D_e = \omega D_{air} \quad [4.6]$$

A steady-statefluid flow field was simulated in SEEP/W® with the governing equation:

$$\frac{\partial}{\partial x}\left(K_{a,x} \frac{\partial H}{\partial x} \right) + \frac{\partial}{\partial y}\left(K_{a,y} \frac{\partial H}{\partial y} \right) + F = 0 \quad [4.7]$$

where K_a is the air permeability ($L \cdot T^{-1}$) in the x and y directions, H is total head (L), and F is an applied flux (T^{-1}).

The fluid flow field and reaction/transport models were coupled in that the volumetric fluxes (F in Eq. [4.7]) used to simulate a steady-state flow field were equivalent to β (in Eq. [4.5]) within the S^0 block. Modelling of [N_2] and [CO_2] was conducted to ensure parameters applied in the [O_2] modelling resulted in reasonable

modelled [N_2] and [CO_2] distributions (Birkham et al., 2010). An equivalent porous medium (EPM) was assumed to represent the fractured S^0 blocks. Birkham et al. (2010) estimated the EPM θ_a and ω of the Phase 1 block to be 6.7% and 0.13, respectively, for depths from 8-17 m, and as great as 9.4% and 0.44, respectively, in the upper 8 m.

As the measured [O_2] distribution in the western and eastern halves of the Phase 1 block (presented below) were similar, symmetry was assumed and further modelling focused on the western half of the block. The western side of the 2-D model grid was an atmospheric boundary, and the eastern side coincided with the location of the pouring towers (during block construction). The western side and top boundary of the model grid were set to a constant atmospheric [O_2] (20.9%). The eastern side and bottom boundary were no flux boundaries. A nodal spacing of 0.5 m was used for the model grid, except within 1 m of the top and western boundaries where a nodal spacing of 0.125 m was used. The 2-D model grid was 92.9 m wide and 17.4 m high.

Winter [O_2] cross sections were modelled using the steady-state summer [O_2] as initial conditions and varying the β_{O2} within the block to correlate with *in situ* winter temperatures. A surficial layer (0.05 m thickness) with relatively low EPM θ_a and ω was added to the winter model to simulate a surficial ice/snow layer (discussed below).

4.3.11 Temperature distribution modelling

Temperature distributions in the Phase 1 block were modelled using the Geo-studio® (TEMP/W®) numerical model assuming heat transfer by conduction (no advection) and no effect of winter freezing on thermal conductivity. As S^0 oxidation (Eq. [4.1]) is an exothermic reaction with a free energy of -415 kJ·mol^{-1} oxidized S^0 (Lizama et al. 2002), the rate of heat generated in the S^0 block is directly proportional to the β_{O2} estimated from the [O_2] modelling. Rates of heat generation (G) were estimated by converting the modelled β_{O2} values to a S^0 oxidation rate (using Eq. [4.1]) and multiplying by 415 kJ·mol^{-1} S^0. The thermal modelling was used to verify if modelled β_{O2} were reasonable as well as to assess the importance of S^0 oxidation in controlling temperatures within the block.

A 2D modelling grid (17.4 m high × 84 m wide) was used to represent half of the Phase 1 S^0 block (symmetry assumed) with the right boundary representing the middle

of the block and the top and left boundaries representing the atmospheric boundary. The width of the gas modelling grid was slightly greater than for the thermal modelling to correspond with locations of gas sampling ports. Initial temperatures were set to 11.1°C (mean block temperature below 5.5 m from Nov. 2004-May 2007; discussed below). Estimated G values in the block were varied spatially and temporally as determined from the $[O_2]$ modelling (discussed below). Daily average atmospheric temperatures measured in 2006 (measured by Environment Canada, 2009b, Mildred Lake station) were assigned to the left and top boundaries, and designated as a cyclic boundary condition in multi-year simulations. The bottom boundary was set at a constant temperature (7.8°C) equal to the average temperature measured under the S^0 block (data not presented). The S^0 was assigned a thermal conductivity of 0.269 $J \cdot m^{-1} \cdot s^{-1} \cdot °C^{-1}$, a heat capacity of 1420 $kJ \cdot m^{-3} \cdot °C^{-1}$ (Lide, 2003), and a uniform moisture content of 0.6%. The simulation duration was 5-10 y (timesteps of 0.5 d) to allow consistent annual temperature trends to develop in the block.

4.4 Results and discussion

4.4.1 Environmental loading of H_2SO_4

Concentrations of SO_4 and pH of drainage water from the Phase 2 block ranged from 13-33 $g \cdot L^{-1}$ and 0.4-1.0, respectively (Figure 4.2). The greatest $[SO_4]$ and smallest pH values were measured from late May to early July. $[SO_4]$ decreased to <20 $g \cdot L^{-1}$ and pH increased to >0.65 proceeding heavy rainfall and high drainage outflow rates in mid-July. Measured pH and $[SO_4]$ matched theoretical values calculated using the computer program PHRQPITZ, which uses the Pitzer method and the MacInnes convention for scaling individual ion activity coefficients (Plummer et al., 1988). For example, theoretical pH from 0.45-0.83 corresponded to $[SO_4]$ from 15-35 $g \cdot L^{-1}$, which are similar to measured values. This validated the analytical methods used for measuring pH and $[SO_4]$, and suggested the acidity in the S^0 block drainage was from H_2SO_4.

The cumulative mass of SO_4 in drainage from the Phase 2 block was estimated to be 4.6×10^5 kg (1.5×10^5 kg S^0) between 24 March and 2 November 2006 (Figure 4.3). Daily loadings of $[SO_4]$ were estimated by multiplying the measured daily flow volume by the $[SO_4]$. On days not measured, $[SO_4]$ was estimated by linear interpolation. SO_4

loading from 24 March to 2 November 2006 from the Phase 1 block was estimated at 3.1×10^5 kg (1×10^5 kg S^0) by scaling the Phase 2 loading by 0.67 (the ratio of Phase 1 to

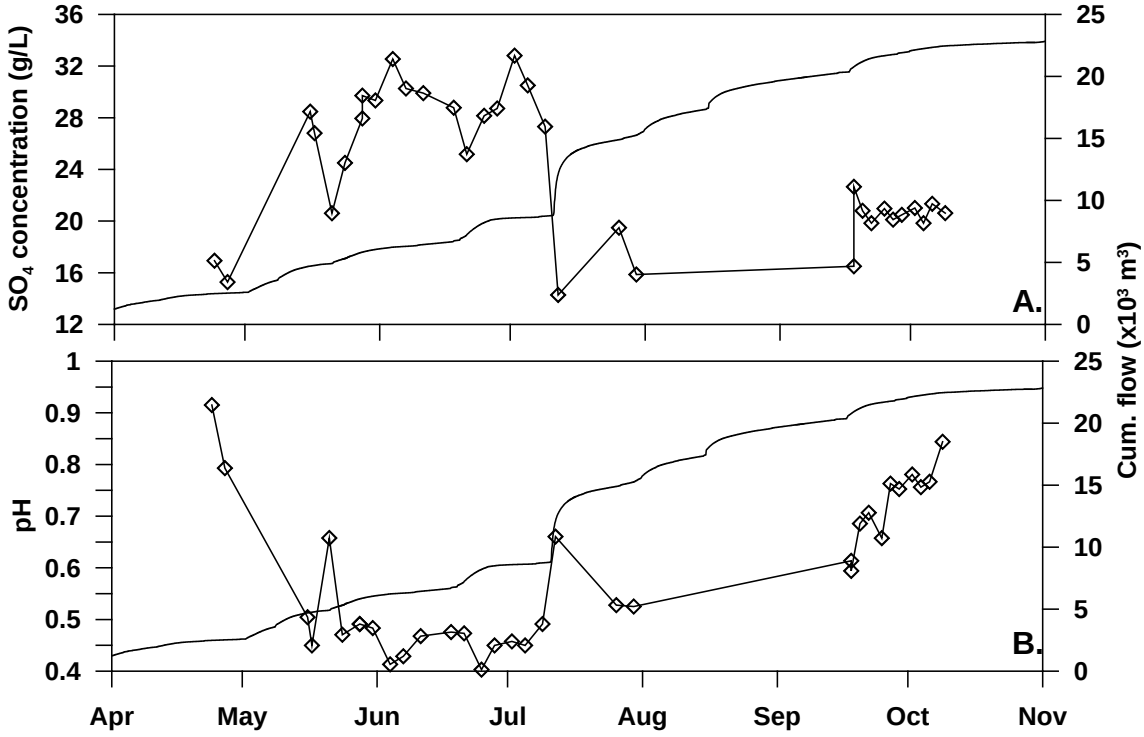

Figure 4.2. [SO_4] (A.) and pH (B.) (symbols), and cumulative flow volumes (line) of drainage water from the Phase 2 S^0 block for the 2006 field season.

Phase 2 footprint areas). Drainage was observed in late winter and early spring (during snowmelt) when flow measurements were not being recorded due to snow and ice buildup at the weir. The SO_4 loading during this time was estimated to be 6.2×10^4 kg (2.1×10^4 kg S^0) assuming an [SO_4] of 20 g·L^{-1} and a drainage volume from snowmelt on the Phase 1 block of 3,100 m^3. The snowmelt water volume was estimated using a mean snow depth of 184 mm (n=57, s.d.=51 mm), and mean snow density of 280 kg·m^{-3} (n=8, s.d.=66 kg·m^{-3}). The total SO_4 loading estimate for 2006 from the Phase 1 block was 3.7×10^5 kg (1.2×10^5 kg S^0). Assuming the Phase 2 block had similar snowpack depth, the estimated 2006 SO_4 loading for the Phase 2 block was 5.5×10^5 kg (1.8×10^5 kg S^0).

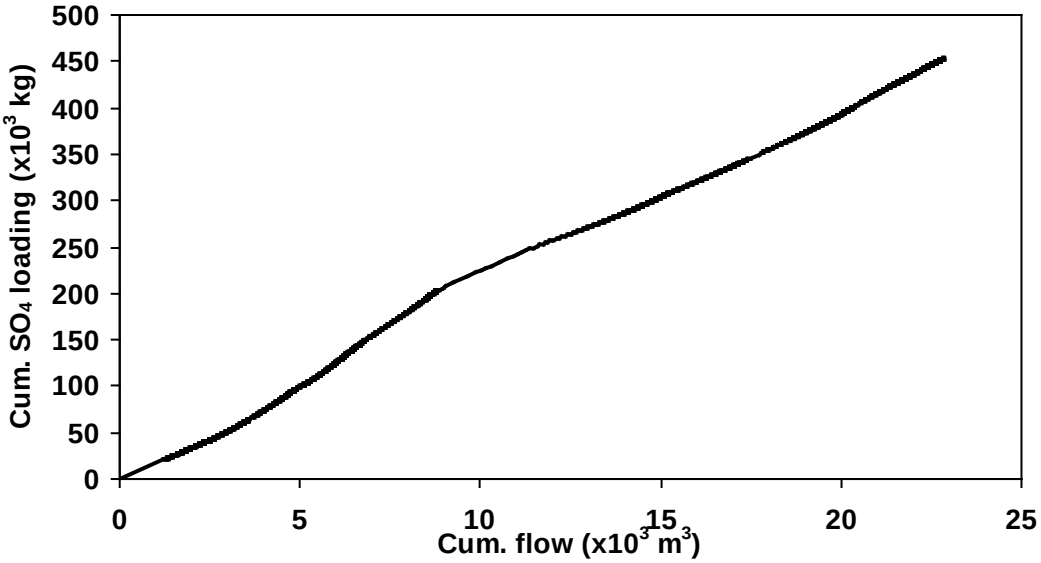

Figure 4.3. Cumulative SO_4 loading vs. cumulative outflow from the Phase 2 S^0 block from 1 April to 31 October 2006.

The cumulative SO_4 loading from the Phase 2 block increased linearly with cumulative outflow volume (Figure 4.3, R^2=1.00), suggesting the production and removal rates of SO_4 were approximately equal from late March to November of 2006. These data for a one-year time period were not sufficient to conclude if H_2SO_4 production rates had reached a long-term steady state as H_2SO_4 production rates may be gradually increasing with time (discussed below). To observe an increase in the slope of the cumulative SO_4 loading vs. outflow volume curve (i.e., generally increasing trend in outflow [SO_4], or decreasing trend in outflow pH), measurements of [SO_4] and outflow rates over many years may be required. Assuming H_2SO_4 in outflow waters resulted from partial mixing of infiltrating water (containing negligible H_2SO_4) and resident water in the S^0 block, [SO_4] would be greater (and pH less) *in situ* than in drainage water. This is discussed in greater detail below.

4.4.2 *In situ* relative humidity distribution

RH within the S^0 block ranged from 40-100%, with a mean of 68% (s.d.=17%, n=21; Figure 4.4). RH values less than 100% in unsaturated porous media can result from total suction (the sum of matric and osmotic suction) greater than 3,000 kPa (Fredlund and Rahardjo, 1993; Wilson et al., 1997). Matric suction values likely did not

exceed 3,000 kPa given that S^0 itself is hydrophobic and consequently has little capacity to exhibit capillarity, and that free-water is present at the bottom of the Phase 1 S^0 block (total depth of approximately 17 m; Birkham et al., 2009). Assuming the pore-water pressure profile to be at equilibrium with the free-water surface, matric suction values would not exceed 170 kPa in the S^0 block. For comparison, Severinghaus et al. (1996) concluded RH in 100-m thick unsaturated sand dunes in an arid environment was at 100% at depths as shallow as 0.2 m. Based on these data, RH values <100% were attributed to osmotic suctions resulting from concentrations of dissolved solids (i.e., H_2SO_4) within the block.

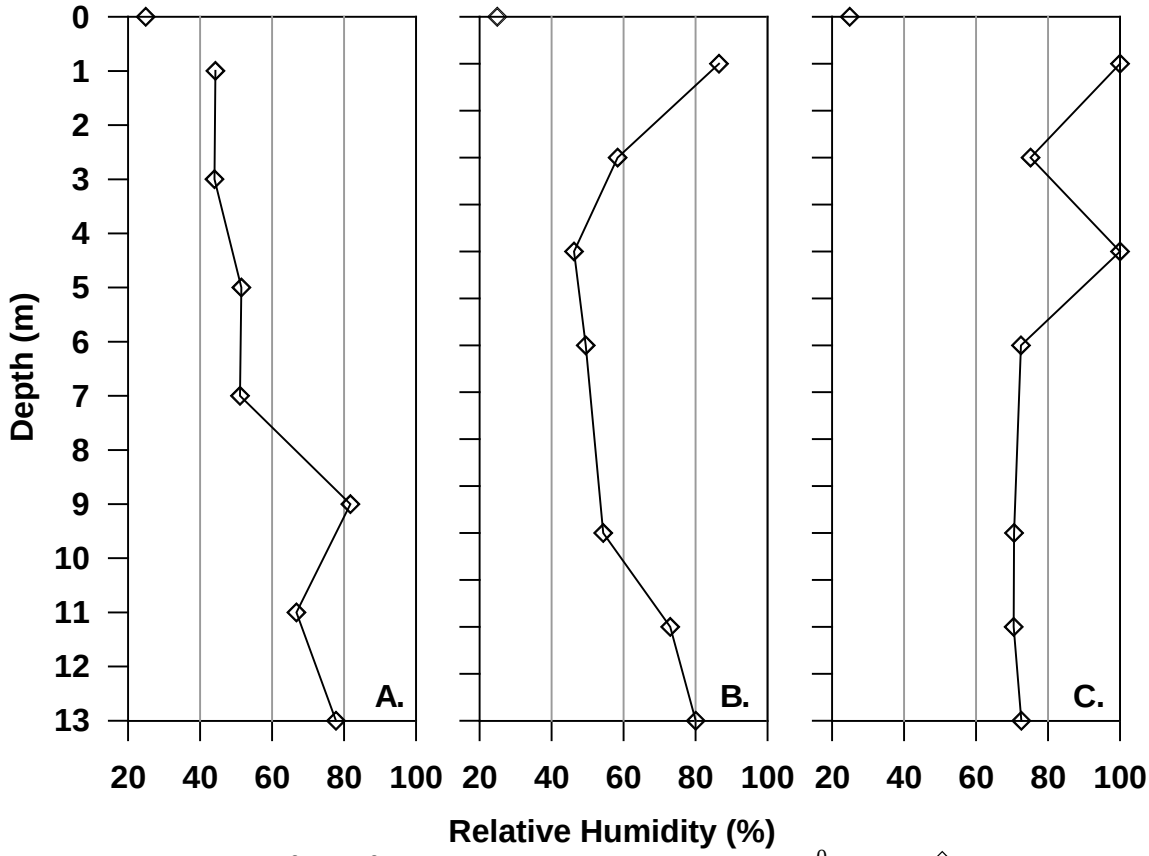

Figure 4.4. Depth profiles of relative humidity in the Phase 1 S^0 block at SRD05-142B (A), SRD05-143B (B), and SRD-144B (C). Atmospheric RH is presented at depth of 0 m.

RH values of 40% (lowest measured *in situ* RH) and 68% (mean measured *in situ* RH) corresponded to H_2SO_4 concentrations (weight %) of 47.5% and 33.7%, respectively (Wilson, 1921). Using the PHRQPITZ program, pH values of -3.8 and -2.1

were calculated for H_2SO_4 concentrations of 47.5 and 33.7%, respectively. Although additional testing is required, these data suggest *in situ* pH values at least for some areas in the Phase 1 S^0 block (S^0 oxidation sites on fracture faces and areas of friable S^0, Birkham et al. 2009) were considerably lower than the pH of the drainage water, and that the H_2SO_4 in the drainage waters was the result of mixing of resident (lower pH) water in the S^0 block with fresher (higher pH) infiltrating water. Assuming a simple mixing model whereby infiltrating water ($[SO_4]$=0) mixes with *in situ* water (average $[SO_4]$=390 $g \cdot L^{-1}$, equivalent to pH=-2.1) to produce drainage water from the blocks with $[SO_4]$=15 to 32 $g \cdot L^{-1}$ (see Figure 4.2), resident water accounted for 4-8% of the drainage water, respectively. The effect of the low pH of resident water on microbial activity is discussed below.

RH of 100% at depths of 1 and 5 m at SRD05-144B corresponded to the increased moisture content measured at SRD05-144 at depths of 1.2 and 5 m (Birkham et al., 2009). However, the 100% RH measured at 1 m depth at SRD05-143 did not correlate with moisture content measured by Birkham et al. (2009) and was attributed to heterogeneity in the moisture distribution within the S^0 block; moisture content samples in Birkham et al. (2009) were collected from a borehole about 3 m away from the nested gas sampling ports used for the RH measurements.

4.4.3 Laboratory-measured reaction rates

The rate of $[O_2]$ decrease (Figure 4.5) in the reaction cells containing liquid water was relatively linear (R^2 from 0.89-0.94) with time indicating α_{O2} was independent of $[O_2]$. As a result, S^0 oxidation was considered to be a zero-order reaction with respect to $[O_2]$.

Values of α_{O2} determined from liquid-water reaction cells containing S^0 increased as a function of temperature from 2.8 mol $O_2 \cdot cm^{-2} \cdot d^{-1}$ (0.6 μg $S^0 \cdot cm^{-2} \cdot d^{-1}$) at 2.9°C to 42 mol O_2 $cm^{-2} \cdot d^{-1}$ (9 μg S^0 $cm^{-2} \cdot d^{-1}$) at 23°C (Table 1) and were well-described by the function:

$$\alpha_{O2} = \alpha_{ref} \exp k(T - T_{ref}) \qquad [4.8]$$

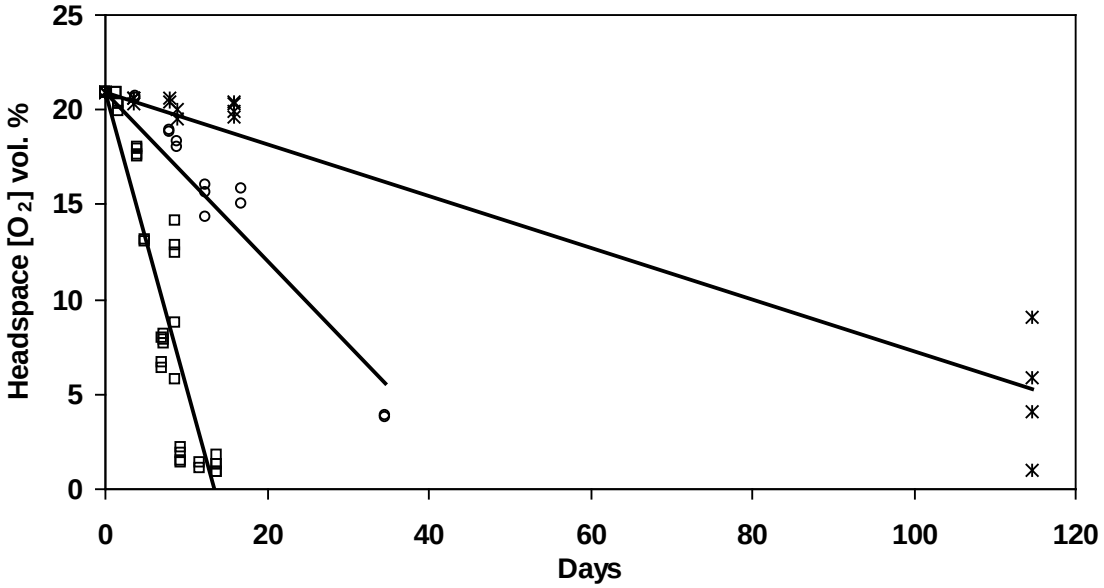

Figure 4.5. Headspace [O_2] in the sealed, free-water reaction cells for temperatures of 23°C (boxes), 10°C (circles), and 3°C (stars). Initial gas headspace was atmospheric ([O_2]=20.9 %). Lines represent best fit trendlines for each temperature series with R^2 values of 0.89 (23°C, boxes), 0.94 (10°C, circles) and 0.94 (2.9°C, stars).

where α_{ref} is the O_2 consumption rate ($M \cdot L^2 \cdot T^{-1}$) at a reference temperature, T_{ref} (3.9°C), and k is a fitting parameter (Figure 4.6).

The best-fit k value of 0.145 (Figure 4.6) was equivalent to a Q_{10}=4.3 (where Q_{10}=exp10k), which was within the range of Q_{10} values (3.2-4.3) estimated by Janzen and Bettany (1987b) for S^0 oxidation in soils, but greater than values reported in the literature for soil respiration (1.5-3.0; Hendry et al., 1999) and oxidation of pure S^0 samples (1.9-3.1; Chapman, 1989). High sensitivity of S^0 oxidation rates to temperature relative to soil respiration has been reported (Li and Caldwell, 1966; Nor and Tabatabai, 1977; Jaggi et al., 1999). α_{O2} values in the current study were similar to S^0 oxidation rates measured by Janzen and Bettany (1987b) at 23°C (4 to 16 μg S^0 $cm^{-2} \cdot d^{-1}$, with average values of ~5 μg S^0 $cm^{-2} \cdot d^{-1}$), but much less than rates measured by Jaggi et al. (1999) (50×10^3-100×10^3 μg S^0 $cm^{-2} \cdot d^{-1}$ at 24°C) and Laishley et al. (1986) (125-4900 μg S^0 $cm^{-2} \cdot d^{-1}$ at 28°C). These differences in α_{O2} were attributed to different microbial communities, S^0 crystalline structure, and reaction conditions as Jaggi et al. (1999)

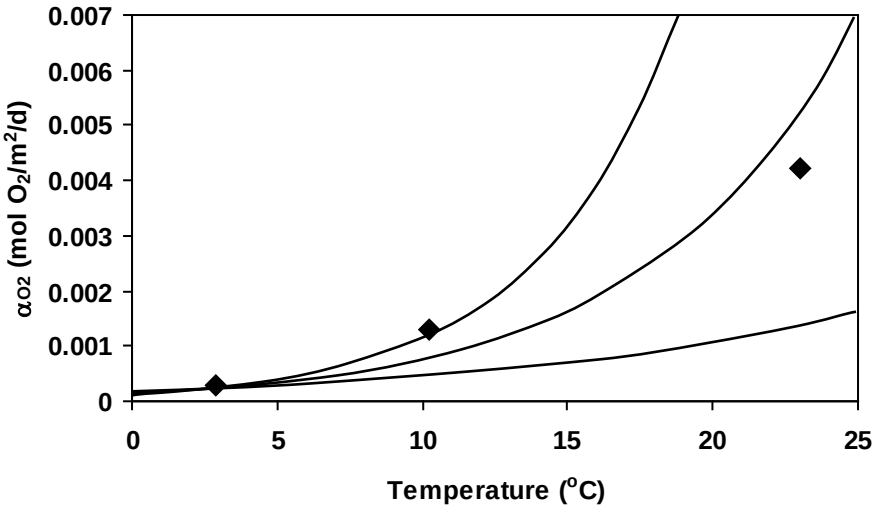

Figure 4.6. Sensitivity of α_{O2} to temperature. Solid lines are for k values (Eq.[4.8]) of (from greatest to least temperature sensitivity, left to right), 0.2, 0.145, and 0.08.

mixed S^0 with a sub-tropical soil and Laishley et al. (1986) mixed S^0 in synthetic salt solutions. Janzen and Bettany (1987b) mixed S^0 with soils from Saskatchewan, Canada, which has a similar climate to the Syncrude mine site and therefore may have had similar microbial communities.

The markedly lower but still measurable α_{O2} at 2.9°C in this current study was in agreement with the trend reported in the literature where S^0 oxidation rates are considered to decrease rapidly below 5°C. Low S^0 oxidation rates were measured at 5°C (Nor and Tabatabai, 1977) and 4°C (Li and Caldwell, 1966; Skiba and Wainwright, 1984), while Janzen and Bettany (1987b) reported negligible rates at 3°C. Chapman (1989) measured S^0 oxidation rates at 2°C, however the micronized S^0 (particle diameter 1-6 μm) used had a very high reactive surface area per unit mass.

Consumption of O_2 in the reaction cells via microbially-mediated S^0 oxidation was supported by the measurement of very low α_{O2} in reaction cells containing only drainage water (no S^0) or sterile de-ionized water with S^0. Mean β_{O2} in reaction cells containing only drainage water (3.1×10^{-7} mol O_2 d^{-1}; 23°C) was one order of magnitude less than β_{O2} in reaction cells with S^0 and drainage water at 2.9°C (data not presented). Similarly, mean α_{O2} in reaction cells with sterile de-ionized water added to S^0 was

approximately one order of magnitude less than reaction cells with drainage water and S^0 at a temperature of 2.9°C (Table 1).

Unfortunately, we were unable to estimate α_{CO2} in the reaction cells with initial atmospheric headspace concentrations because the [CO_2] in individual reaction cells did not consistently increase with time (data not shown). However, compared to changes in [O_2], changes in [CO_2] were small, with a mean [CO_2] of 0.19% (n=47, s.d.=0.19) within a range of <0.03 to 0.66%. The low ratio of α_{CO2} to α_{O2} (<0.05) suggests O_2 consumption by heterotrophic microbial activity in the reaction cells was minimal, as heterotrophic microbes associated with oxidation of soil organic carbon typically yield a molar ratio of CO_2 production to O_2 consumption from 0.5-0.77 (Drever, 1997; Lee et al., 2003; Birkham et al., 2007). These data suggest O_2 consumption in the reaction cells was due to autotrophic bacterial activity.

Most probable number analyses of drainage water used in the reaction cells showed both autotrophic and heterotrophic S^0 oxidizers were present. Populations of autotrophic S^0 oxidizers ranged from 6.8×10^3-2.2×10^5 per mL, while populations of heterotrophic S^0 oxidizers ranged from 8.6×10^3-2.2×10^6 per mL. The heterotrophic S^0 oxidizers detected would include the mixotrophic thiobacilli as well as heterotrophic bacteria and fungi, however, our data suggest that although relatively abundant they had a negligible impact in the reaction cells relative to the autotrophic S^0 oxidizers. Heterotrophs can play an important role by keeping the levels of dissolved organic carbon low, which is beneficial for autotrophic growth in these systems (Baker et al., 2004).

We were not able to measure α_{CO2} in the reaction cells flushed with a 3% O_2/10% CO_2 gas mixture because the change in [CO_2] was too small to accurately measure α_{CO2}. Assuming an α_{CO2} to α_{O2} ratio of 1:17 (O_2 to CO_2 molar consumption ratio for a mixed culture of autotrophic *Thiobacillus ferrooxidans* and *T. thiooxidans;* Lizama et al., 2002), a [O_2] decrease of 2% would have resulted in a [CO_2] decrease of only 0.1%. As a result, we estimated the α_{CO2} to α_{O2} ratio in the reaction cells to be less than 1:17.

The α_{O2} in the H_2O vapour reaction cells was below the detection limit ($<1\times10^{-6}$ mol O_2 $m^{-2}\cdot d^{-1}$). Therefore, the α_{O2} using water vapour was considered negligible in the

S^0 blocks, and H_2SO_4 production was considered to be limited to S^0 surfaces in contact with liquid H_2O (e.g., fracture faces).

The lower pH limit for microbial S^0 oxidation is not known. Brock (1978) reported microbial growth in water with pH as low as zero. Nordstrom et al. (2000) measured the lowest known pH (to our knowledge) of -3.6 ($[SO_4]$ as great as 760 $g \cdot L^{-1}$) for mine waters in contact with sulfide-rich rock; however, they were not able to determine if viable microbes were present in the water. However, Baker et al. (2004) and related publications demonstrate a complex microbial community in the Richmond Mine waters and biofilms at pH 0.5-0.9 that included autotrophic and heterotrophic bacteria, fungi, and protozoa.

4.4.4 *In situ* temperature

Temperature-depth profiles for TM03-07 (middle of the block) and TM03-14 (~10 m from the block edge) presented in Figure 4.7 represent the lowest and highest mean annual temperature profiles, respectively. Temporal variations in temperature decreased with depth as seasonal effects were dampened (typical temperature variation presented in Figure 4.8 for TM03-14). Temperatures at the 0.5-m depth ranged from -18 to 25°C and were generally <5°C from November to April (inclusive). Temperatures at the 1.5-m depth ranged from -2 to 19°C and were <5°C from January to mid-June. Temperatures <5°C at shallow depths were important during the winter and spring seasons because, as discussed in the O_2 modelling section below, they would have decreased S^0 oxidation (H_2SO_4 production) rates.

The average mean temperature at depths >5.5 m was 11.1°C but ranged from 8.8-14.4°C (Figure 4.7) for different locations. This variation may have been attributable to thermistor accuracy as temperatures varied by as much by 1-3°C for thermistors in the same profile installed at the same depth or separated by 0.3-m (data not presented). This variability is assumed to be an approximation of the thermistor accuracy (factory specifications unknown).

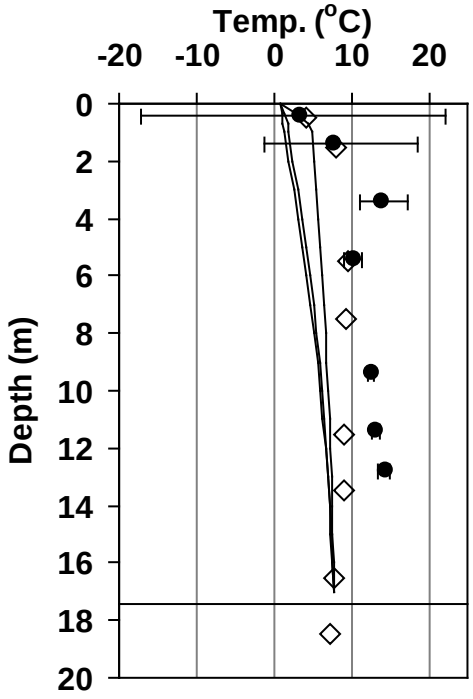

Figure 4.7. Temperature-depth profiles for the Phase 1 block for measured mean annual temperatures at TM03-07 (diamond symbols) and TM03-14 (solid circular symbols). Solid lines are modelled mean annual temperatures for simulations (from left to right) with no heat generation, 1.3 $J \cdot m^{-3} \cdot s^{-1}$ applied from 0-1 m and 8.6×10^{-4} $J \cdot m^{-3} \cdot s^{-1}$ applied below 1 m, and 5.8 $J \cdot m^{-3} \cdot s^{-1}$ applied from 0-1 m and 8.6×10^{-4} $J \cdot m^{-3} \cdot s^{-1}$ applied below 1 m. Bars on the TM03-14 data points represent minimum and maximum temperatures at each depth. Minimum and maximum bars are only presented for one modelled depth profile for clarity. Horizontal line represents the base of the S^0 block.

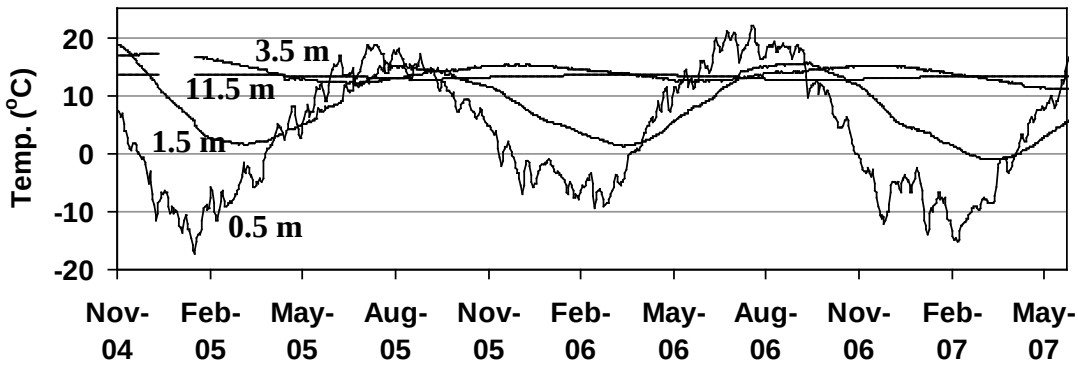

Figure 4.8. Temporal variation in temperature at TM03-14. Thermistor depths are labeled for each time series.

At a given location, temperatures at depths 3.5-5.5 m varied <3°C from May 2005 to May 2007, and by <1°C at depths >5.5 m. These small temporal variations did not follow consistent increasing or decreasing trends, suggesting temperatures at depths >5.5 m were either at a steady state, or changing very slowly (<1°C over 2.5 y measurement period). Model simulations (discussed below, data not presented) suggest annual temperature decreases at depths >5.5 m would be ~1°C if the block was still cooling, a change that would have been measurable during the 2.5 y measurement period.

In general, mean temperatures within the block were 1-6.5°C greater than at the base of the block (7.8°C), and 8-13.5°C greater than the mean annual atmospheric temperature (0.7°C) (Figure 4.7). Assuming relatively steady-state temperatures at depths >5.5 m (i.e., dissipation of initially high thermal energy of S^0 was complete), the increased temperatures in the block were attributed to heat generation from S^0 oxidation (discussed in greater detail below).

4.4.5 Measured and modelled distributions of *in situ* [O_2]

Trends in measured [O_2] distributions in the Phase 1 S^0 block for four sampling dates in 2006 are presented in Figure 4.9. Late-summer distribution of [O_2] (Figure 4.9D) in the Phase 1 S^0 block were originally presented by Birkham et al. (2010), but are included here for discussion of seasonal trends. [O_2] varied by 3-5% throughout the year with the lowest and highest levels measured in September and March 2006, respectively. General trends in [O_2] were similar throughout the year, with steep vertical gradients near the top surface of the block and more gradual lateral gradients.

Birkham et al. (2010) assumed the late-summer [O_2] distribution represented quasi-steady state conditions and modelled this distribution (Figure 4.10A) by applying O_2 consumption rates (β_{O2}) of 0.68 mol O_2 $m^{-3}\cdot d^{-1}$ in the upper 1 m and $<2.7\times10^{-4}$ mol O_2 $m^{-3}\cdot d^{-1}$ in the rest of the S^0 block (where [O_2] was >0) for EPM θ_a and ω of 7.3% and 0.21, respectively. θ_a and ω were 9% and 0.44, respectively, in the outer 35 m for depths of 0-1.5 m. Assuming a possible range in EPM θ_a and ω from 6.7% and 0.13 to 9% and 0.44, the range in best-fit β_{O2} in the upper 1 m was from 0.39-1.8 mol O_2 $m^{-3}\cdot d^{-1}$.

The increased β_{O2} near the top surface was required to create steep vertical O_2

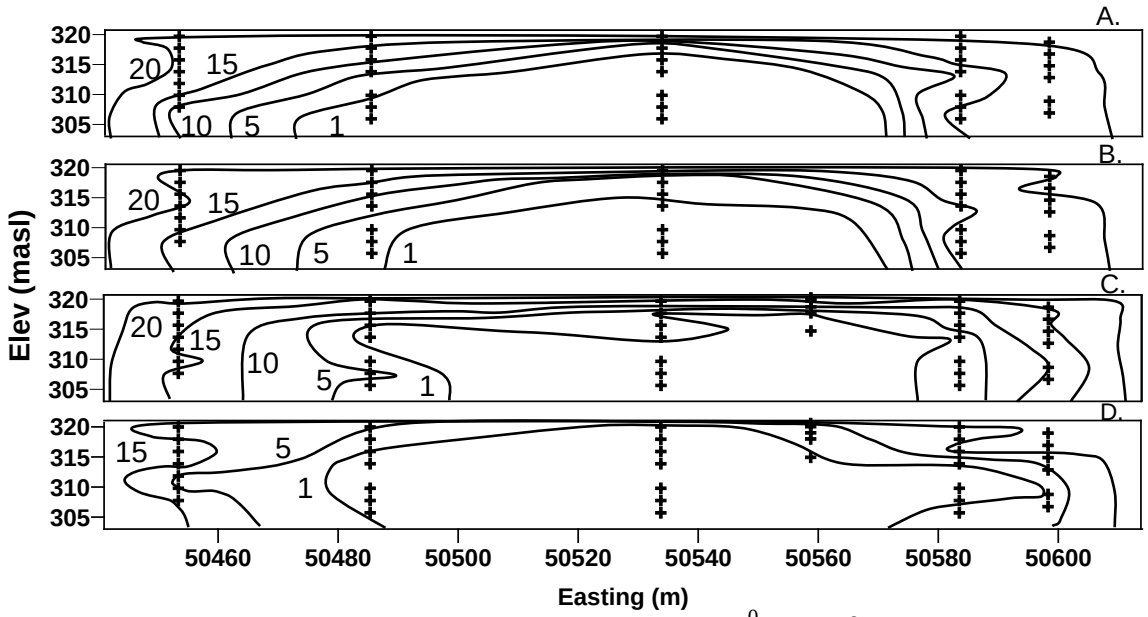

Figure 4.9. Measured [O_2] cross sections in the Phase 1 S^0 block for A) December 2005, B) March 2006, C) May 2006, and D) September 2006. Contours of 20 and 10% in Figure 4.9D have been omitted to improve clarity. Cross symbols represent sampling ports in the S^0 block.

gradients in the upper 1 m. We hypothesized greater β_{O2} during the summer near the S^0 block surface was the combined result of temperatures greater than 10°C for approximately 120 d of greater solar radiation and air temperature (Figure 4.8), greater microbial activity (Pisz, 2008), greater availability of nutrients from wind-blown sediments on the surface of the block, and more accessible S^0 fracture faces (reaction sites). We further hypothesized the fracture frequency and aperture to be greatest near the surface of the S^0 block (i.e., increased O_2 availability), as pouring of molten S^0 during block construction remelts underlying S^0 and reduces the n_f (Syncrude Canada Ltd., 2004b). Sulphur on the surface was observed to commonly be highly fractured and in loose shattered pieces as thick as 0.15 m.

Pisz (2008) collected samples from depth intervals of 0-0.1, 0.4-0.5, 0.9-1.0, 1.9-2.0, 2.9-3.0, 4.9-5.0, and 5.9-6.0 m at SRD05-143, -144, and -145 for microbiological analyses. Using the MPN technique, resident bacteria were only detected in the samples from 0-0.1 m at average concentrations of 18 MPN g^{-1} S^0 for culturable autotrophic S^0 oxidizers and 3 MPN g^{-1} S^0 for thiosulphate (S_2O_3) oxidizers. Pisz (2008) also detected the greatest concentration of *A. thiooxidans* from 0-0.1 m using polymerase chain

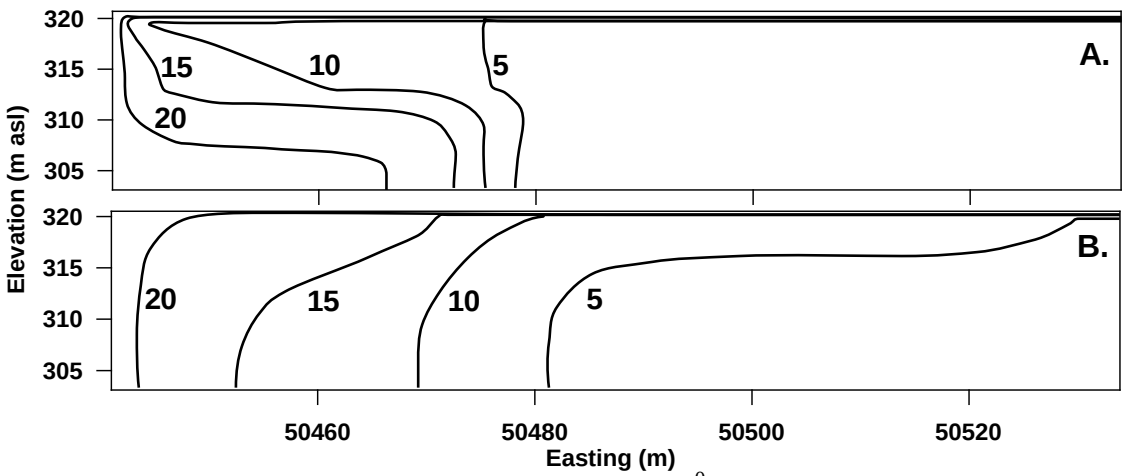

Figure 4.10. Simulated [O_2] distributions for Phase 1 S^0 block, where the left side of the cross section is the west side of the block, and the right side of the cross section is the middle of the pouring tower alley. Modelled distributions are for: A) summer conditions with increased β_{O2} in the upper 1 m (i.e., steady-state late summer conditions), and B) steady-state winter conditions with a uniform β_{O2} applied throughout the block (β_{O2} from 0-1.5 m set to zero) assuming Figure 4.10A as initial conditions.

reaction and DNA sequencing; however, these concentrations were not statistically different than for greater depths.

[O_2] distributions in the late winter (Figure 4.10B) were modelled by removing the increased β_{O2} in the upper 1 m, as temperatures at depths <1.5 m were <5°C (negligible β_{O2}). However, simply removing the increased near-surface β_{O2} resulted in modelled [O_2] being much too high near the upper surface of the block. Application of a thin (50 mm) layer with low θ_a (5%) and ω (5.6×10^{-5}-4.5×10^{-2}) on top of the S^0 block was required to limit influx of atmospheric O_2 and lower modelled [O_2] in the block (Figure 4.10B). For comparison, typical values of θ_a for sea ice range from 1-5% (Moslet, 2007); Ikeda-Fukazawa et al. (2005) approximated the ω of solid ice to be 2×10^{-6}. The addition of the thin surficial layer represented ice and snow on the top surface of the S^0 and acted as a barrier to the influx of atmospheric O_2. A thin layer of ice on the surface of the Phase 1 S^0 block was commonly observed during the winters of 2004 and 2005 (up to 0.02 m thick) and could act as low ω barrier. Mean snowpack depth was 184 mm in March 2006.

The ω for the 50 mm ice/snow layer was decreased with increasing distance from the edge of the block. Best-fit ω values were 4.5×10^{-2}, 5.6×10^{-3}, and 5.6×10^{-5} for easting

intervals of 50441-50471 m, 50471-50528 m, and 50528-50538 m, respectively. The decreasing ω with increasing distance from the edge of the block may have been the result of denser or thicker snow/ice pack near the center of the block. Simulations for winter conditions with increased β_{O2} from 3-3.5 m (where temperatures during winter were >5°C) were simulated but resulted in a poor match with measured $[O_2]$ gradients in the outer 60 m of the block. A K_a of 3×10^{-10} $m\cdot s^{-1}$ was assumed for the winter surficial layer, and 3×10^{-7} $m\cdot s^{-1}$ elsewhere (estimate based on permeability measurements by Bonstrom (2007)).

In spite of the differences between modelled and measured $[O_2]$ contours for late-summer months (Figures 4.10A and 4.9D), the general trend was similar. In particular, the 'bending' of measured $[O_2]$ contours towards the outer edge of the S^0 block during the summer could be simulated by applying increased β_{O2} values from 0-1 m.

4.4.6 Comparing O_2 consumption and H_2SO_4 production rates

Annual SO_4 production estimates based on the O_2 modelling for the Phase 2 block are presented in Table 2 (using stoichiometry from Eq. [4.1]). Greater than 97% of the annual SO_4 production was accounted for by assuming a constant β_{O2} for S^0 oxidation in the upper 1 m during the summer. However, if a lower β_{O2} was assumed instead of a greater θ_a and ω in the upper 1 m for the outer 35 m of the block (discussed above), S^0 oxidation in the upper 1 m could account for as little as 70% of annual SO_4 production. The total annual SO_4 production estimated from $[O_2]$ simulations (2.7×10^5-1.2×10^6 kg, assuming uniform β_{O2} in the upper 1m) was 50-220% of the measured mass loading of SO_4 from the Phase 2 block (5.5×10^5 kg). Considering the range and error associated with these estimates, the SO_4 production estimate from the $[O_2]$ modelling was similar to the measured SO_4 mass loading. This was consistent with the linear relationship between cumulative SO_4 loading and outflow in Figure 4.3 that suggested the production and removal rates of SO_4 were similar in 2006.

Although the β_{O2} was applied uniformly to each m^3 in the model, data presented above showed O_2 consumption (and H_2SO_4 production) in the blocks was isolated to S^0 surface areas in contact with liquid water. Birkham et al. (2009) reported the flowpaths

Table 4.2. Estimated SO_4 production in the Phase 2 S^0 block based on simulated β_{O2} for the Phase 1 block.

Region of S^0 block	Volume (m^3)	Estimated β_{O2} (mol O_2 $m^{-3}\cdot d^{-1}$)	Annual SO_4 production (kg)
Interior*	1,030,000	$<2.7\times10^{-4}$	$<6.6\times10^{3}$
Upper 1 m**	87,174	0.39-1.8	2.6×10^{5}-1.2×10^{6}

*applied to outer 40 m around the perimeter, the approximate thickness where [O_2] was >1%
**applicable to 120 d period (summer) for a thickness of 1 m

of H_2O in the Phase 1 S^0 block were limited to fractures and areas of highly porous or friable S^0. The reactive surface area in the S^0 block (per m^3) was estimated by dividing the modelled β_{O2} (Table 2) by the measured α_{O2} (scaled for the appropriate temperature) from the free-water reaction cells. For the interior of the S^0 block (at an average temperature of 11.1°C), the reactive surface area estimate was less than 4 $m^2\cdot m^{-3}$. During the summer months, the reactive surface area of the near-surface reactive layer (upper 1 m at an average temperature of 14°C) was estimated at 400-4,000 $m^2\cdot m^{-3}$. Assuming smooth fracture surfaces at vertical and horizontal frequencies of 33.5 and 5.4 m^{-1}, respectively (Bonstrom, 2007), the fracture surface area was estimated at 145 $m^2\cdot m^{-3}$. This suggested crushed or powdered S^0 particles as well as discrete fracture faces contributed to available surface area for S^0 oxidation in the upper 1 m.

4.4.7 Modelled temperature distributions

Modelled mean annual temperature depth profiles for the middle of the Phase 1 S^0 block are presented in Figure 4.7 and were generally 2-3°C less than measured temperature profiles for TM03-07 (middle of the block) and 4-8°C less than measured temperatures at TM03-14 (~10 m from the east edge of the block). One-dimensional temperature profiles are presented because simulated temperature depth profiles were uniform across the block with the exception of the outer 5 m. Considering the estimated accuracy of measured temperatures was ±1-3°C, measured mean temperatures for TM03-07 were considered similar to modelled mean annual temperatures when a G value of 501 $kJ\cdot m^{-3}\cdot d^{-1}$ (corresponding to the greatest estimated near-surface β_{O2} of 1.8 mol O_2 $m^{-3}\cdot d^{-1}$) was applied in the upper 1 m for 120 days (4 months during the summer

and autumn) each year. When no heat generation was applied to the S^0 block (G=0) or when an G of 108 $kJ \cdot m^{-3} \cdot d^{-1}$ was applied to the upper 1 m (corresponding to the lowest estimated near-surface β_{O2} of 0.39 mol O_2 $m^{-3} \cdot d^{-1}$), modelled mean temperatures in the upper 10 m were 1-3.5°C less than for the greatest G estimate (described above). This suggested *in situ* β_{O2} was at the higher end of the range estimated by the $[O_2]$ modelling and that heat generated during S^0 oxidation was an important control on temperatures in the Phase 1 S^0 block. Simulations including convective heat flux (not presented) determined convection had a negligible effect on heat flux in the S^0 block.

A G value of 0.07 $kJ \cdot m^{-3} \cdot d^{-1}$ (corresponding to an internal β_{O2} of 2.7×10^{-4} mol O_2 $m^{-3} \cdot d^{-1}$) was applied at depths below 1 m where $[O_2]$ was greater than 1% and S^0 oxidation would have been occurring; however, modelled temperatures were insensitive to internal G values ≤ 0.07 $kJ \cdot m^{-3} \cdot d^{-1}$.

4.5 Implications

Our findings that indicate the majority of H_2SO_4 is produced in the upper 1 m have important implications for the design of long-term storage strategies. Storage methods for limiting H_2SO_4 production by minimizing O_2 and/or H_2O influx, or involving the application of a biocide to minimize the activity of S^0-oxidizing microbes, should focus on the upper 1 m of the block. Further, given that oxidation rates in the water vapour reaction cells were less than the detection limit ($<1 \times 10^{-6}$ mol O_2 $m^{-2} \cdot d^{-1}$), S^0 oxidation by consumption of water vapour should not be a concern for potential S^0 storage strategies that limit water infiltration but would have RH=100% within the S^0 block.

Assuming β_{O2} values ranging from 0.39-1.8 mol O_2 $m^{-3} \cdot d^{-1}$ (0.26-1.2 mol S^0 $m^{-3} \cdot d^{-1}$) and a S^0 density of 2070 $kg \cdot m^{-3}$, the estimated annual S^0 loss to oxidation was 5×10^{-4}-2×10^{-3} m^3 (1-4.6 kg S^0) per m^3 in the upper 1 m. If this mass loss was derived from the fracture faces and translated directly to an increase in n_f, the maximum estimated annual increase in n_f would be 0.05-0.2%. The n_f in the upper 1 m is expected to increase over time as a result of S^0 oxidation; however, recurrent increases in the n_f by 0.05-0.2% each year will depend on whether fractures close as mass is lost to oxidation (e.g., due to overburden or confining pressures) or if fractures remain 'open'.

An increase in n_f with time would increase ω, K_a, and K_w and could contribute to increased H_2SO_4 production rates because of increased O_2 and water availability.

Under current conditions, the production of H_2SO_4 will most likely continue. As the block oxidizes, new surfaces for S^0 oxidation will be exposed. If at some future time H_2SO_4 production is limited by acidity, infiltration would eventually flush the H_2SO_4 from the block and H_2SO_4 production would resume. In cold climates such as the one in this study, H_2SO_4 production does not appear to be limited by gradual cooling of the block. Because the majority of H_2SO_4 is produced in the upper 1 m as a result of increased summer temperatures, cooling of the interior of the block to the average annual mean temperature (0.7°C) should have little effect on the production of H_2SO_4.

Maintaining low temperatures (<5°C) within S^0 blocks is a potentially effective strategy for minimizing H_2SO_4 production rates. However, the exothermic nature of S^0 oxidation should be considered when designing strategies that include soil or synthetic covers. Cover systems could insulate the block and heat released during S^0 oxidation could increase temperatures and H_2SO_4 production rates over time.

4.6 Acknowledgements

Field support was provided by Ron Lewko, Robert Mahood, and Gord McKenna, technical assistance by Julie Robertson, Matt Harker, and Rob Holben, and modelling assistance by Chris Kelln, Curtis Kelln, and Greg Newman (Geo-Slope International Ltd.). We acknowledge funding provided the Natural Sciences and Engineering Research Council of Canada and Syncrude Canada Ltd.

4.7 References

Attoe OJ and RA Olson. 1966. Factors affecting rate of oxidation in soils of elemental sulphur and that added in rock phosphate sulphur fusions. Soil Sci. 101: 317–327.

Baker BJ, MA Lutz, SC Dawson, PL Bond, and JF Banfield. 2004. Metabolically active eukaryotic communities in extremely acidic mine drainage. Appl. Envir. Microbiol. 70: 6264–6271.

Baldensperger J. 1976. Use of respirometry to evaluate sulphur oxidation in soils. Soil Biol. Biochem. 8:423-427.

Birkham TK, MJ Hendry, LI Wassenaar, and CA Mendoza. 2007. A transient model of vadose zone reaction rates using oxygen isotopes and carbon dioxide. Vadose Zone J. 6: 67–76.

Birkham TK, MJ Hendry, SL Barbour, SK Carey, JR Lawrence, and R Lewko. 2009. Water flow and storage in fractured, unsaturated sulphur blocks. *Submitted to Can. Geotech. J., June 2009.*

Birkham TK, MJ Hendry, and SL Barbour. 2010. Advective and diffusive gas transport through fractured sulphur blocks. *In Press toVad. Z. J., 2010.*

Bonstrom K. 2007. Physical controls on water migration in elemental sulphur blocks. M.Sc. Thesis, Dept. Geological Sciences, University of Saskatchewan. Saskatoon, SK, Canada.

Bonstrom K, SL Barbour, and MJ Hendry. 2009. Physical and hydraulic characterization of fractured, hydrophobic, sulphur within above ground sulphur blocks. Under revision, Can. Geotech. J.

Brock TD. 1978. Thermophilic microorganisms and life at high temperatures. Springer-Verlag, New York, NY. pp. 465.

Carotenuto A and M Dell'Isola. 1996. An experimental verification of saturated salt solution-based humidity fixed points. Int. J. Thermophys. 17(6): 1423–1439.

Chapman SJ. 1989. Oxidation of micronized elemental sulphur in soil. Plant Soil 116: 69–76.

Drever JI. 1997. The Geochemistry of Natural Waters. Prentice Hall, Upper Saddle River, NJ.

Elberling B, RV Nicholson, and JM Scharer. 1994. A combined kinetic and diffusion model for pyrite oxidation in tailings: a change in controls with time. J. Hydrol. 157: 47–60.

Elberling B and LR Damgaard. 2001. Microscale measurements of oxygen diffusion and composition in subaqueous sulfide tailings. Geochim. Cosmochim. Acta 65(12): 1897–1905.

Energy Resources and Conservation Board (ERCB) (Alberta, Canada). 2008. Alberta's energy reserves 2007 and supply/demand outlook 2008-2017. ST98-2008.

Environment Canada, 2009a. Accessed June 3. http://www.climate.weatheroffice.ec.gc.ca/climate_normals/results_e.html?StnID=2519&autofwd=1

Environment Canada, 2009b. Accessed June 3. http://www.climate.weatheroffice.ec.gc.ca/climateData/dailydata_e.html

Fenchel T, GM King, and TH Blackburn. 1998. Bacterial Biogeochemistry: the ecophysiology of mineral cycling, second edition. Academic Press, Toronto, ON.

Fredlund DG and H Rahardjo. 1993. Soil mechanics for unsaturated soils. John Wiley&Sons Inc., Toronto, ON.

Hendry MJ, CA Mendoza, RA Kirkland, and JR Lawrence. 1999. Quantification of transient CO_2 production in a sandy unsaturated zone. Wat. Res. Res. 35(7): 2189-2198.

Hyne JB, EJ Laishley, and RD Bryant. 1996. Sodium lauryl sulfate-a biocide for controlling acidity development in bulk commercially formed solid elemental sulfur. ASRL Quar. Bull. XXXIII(1; April-June): 29–41.

Ikeda-Fukazawa T, K Fukumizu, K Kawamura, S Aoki, T Nakazawa, and T Hondoh. 2005. Effects of molecular diffusion on trapped gas composition in polar ice cores. Earth Planet. Sc. Lett. 229: 183–192.

Jaggi RC, MS Aulakh, and R Sharma. 1999. Temperature effects on soil organic sulphur mineralization and elemental sulphur oxidation in subtropical soils of varying pH. Nutr. Cycl. Agroecosys. 54: 175–182.

Janzen HH. 1984. Sulfur nutrition of rapeseed. Ph.D. dissertation. Department of Soil Science, University of Saskatchewan. Saskatoon, SK, Canada.

Janzen HH. and JR Bettany. 1987a. Measurement of sulfur oxidation in soils. Soil Sci. 144: 444–452.

Janzen HH and JR Bettany. 1987b. The effect of temperature and water potential on sulfur oxidation in soils. Soil Sci. 144: 81–98.

Johnson BD. 1998. Biodiversity and ecology of acidophilic microorganisms. Microbiol. Ecol. 27: 307–317.

Kitto M. 2005. Sulphur supply/demand balance: the outlook to 2013. Proceedings of AFA 11th International annual fertilizer conference and exhibition. 1–3 Feb. 2005. Cairo, Egypt.

Knickerbocker C, DK Nordstrom, and G Southam. 2000. The role of "blebbing" in overcoming the hydrophobic barrier during biooxidation of elemental sulphur by Thiobacilllus thiooxidans. Chem. Geol. 169: 425–433.

Kosich D. 2008. Sulphur, potash prices soar last month as base and precious metals decline. International business times, June 20.

Laishley EJ, RD Bryant, BW Kobryn, and J.B. Hyne..1986. Microcrystalline structure and surface area of elemental sulphur as factors influencing its oxidation by *Thiobacillus albertis*. Can. J. Microbiol. 32: 237–242.

Lawrence JR, VVSR Gupta, and JJ Germida. 1988a. Impact of elemental sulfur fertilization on agricultural soils. 2. Effects on sulfur-oxidizing populations and oxidation rates. Can. J. Soil Sci. 68(3): 475–483.

Lawrence JR and JJ Germida. 1988b. Relationship between microbial biomass and elemental sulfur oxidation in agricultural soils. Soil Sci. Soc. Am. J. 52(3): 672–677.

Lawrence JR, YTJ Kwong, and GDW. Swerhone. 1997. Colonization and weathering of natural sulfide mineral assemblages by Thiobacillus ferrooxidans. Can. J. Microbiol. 43: 178–188.

Lee ES, TK Birkham, LI Wassenaar, and MJ Hendry. 2003. Microbial respiration and diffusive transport of O_2, $^{16}O_2$, and $^{18}O^{16}O$ in unsaturated soils and geologic sediments. Environ. Sci. Technol. 37: 2913–2919.

Li P and AC Caldwell. 1966. The oxidation of elemental sulphur in soil. Soil Sci. Soc. Am. Proc. 30: 370–372.

Lide DR (ed.), 2003. CRC Handbook of Chemistry and Physics, 84th Edition. CRC Press, Boca Raton, Florica; Section 4, Properties of the elements and inorganic compounds, heat capacity of the elements at 25^{o}C.

Lizama HM, PA Zielinski, LD Kerby, and CC Abraham. 2002. Comparison of biooxidation with carbon dioxide assimilation during bacterial growth on ferrous ion or elemental sulfur. Biotech. Bioeng. 77(1): 111–117.

Meyer B. 1977. Sulphur, energy and environment. Elsevier Scientific, Amsterdam.

Moldrup P, T Olesen, S Yoshikawa, T Komatsu, and DE Rolston. 2004. Three-porosity model for predicting the gas diffusion coefficient in undisturbed soil. Soil Science Society of America Journal 68: 750-759.

Moslet PO. 2007. Field testing of uniaxial compression strength of columnar sea ice. Cole Reg. Sci. Technol. 48: 1–14.

Nor YM and MA Tabatabai. 1977. Oxidation of elemental sulphur in soils. Soil Sci. Soc. Am. J. 41: 736–741.

Nordstrom DK, CN Alpers, CJ Ptacek, and DW Blowes. 2000. Negative pH and extremely acidic mine waters from Iron Mountain, California. Environ. Sci. Technol. 34: 254–258.

Pisz J. 2008. Characterization of extremophilic sulfur oxidizing microbial communities inhabiting the sulfur blocks of Alberta's oil sands. M.Sc. Thesis, Dept. Soil Science, College of Agriculture, University of Saskatchewan, Saskatoon, SK.

Plummer LN, DL Parkhurst, GW Fleming, and SA Dunkle. 1988. U.S. Geol. Survey Water-Resour. Invest. Report 88-4153.

Proce B. 2006. Oilsands Review. October 2006, 42–45.

Severinghaus JP, ML Bender, RF Keeling, and WS Broecker. 1996. Fractionation of soil gases by diffusion of water vapor, gravitational settling, and thermal diffusion. Geochim. Cosmochim. Acta 60(6): 1005–1018.

Skiba U and M Wainwright. 1984. Oxidation of elemental S in coastal-dune sands and soils. Plant Soil 77: 87–95.

Syncrude Canada Ltd. 2004a. Geo-environmental observations of 17 sulphur blocks in Alberta. Research Dept. Progress Report 33(2).

Syncrude Canada Ltd. 2004b. Geochemical characterization of a large sulphur block at Syncrude: results from the 2003 field investigation. June 21, 2004.

Wagner W and A Pruss. 2002. The IAPWS 1995 formulation for the thermodynamic properties of ordinary water substance for general and scientific use. J. Phys. Chem. Ref. Data, 31(2): 387–535.

Weast RC and MJ Astle. 1981. CRC Handbook of Chemistry and Physics. CRC Press, Boca Raton, FL.

Wen G, JJ Schoenau, T Yamamoto, and M Inoue. 2001. A model of oxidation of an elemental sulfur fertilizer in soils. Soil Sci. 166(9): 607–613.

Wilson RE. 1921. Humidity control by means of sulfuric acid solutions, with critical compilation of vapor pressure data. J. Ind. Eng. Chem. 13(4): 326–331.

Wilson GW, DG Fredlund, and SL Barbour. 1997. The effect of soil suction on evaporative fluxes from soil surfaces. Can. Geotech. J. 34: 145–155.

5.0 SUMMARY OF CONCLUSIONS

5.1 Water flow and storage in fractured, unsaturated sulphur blocks

Despite the hydrophobicity of S^0, water infiltrates rapidly through fractured S^0 blocks with bulk K_s values (1×10^{-1} to 1×10^{-3} m/s) similar to that of a gravel or clean sand. Preferential flow pathways occurred through fractures and friable S^0. Localized hydrophilic conditions measured on fracture faces contributed to preferential flowpaths and were the result of colonization of S^0-oxidizing microbes. Greater than 90% of rainfall infiltrated and rapidly drained from the block as surface evaporation rates were low (mean 0.2 mm/d). Representing the S^0 blocks as a hydrophilic equivalent porous medium adequately described the flow and storage of water for modelling purposes. Vertical infiltration and lateral drainage at the base of the blocks were quantified using a 1-D analytical solution and 2-D numerical model, respectively. Transient simulations of water ponding and drainage at the base of a S^0 block were compared with field data. Specific yield (S_y) and K_s values used in the model were varied to obtain hydraulic head and outflow responses that corresponded with measured values reasonably well. S_y was estimated at 0.8 to 4.4% which indicated water occupied the fracture porosity and a portion of the matrix porosity at the base of the block after rainfall events.

5.2 Advective and diffusive gas transport through fractured sulphur blocks

In situ distributions of $[N_2]$, $[O_2]$, and $[CO_2]$ were used to quantify the direction and magnitude of *in situ* gas fluxes. Quantification of O_2 and CO_2 fluxes was necessary to explain the direction and magnitude of N_2 concentration gradients that developed in the block, despite the fact that N_2 was non-reactive. Advection, created by O_2 consumption within the block, accounted for 20% of the total O_2 influx and considerably increased H_2SO_4 production in the block above that attributed to O_2 diffusion alone. An *in situ* SF_6 tracer experiment and laboratory diffusion cell experiments were performed and modelled to quantify D_e for a fractured S^0 block and matrix S^0, respectively. Mean values of ω and interconnected $\theta_{a,m}$ for matrix S^0 were

0.11 (s.d.=0.03, n=6) and 6.1%, respectively. Values of ω and EPM θ_a for a fractured S^0 block ranged from 0.13-0.44 and 6.7-9%, respectively. SF_6 tracer concentrations in the upper 8 m were lower than expected for diffusive gas transport and were attributed to multiple flushing cycles of the fracture porosity from changes in barometric pressure. A small net O_2 influx may have resulted from repeated barometric pressure cycles, however O_2 influx from increased barometric pressure would likely be approximately balanced by O_2 efflux when the barometric pressure decreased.

5.3 Controls and rates of acid production in commercial-scale sulphur blocks

H_2SO_4 production rates in a S^0 block were estimated by quantifying O_2 influx rates assuming S^0 oxidation (H_2SO_4 production) was the dominant O_2-consuming process in the blocks. *In situ* [O_2] modelling suggested 70 to >97% of the annual H_2SO_4 production occurs in the upper 1 m of the blocks where temperatures increased to >15°C during the summer. S^0 oxidation rates were more sensitive to temperature (Q_{10}=4.3) than soil respiration processes reported in the literature (Q_{10}=1.5-3.0) and were controlled by the activity of autotrophic S^0-oxidizing microbes. The efflux of SO_4 in drainage water from a S^0 block (5.5×10^5 kg) was within the estimated range of SO_4 production within the block (2.7×10^5-1.2×10^6 kg), suggesting H_2SO_4 production and removal rates were approximately equal during the study period. The low mean RH within the block (68%, s.d.=17%, n=21) was attributed to osmotic suction from elevated H_2SO_4 concentrations and suggested a mean *in situ* pH of approximately -2.1. The pH of drainage waters (0.4-1.0) was attributed to mixing of fresh infiltrating water and low-pH *in situ* water. Heat released during S^0 oxidation was an important control on maintaining temperatures within the block (mean=11.1°C) 1-3.5°C greater than would be expected if there were no heat source in the block.

6.0 IMPLICATIONS FOR S^0 STORAGE

The purpose of this research was to provide a scientific basis to those who will design site-specific storage facilities, rather than to recommend specific plans for S^0 storage. Climate, available construction materials, land availability, and budget constraints will determine the most appropriate S^0 storage methods for each site. However, several general principles from this research can be widely applied to the design of S^0 storage strategies.

- Designs for S^0 storage that minimize H_2SO_4 production should focus on S^0 oxidation in the upper 1-m. Although this near-surface S^0 oxidation may make biocide application an attractive option for minimizing H_2SO_4 production, this strategy should be carefully considered. Surface application of biocide may greatly reduce the activity of S^0-oxidizing microbes in the upper 1-m however this action might increase O_2 availability at depths greater than 1 m and move the zone of H_2SO_4 production to greater depths.
- Minimizing temperatures in S^0 blocks would be an effective method of limiting H_2SO_4 production, particularly if temperatures were <5°C. However, thermal modelling in this study suggested that heat generation from S^0 oxidation in an exposed S^0 block maintained temperatures 1-3.5°C greater than scenarios with low or no heat generation. Consideration should be given to the heat released during S^0 oxidation when designing cover systems that might insulate the S^0 blocks. An insulating cover might reduce heat escape from the block and result in increased temperatures, and H_2SO_4 production rates, in the block. Additionally, adequate time would be required between the pouring of molten S^0 and the construction of an insulating cover to allow the block to cool.
- Minimizing the influx of H_2O and O_2 would be an effective strategy for limiting H_2SO_4 production and drainage from S^0 blocks. Limiting H_2O infiltration would decrease the volume of acidic drainage water, however, because of the small amount of water required to maintain S^0 oxidation (annual water demand

estimate 2.6 mm/m^2 in this study) a cover system would have to be extremely efficient to decrease H_2SO_4 production rates. A cover system that sealed fractures (e.g., a bitumous cover) from water flow could be very effective in minimizing both water infiltration and H_2SO_4 production. This type of cover system would take advantage of the hydrophobicity of matrix S^0 and, if the top of a S^0 block was sloped appropriately, water runoff rates could be very high.

- For geologic media where $[O_2]$ are low (<1 %; i.e. S^0 blocks) and oxidation rates are independent of $[O_2]$, O_2 influx rates are approximately proportional to the $[O_2]$ directly above the S^0 block surface. Therefore, minimizing the $[O_2]$ at the S^0 surface can greatly reduce H_2SO_4 production in S^0 blocks. O_2 influx through the sidewalls of S^0 blocks should also be considered when designing O_2-limiting cover systems. S^0 oxidation was found to be a zero-order reaction with respect to $[O_2]$ (for $[O_2]$ >1%), therefore $[O_2]$ would have to be <1% for S^0 oxidation rates to be limited by O_2 availability.

7.0 RECOMMENDATIONS FOR FURTHER WORK

- Water flow modelling assuming hydrophobic conditions should be addressed by adding the capability of hydrophobic moisture retention curves in the Geostudio 2007® model. Although modelling of water storage and outflow response to rainfall events corresponded well with measured data assuming hydrophilic conditions along fracture faces, the uniqueness of these solutions should be assessed. Very small positive pore water pressures are required for water to enter large hydrophobic fractures, therefore the importance of hydrophobic portions of the fracture porosity during water infiltration is unclear.
- The water infiltration and drainage modelling was limited to intense distinct rainfall events. Although likely very difficult, the ability to model the infiltration, storage, and drainage of water from sequential rainfall events with varying intensity would allow more rigorous testing of the S_y and K_s estimations presented in this study.
- A more accurate method of measuring *in situ* K should be developed. This may be achieved by developing a method of cleaning powdered S^0 from fractures along borehole sidewalls after drilling.
- A dye tracer that had a contact angle >90° should be considered in future dye tracer experiments. This would show flow pathways more similar to those of water and likely result in less spreading relative to the Brilliant Blue FCF tracer used in this study.
- Initial estimates of convective gas transport (not presented) indicated that convection was negligible, however this should be verified with more rigorous modelling of the temperature regimes in S^0 blocks.
- The injection of gas tracer for measurement of *in situ* D_e should be completed more precisely than the methodology presented in this thesis. One possibility would be to push a 1/8 inch copper tube down the CMT tube before installation so the end of the copper tube extended through the CMT sampling port. The

space around the copper tube at its exit from the CMT sampling port could be sealed to prevent gas migration back up the CMT channel. The small diameter tube would ensure direct injection of the tracer into the formation with minimal mixing within the injection tube or channel. The small diameter injection tube would also allow for better control of the initial tracer concentration which could be minimized to reduce gravitational settling if a heavy gas (eg. SF_6) is used.

- If repeated, reaction cell experiments for α_{CO2} measurement of autotrophic microorganisms should be repeated with initial headspace of ~20% O_2/~10% CO_2/balance N_2 (compared to 3% O_2/10% CO_2/balance N_2 in this study). Increasing the initial headspace [O_2] would increase the likelihood of measuring CO_2 consumption, and accurately measuring α_{CO2}.
- *In situ* pH as low as -3.8 was estimated by *in situ* RH measurements. Direct measurement of the *in situ* pH would help to confirm these extremely low pH estimates. If an *in situ* methodology was not possible, a portion of a S^0 block could possibly be destructively sampled and pH of fracture faces could be measured. This would require a pH probe that was effective at very low moisture contents, or an alternate method (eg. pH sensitive stain indicator). If direct measurement of *in situ* pH is not possible, a more rigorous methodology for *in situ* RH measurement should be pursued.
- Given the low *in situ* pH estimates, research is required into the effect of low pH on microbial activity. The lower pH limit for microbial activity in S^0 blocks is not known and would have implications on long-term acid production.
- The results of this study should be compared to the performance of the five research pilot blocks at Syncrude Canada Ltd. These blocks have been instrumented for sampling of water fluxes and *in situ* gas, and temperature profiles and should provide an excellent opportunity to test the findings of this study.

APPENDIX

Data and modelling files

Data presented in this thesis dissertation are included on the enclosed CD. This includes modelling files for Geostudio 2007®.